Intermediate Band Solar Cells based on ZnTeO

by

Weiming Wang

A dissertation submitted in partial fulfillment
of the requirements for the degree of
Doctor of Philosophy
(Electrical Engineering)
in The University of Michigan
2010

Doctoral Committee:

Associate Professor Jamie D. Phillips, Chair
Assistant Professor Pei-Cheng Ku
Assistant Professor Wei Lu
Assistant Professor Max Shtein

To My Wife, My Parents, and My sister

Acknowledgement

At the end of this dissertation writing, I would express my gratitude to my research advisor, Prof. Jamie D. Phillips. In almost four years in his group, he guided me get through all difficulties in my research. He continuously found financial resources to support my research work, provided insight suggestions and directions, reviewed all my English writing sentence by sentence. And more importantly, he always gives me some space, provides me to enough resources, spares my eagerness of knowledge, and strengthens my problem-solve skills. I really cherish this training. I also appreciate his hand-on-hand instruction of taking care of PLD and MBE systems. It not only takes huge of time, but also patience, energy, trust, and fund to graduate a Ph.D. student. I am really grateful all of his effort.

I also thank my committee members: Prof. Pei-Cheng Ku, Prof. Wei Lu, and Prof. Max Shtein. All of them not only provided extremely valuable suggestions on my thesis work, but also provided free accesses of their research labs.

I would thank Prof. Charles Tu, my research advisor at University of California, San Diego, who gave me the initial training of MBE growth, material and device characterization.

From Nov. 2008 to Oct. 2009, the MNF staff members, Dennis Schweiger and Fred Sequin helped to move out my MBE system from the cleanroom, and shipped it out for cleaning, and assembled it in the new lab space. I really appreciate their help.

Then I would also express my gratitude to Kuen-Ting Shiu. He not only supported me most of device characterization in Prof. Forrest's research lab, but also shared lots of MBE experiences, and MBE parts with me. Guo-Dan Wei and Fan Yang also helped me measure the devices. I really appreciate it.

Dr. Wyatt Metzger at National Renewable Energy Lab provided the TRPL measurement. Sara Spanninga helped XPS measurement. Luke Lee and Min Kim provide initial training of TRPL set-up and measurement. All of works are essential in my thesis.

Albert Lin, Willie Bowen, Emine Cagin in our group provided theoretical and experimental support for my thesis work. And Yiying Zhao in Prof. Max Shtein had lots of discussion of measuring the two-photon process. It is very helpful.

It is very hard to maintain the MBE by myself. Therefore, my MBE colleagues Guan Huang, Meng Zhang, Debashish Basu, Wei Guo in Prof. Pallab Bhattacharya help me a lot to take care of it. I also very appreciate their helps.

Then all of my friends from University of Michigan and all of current and previous group members (Pierre, Jeff, Jinyoung, Anne, Ding, Kaveh) are essential of my happy experiences in Ann Arbor.

Finally, I would thank my wife, my parents and my sister. Their understanding and support make this working meaningful.

Table of Contents

List of Figures

List of Tables

List of Appendices

List of Abbreviation

CB	Conduction band
VB	Valence band
IB	Intermediate band
IBSC	Intermediate band solar cell
MBE	Molecular beam epitaxy
PLD	Pulse laser deposition
ALD	Atomic layer deposition
PL	Photoluminescence
TRPL	Time resolved photoluminescence
FOM	Figure of merit
FF	Fill factor
SIMS	Second ion mass spectrum
XPS	X-ray photoelectron spectroscopy
XRD	X-ray diffraction
CRT	Carrier recombination and transportation

ABSTRACT

Low-cost, high efficiency solar cells are of tremendous interest for the realization of a renewable and clean energy source. The conversion efficiency of a single junction solar cell with an Intermediate Band in the bang gap is theoretically predicted to be as high as that of a triple junction solar cell by expanding the absorption spectrum without sacrificing the open-circuit voltage. In this work, an Intermediate Band Solar Cell based on the ZnTeO material system is investigated both experimentally and theoretically

ZnTeO thin films synthesized by MBE and PLD are compared by characterizing their structural, chemical and electrical properties, which conclude that low oxygen partial pressure in MBE growth preferentially leads to subtitutional oxygen impurity in ZnTe. These states and related complexes, located at 0.4-0.7eV below the conduction band, with a radiative recombination coefficient of 1.2×10^{-10} cm^3 sec^{-1} and an absorption coefficient of 10^4 cm^{-1} are excellent candidates to demonstrate the IBSC technique.

The theoretical work reveals that both the open circuit voltage and fill factor degrade but the short circuit current increases in a ZnTe junction with oxygen states in comparison to those of a junction without oxygen states. When the optical cross-sections of oxygen states are larger than $10^{-14}cm^2$, the conversion efficiency of ZnTeO based IBSC can be more than 20% with the optimal oxygen states density in range of 10^{20}-10^{21} cm^{-3}, nearly double of that of a ZnTe cell without oxygen states.

Experimentally, ZnTeO based cells exhibit an expanded response to the solar spectrum in comparison to ZnTe due to photo-excitation below the bandgap energy, resulting in an approximate double of the short circuit current, while suffering an approximate 15% decrease in open circuit voltage. Sub-bandgap excitation experiments under 650nm and 1550 nm excitation demonstrate absorption of two photons in sequence, which is desired for intermediate band solar cells and serve as a basis for further efforts to develop ZnTeO for enhanced solar cell conversion efficiency. The diode structure was

further optimized by n-ZnO/p-ZnTe hetero-junction with enhanced diode characteristics. A ZnSe buffer grown by MBE between the ZnO/ZnTe interface demonstrated a significant improvement of photovoltaic effect.

Chapter 1

Introduction

1.1 Motivation and Background

Energy is the most fundamental issue for our world's evolution. Since the first industrial revolution in the middle of the 19th century, coal, petroleum, and natural gas have been our predominant energy sources. Figure 1.1 shows unrenewable sources, such as fossil fuels and nuclear fission, account for more than 90% of the United States national energy supply in 2008. Globally, this percentage is even higher. Continuous consumption of these materials is recognized to damage our environment, break Earth's ecosystem, and eventually harm humanity. Therefore, it is essential to seek alternative energy supplies by increasing the percentage of clean and renewable energy sources in order to sustain long-term development of society.

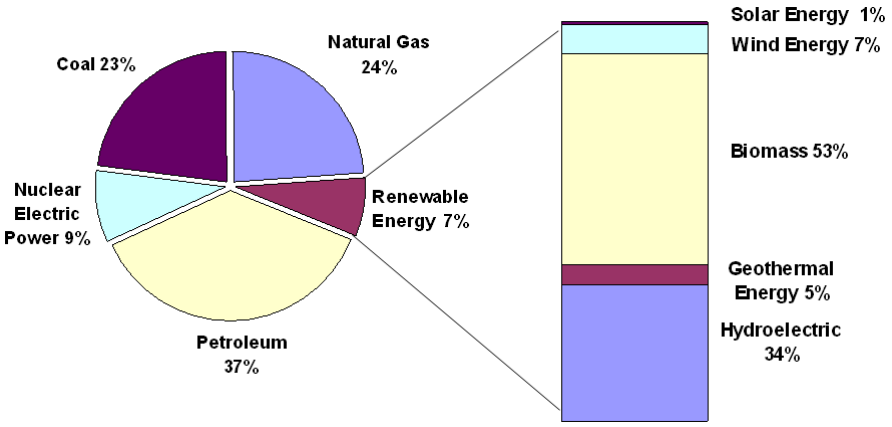

Figure 1.1 USA National Energy Supply in 2008[1].

Solar energy is the cleanest and most abundant source on the Earth in comparison to hydroelectric, wind, geothermal energy, and other renewable energies, as quantitatively shown in the Figure 1.2**.** The solar power delivered to the earth's surface is thousands

times more than we need. For example, an area of 100 miles by 100 miles under standard AM1.5 sunlight receives enough Sun power to exceed our global consumption in 2008. Solar energy is the most universally available, potentially saving the cost of energy transmission by setting the energy generation and consumption in close proximity.

Solar energy is an ideal alternative energy because it is clean, renewable, abundant, and universally available. However, as shown in Figure 1.1, solar energy only provided 0.07% of the USA's energy supply in 2008 due to the high cost of current technologies. The overall cost of using solar energy is related to land requirements, manufacturing, installation and maintenance of solar energy conversion facilities. The technology of manufacturing solar conversion facilities is the most critical factor in deciding whether solar energy can compete with other energy sources and eventually become a dominant contributor to our energy supply.

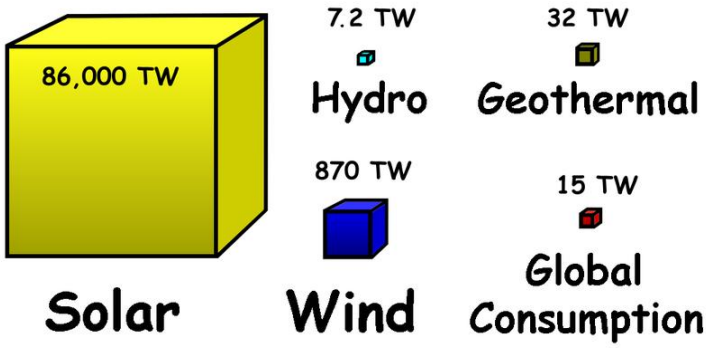

Figure 1.2 Availability of renewable energy in the world[2].

Generally, there are two technologies for solar energy. One is solar thermal technology by which solar energy is converted into thermal energy, such as hot water for home or industry application, or subsequently converted thermal energy into electricity. Low cost of energy storage is the most significant advantage for solar thermal technology. The other is solar photovoltaic technology, which directly converts sunlight into electricity. One photovoltaic cell usually generates a small amount of energy depending on the cell size and sunlight intensity. When connected either in series or parallel, photovoltaic cells can generate electricity with a very wide range of current and voltage,

which is suitable for diverse scenarios from milliwatt (10^{-3} watt) solar calculators to gigawatt (10^{9}) solar power plants.

1.2 Photovoltaic Technologies

In a photovoltaic cell, electron-hole pairs are created by absorbing photons. Then these electrons and holes drift in an opposite direction, and contribute power to external loads. The solar spectrum covers a wide range from ultraviolet to infrared as shown in Figure 1.3. Those photons with energy less than the band gap of material (E_g) are not able to generate electron-hole pairs. This behavior is illustrated in Figure 1.4, and presents one significant loss in conversion. On the other hand, electron-hole pairs created by photons with energy exceeding the band gap (E_g) will relax to the band edge before extraction as as a photocurrent. This is another major source of loss in photovoltaic solar cell. Balancing these two effects, the maximum conversion efficiency of a single junction based on thermodymanics is 31%, Schokley-Queissier limitation[3].

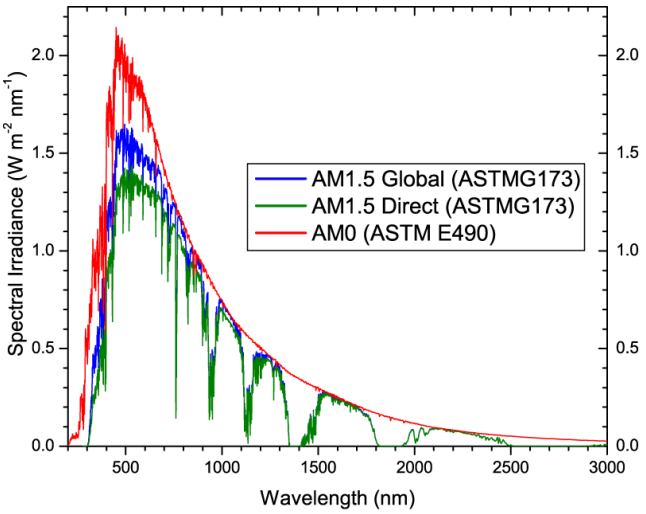

Figure 1.3 Standard solar spectrum AM1.5 and AM0[4].

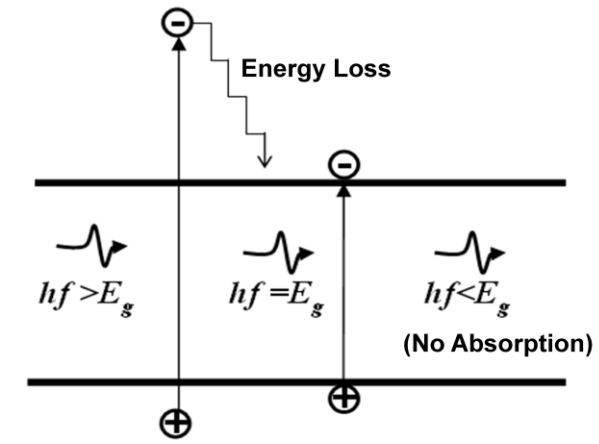

Figure 1.4 Schematics of electron excitation in photovoltaic cells.

Since the first modern photovoltaic cell was realized on silicon by Bell Labs in 1954[5], the performance has been improved dramatically, including the development of exciting technologies have been invented[6]. The Figure of Merit (FOM) of photovoltaic cell technologies is the cost per unit power. According to the FOM, these photovoltaic technologies are categorized into three generations as shown in Figure 1.5.

The 1st generation refers to wafer based technologies using single crystal semiconductor materials. The record efficiencies of the single junction cells based on Si, GaAs and InP wafers are 25%, 26% and 22% respectively[7]. The high energy consumption for molding single crystal wafers and relative scarcity of materials, such as indium and gallium, these photovoltaic cells are very expensive. Poly-crystalline silicon cells are a mature technology, and have been manufactured in a gigawatt-scale, seizing over 80% of the current photovoltaic market with very limited room for cost reduce.

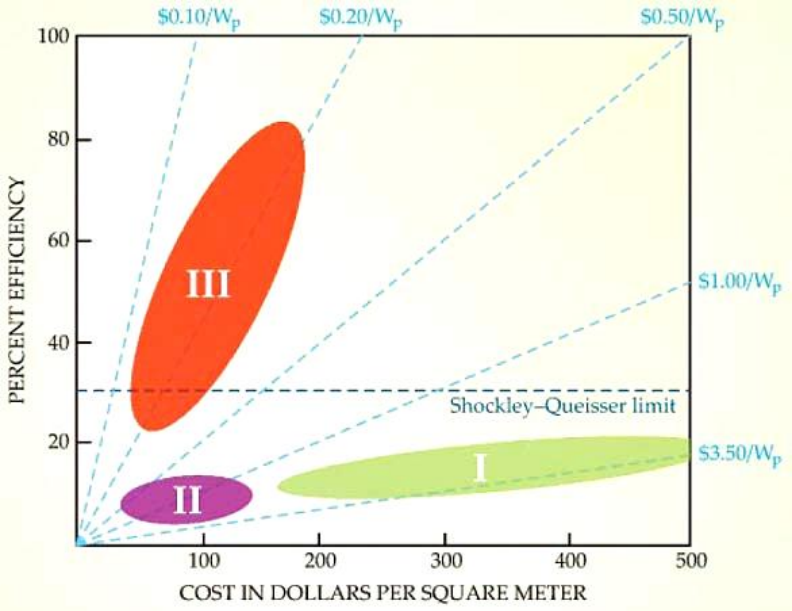

Figure 1.5 Efficiency and cost projects for1st-, 2nd and 3rd-generation photovoltaic technology (wafers, thin-films, and advanced thin-films, respectively). [8]

The 2nd generation includes thin-film photovoltaic technologies fabricated on non-crystal substrates, such as glasses and metal foils, which are one or two orders of magnitude cheaper than single crystal substrates. The most typical absorption films are CdTe, $CuInGaSe_2$ (CIGS), and amorphous silicon (a-Si:H), with absorption coefficient greater than 10^4 cm^{-1}. With a thickness of 3μm, these thin films can capture over 95% of incident solar photons above the absorption band edge, resulting in low usage of scarce materials, such as tellurium and indium. To date, the highest efficiencies of CIGS, CdTe, and a-Si:H. achieved in the lab are 19%[9], 16%[10] and 10%[11], respectively. Although the thin film photovoltaic cells are lower in conversion efficiency and shorter in working lifetime than those on single crystal wafers because of much higher defects density, the overall cost per watt is still lower than the 1st generation. As a result, the thin film photovoltaic cells are leading the PV market growth.

The 3rd generation photovoltaic cells aim to harvest more solar energy by reducing or eliminating the energy loss effects as mentioned in previously, which includes the following technologies.

1. Multi-junction. Multiple pn junctions are connected in series with the highest band gap junction at top and the lowest band gap at bottom. Each junction

covers a select range of the solar spectrum. Therefore, the thermalization loss is much less than that of a single junction cell. The limiting efficiency is 86.8% for an infinite number of junctions in series[12]. The GaInP/GaInAs/Ge based triple junction cell [13] is a representative technology with demonstrated efficiency greater than 40%. Cells with four or five junctions in series are under development for higher efficiency. The complex device structure of a multi-junction cell results in a higher manufacturing cost. In order to reduce the cell size, highly concentrated sunlight by optics lenses is applied.

2. Multi-exciton. One high energy photon generates more than one electron-hole pairs so that the output current is enhanced. This technology has been demonstrated by quantum dots [14]. However, the quantum efficiency of generation of multiple electron-hole pair is too low to be a practical device.
3. Hot carrier extraction. Photons with energy above the band gap will excite the hot carriers. The output voltage will be improved if these hot carriers can be extracted out before they relax via phonon scattering.[15]. This technology has not been demonstrated yet.
4. Intermediate band. Electron states are introduced into the forbidden band gap to provide increased absorption due to multi-photon processes. In addition to the transition from the valence band to the conduction band, the transition via the intermediate band states occurs by absorbing two sub-gap photons in sequence. Therefore, the short-circuit current (J_{sc}) is increased without sacrificing the open circuit voltage (V_{oc}). The efficiency of an intermediate band cell implemented by a homo-junction is able to surpass the Shockley-Queisser limitation with an ultimate limit as high as a triple junction cell's. Additionally, because of the parallel process inside, an intermediate band cell performs more stably than a triple junction cell when the input solar spectrum is distorted by weather. Finally, intermediate band solar cells are possibly fabricated on the non-crystal substrate because of the weak restrain of lattice match for single junction structure. Therefore, an intermediate band cell, potentially achieving a better FOM than a multi-junction cell, has become an exciting research topic.

1.3 Concept of Intermediate Band Solar Cell

With an additional band in the forbidden band gap, three optical transition happen simultaneously, from Valence Band (VB) to Conduction Band (CB), from VB to Intermediate Band (IB), and from IB to CB, as illustrated in Figure 1.6. Therefore, sub-gap photons are absorbed, increasing output current without decrease the band gap.

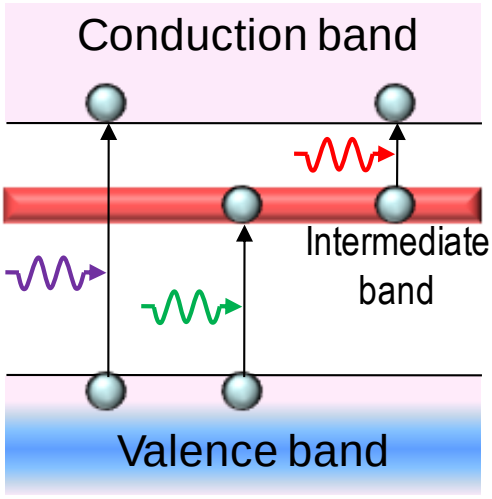

Figure 1.6 Schematic of optical transitions in intermediate band solar cells.

This concept was first proposed by M. Wolf[16] in 1960. Subsequently, Schokley and Queisser had concluded that defect states in the forbidden band gap acting as nan-radiative recombination centers are improbable to improve the overall conversion efficiency[3]. Experimentally, the improved short-circuit current was observed in an impurity silicon solar cell in 1970 by Gutter and Queisser[17] but no overall efficiency enhancement. However, since 1990, further theoretical studies[18-23] have predicted that an overall conversion efficiency higher than Shockley-Queisser limit is achievable in a single junction with either an impurity level or an intermediate band. The maximum efficiency can be as high as 63% based on the following conditions[22, 23]:

1. Negligible non-radiative recombination for band-to-band transitions.
2. Ideal carrier transportation. In other words, all photo-carriers can transport out to terminals before recombination.
3. Optimal bandgap energy of the host material (1.9eV) and position of intermediate band states (0.7eV from the band edges) for black body radiation solar spectrum.

4. Non-overlapping bands for over optical transitions. This requirement ensures that higher energy photons are not used to excite lower energy transitions, which would result in energy loss.

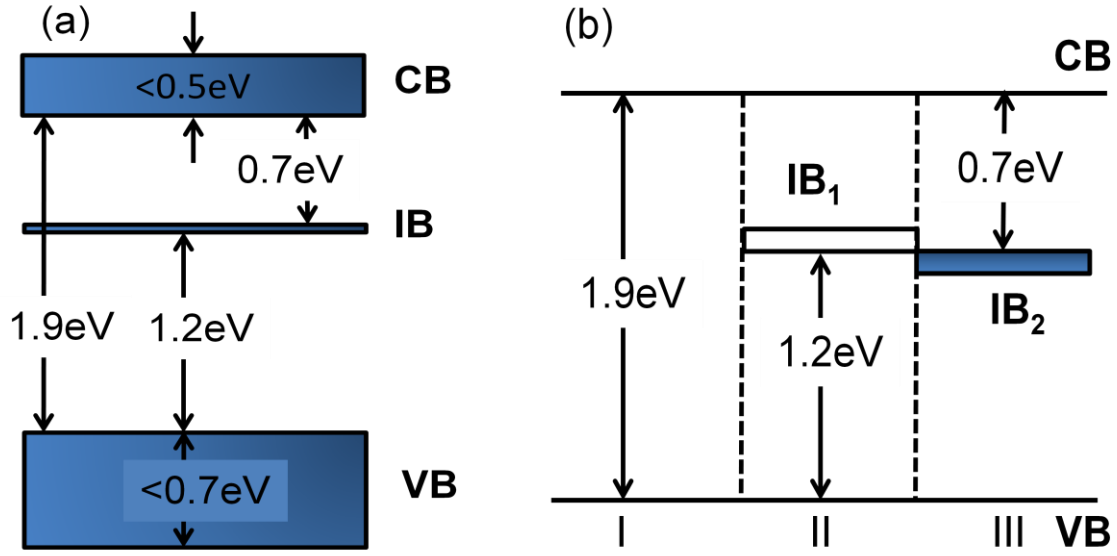

Figure 1.7 Approaches for non-overlapping approaches: (a) Limited band width, (b) Spatial separation.

One of methods to realize non-overlapping absorption is the limited band width as shown in Figure 1.7 (a). The bandwidth of the VB is less the transition energy from the IB to the CB, and the bandwidth of the CB is less than the difference between transition from the VB to the IB and that from the IB to the CB. Therefore, any photons in the solar spectrum with its energy greater than the minimum of band-to-band transition will be separated into three groups without any overlapping in the energy space. However, the defined band structure is hard to be achieved in the real device structure. Spatial separation as shown in Figure 1.7 (b) is the much more feasible technology for semiconductor devices. The absorption region is separated into three ranges according to the status of the IB. In the first range without the IB structure, only absorption of the VB to the CB can happen. In the second range with a completely empty intermediate band (IB_1), only the absorption from the VB to IB_1 can happen. In the third range with a totally full intermediate band, only the absorption from the IB_2 to the CB can happen.

1.4 Experimental Approaches to Realize IBSC

The high conversion efficient predicted for IBSC make the approach very attractive. However, a few technologies have been explored to demonstrate this multi-photon approach including quantum confinement structures (quantum dots[2429], quantum wells[30]), diluted semiconductor alloys[31,32], and deep level impurities[16,33].

1.4.1 Quantum Dots and Quantum Wells

Both quantum well and quantum dot structures are the most extensively studied to achieve an intermediate band. Enhanced short-circuit current (J_{sc}) has been realized by the $Al_{0.3}Ga_{0.7}As$/GaAs quantum well cell[30] where overall efficiency is 110% higher than that of the reference cell using $Al_{0.3}Ga_{0.7}As$ is used as absorber. After two decades of development, the efficiency of a single junction cell based on strain-balanced InGaAs/GaAsP multiple quantum wells with IB position about 0.1eV below the CB has reached 28% under 500 suns[34]. Based on the intermediate band theory, a deep level band near 0.7eV from the band edges is preferred for high efficiency. The required barrier height is very difficult to achieve in the InGaAs/GaAsP system due to phase separation problem. Alternatively, quantum dots such as InAs/GaAs, InN/InGaN have been proposed and enhanced absorption via multi-photon processes has been demonstrated. However, the photon carriers in quantum dots are very hard to be extracted out before recombination because of strong confinement in dots. Moreover, absorption volume of quantum dots is limited by strain and sparse quantum dot density. Enhanced short-circuit current (J_{sc}) has not been observed in quantum dots based intermediate band solar cells[35].

1.4.2 Deep Level Impurities

Deep level impurities acting as non-radiative recombination centers[36], including gold and indium doped in silicon, have not succeeded in intermediate band application. Alternatively, isoelectronic impurities including GaP:N, GaP:Bi and ZnTe:O with highly radiative recombination have been proposed to use as an intermediate band.

1.4.3 Dilute Alloys

Dilute semiconductor alloys mainly refer to diluted nitride III-V semiconductors and diluted oxygen II-VI semiconductors. Because of the big electronegativity difference

between nitrogen atoms with other Group V atoms in III-V host materials, such as As in GaAs, deep level states may be formed when nitrogen atoms replace the Group V atoms. So does oxygen in II-VI semiconductors. These states can act as localized isoelectronic defects at low concentration, or form an energy band when their wave-functions are coupled at high concentration. This behavior is described by the Band Anti-Crossing (BAC) model, as expressed in Equation (1.1)[37] .

$$E_{\pm}(k) = \frac{1}{2}\{[E^{C}(k) + E^{L}] \pm \sqrt{[E^{C}(k) - E^{L}]^{2} + 4V^{2}x}\} \qquad (1.1)$$

Where $E^{C}(k)$ is the energy level of the conduction band, E^{L} is the energy level of localized isoelectronic states, and V is the adjusted parameter describing the coupling effect between $E^{C}(k)$ and E^{L}. x is the mole composition of in $GaAs_{1-x}N_x$ or $ZnTe_{1-x}O_x$.

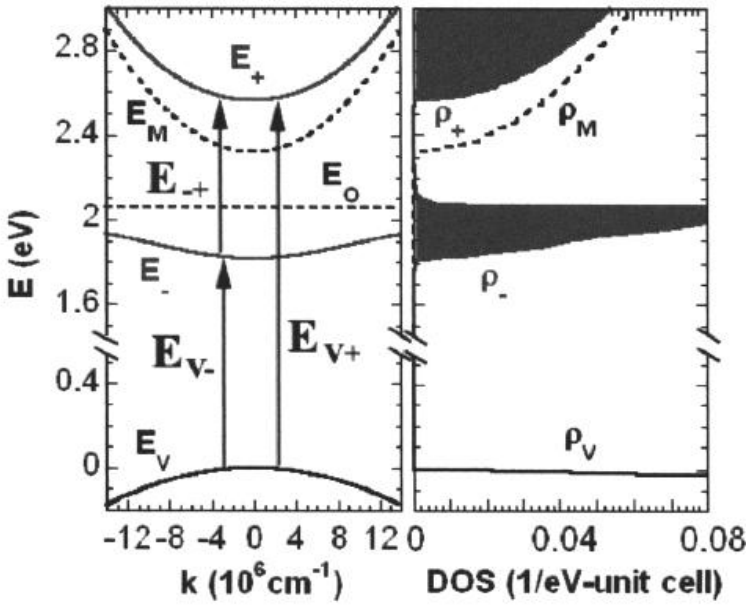

Figure 1.8 The calculated energy band structure (left panel) a density of states (right panel) for zinc telluride alloying with oxygen. Three possible optical transitions are indicated in the left panel[38] .

The band diagram of $ZnTe_{1-x}O_x$ with an intermediate band is predicted based on BAC model, as shown in Figure 1.8. It should be noticed that the band diagrams of $ZnTe_{1-x}O_x$ and $GaAs_{1-x}N_x$ are still not optimized for the best performance of an intermediate band cell. Further band diagram optimization by tuning the band gap may be

achieved by forming ternary alloys, such as ZnCdTe, ZnCdSe, MgCdSe, MgCdTe as shown in Figure 1.9.

Although the idea of an intermediate band solar cell based on the diluted semiconductor alloys is extremely attractive, the experimental research is rarely reported Especially, the internal processes of the real intermediate band cell has never been carefully studied. This thesis aims to intensively explore the operation of an intermediate band solar cell based on ZnTeO material system.

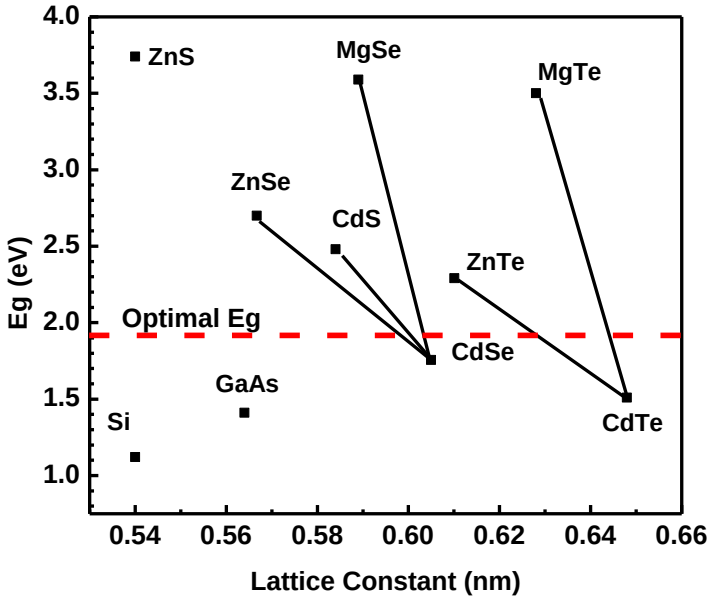

Figure 1.9 Band gap tunabilities of II-VI semiconductor alloys.

1.5 Focus and Organization of Thesis

This work has systematically investigated the operation of an intermediate band solar cell based on ZnTeO material system both experimentally and theoretically coving from ZnTeO material synthesis and characterization, photon-carrier generation, recombination and transportation, and device simulation, fabrication and optimization.

The main contributions of this work are listed as following.

- identified the conditions of synthesizing the radiative oxygen states in ZnTe

- demonstrated the high absorption coefficient (10^4 cm^{-1}) of oxygen states and estimated the relationship between oxygen concentration and absorption coefficient
- verified long recombination lifetime of electron in oxygen states (>1μs) and determined the radiative recombination coefficient (~1.2×10^{-10} $cm^{-3}sec^{-1}$) of oxygen states
- revealed that the electron lifetime in oxygen states can be extended to more than 1ms under an electrical field bias and determined the mechanics of short carrier lifetime at the conduction band of ZnTeO based on analysis of rate equations
- established a device model for operating ZnTeO IBSC including electron occupation of oxygen states which is used to determine the optimal devices parameters and work conditions based on semiconductor device physics
- demonstrated ZnTeO IBSC by a p-ZnTe/n-GaAs hetero-junction with a 100% increase in short circuit current, 15% decrease in open circuit voltage, and overall 50% increase in power conversion efficiency
- confirmed sub-band absorption via a two-photon process by 650nm and 1550nm excitation and illustrated the proposed energy conversion mechanism for IBSC
- demonstrated the improvement of diode character by a ZnSe buffer in n-ZnO/p-ZnTe hetero-junction, which is used to realize a low cost and high efficient ZnTeO based IBSC

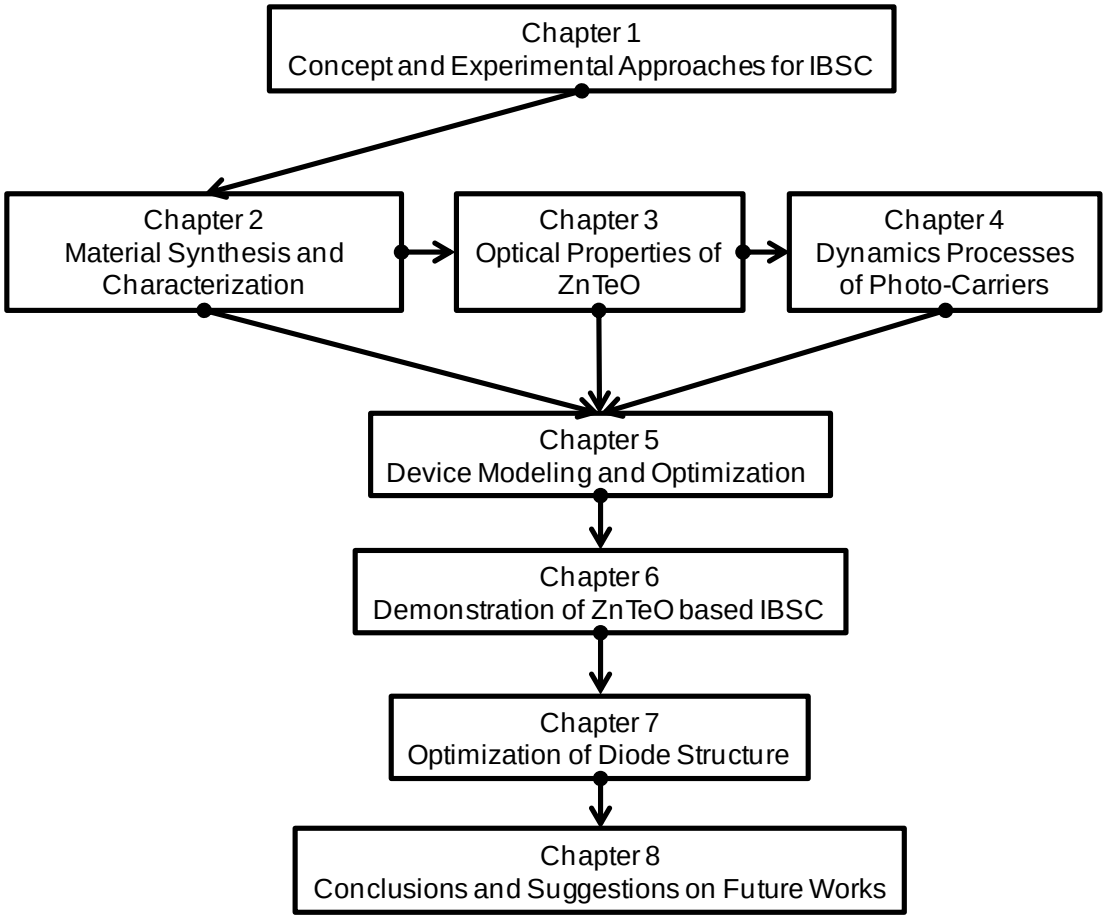

Figure 1.10 Layout of thesis organization.

The layout of this work is illustrated in Figure 1.10.

Chapter 2: Material synthesis with incorporating a wide range of oxygen concentration in ZnTe will be presented. Structural, chemical and electrical properties of ZnTeO also will be described. These studies conclude that high oxygen concentration in ZnTe results in complex tellurium oxide (TeO_x), and low oxygen concentration (below 10^{20} cm^{-3}) is preferred to generate oxygen substitutes of tellurium in ZnTe.

Chapter 3: Optical properties of ZnTeO are explored extensively by reflection, transmission and photoluminescence measurements in order to reveal the role of oxygen states in ZnTe for carrier generation and recombination processes which are most critical to achieving the advantage of Intermediate Band Solar Cells.

Chapter 4: Dynamic processes of photo-carriers are characterized by the time-resolved photoluminescence and analyzed rate equations with and without an electrical field bias including generation, recombination and transportation.

Chapter 5: A theoretical device model for IBSC based on ZnTeO is developed from the fundamental of semiconductor device physics. The theoretical simulation is used to optimize the device parameters and operation conditions for achieving maximum conversion efficiency. Parasite factors in a ZnTe diode are also discussed.

Chapter 6: ZnTeO based IBSC is demonstrated by p-ZnTe/n-GaAs hetero-junctions, confirming extended spectral response below the band edge relative to undoped ZnTe diodes, and enhanced power conversion efficiency. Sub-band gap excitation at 650 nm and 1550 nm also confirms response via a two-photon process and illustrates the proposed energy conversion mechanism for an intermediate band solar cell.

Chapter 7: Optimization effort initially is focused on improve ZnTe based diodes' characters. ZnO/ZnTe hetero-structure is studied aiming to improve its ideal factor and reduce its series resistance. Furthermore the effect of a ZnSe buffer between ZnO/ZnTe is also investigated in order to reduce the interface defects between ZnO/ZnTe

Chapter 8: Summary of thesis work and suggestions on future works to understand about ZnTeO properties and improve the overall conversion efficiency.

Chapter 2

Material Synthesis and Properties of ZnTeO

In this chapter, the synthesis of ZnTe with varying oxygen concentration is presented as a means to introduce intermediate electron states. Structural, chemical and electrical properties of ZnTeO thin films are investigated. The synthesis and properties of ZnO and ZnSe thin films are also presented in the context of their use in solar cell device structures based on ZnTeO absorber layers.

2.1 Introduction to ZnTe and ZnTeO

ZnTe has a direct bandgap of 2.29eV at room temperature with a zinc-blend crystal structure. The bandgap energy corresponds to the green optical wavelength, and has been investigated in great detail for application to ZnSe-based visible light emitters, CdZnTe x-ray detectors, and ZnTe buffer layers for HgCdTe infrared detectors. ZnTe has demonstrated controllable p-type doping by nitrogen[39–42], with hole concentrations of up to 10^{20} cm^{-3}. The source of the unique p-type nature for this wide-bandgap material is believed to be the native defect structure, such as zinc vacancy[43,44], where defects lie within the valence band rather than within the bandgap[45]. The unique p-type behavior of ZnTe is in stark contrast to other wide-bandgap compound semiconductors such as ZnO, where materials are typically n-type and difficult to convert to p-type conduction. The potential of achieving p-type materials with variable bandgap in the visible range make ZnTeO alloys an attractive material for optoelectronic devices. The material properties of ZnTe are listed in the Table 2-1.

Band gap (Eg)	2.29eV at room temperature
Crystal structure	Zinc-blend
Lattice constant	0.6101nm
Native defects	p-type
O_{Te} substitute	0.5eV below E_c

Table 2-1 Material parameters of single crystal ZnTe.

In contrast to to oxygen doping in CdTe where oxygen acts as a shallow acceptor[46], doping or alloying of ZnTe with oxygen is believed to result in a "highly mismatched alloy" where Te and O atoms possess a very different electronegativity. In the extreme of low oxygen concentration, a substitutional impurity of O_{Te} in ZnTe results in a defect level 0.4eV-0.5eV from the conduction band and a strong radiative transition at 1.8-1.9eV[47, 48]. This strong radiative transition in ZnTe:O has in fact been used as red light emitting diode[49] and a phosphorescent material for x-ray detectors, where long radiative lifetimes of > 1μs have been reported[50]. Higher oxygen content in ZnTe is predicted to introduce a narrow electronic band in the material, as explained by a Band Anti-Crossing model [51]. Experiments and calculations have suggested the presence of such an intermediate band in ZnTeO and the quaternary ZnMnTeO[51]. Bandgap reduction in ZnTe with the introduction of oxygen has also been reported[52,53], providing further evidence of an intermediate band in this alloy.

2.2 Material Synthesis Techniques

Molecular Beam Epitaxy (MBE) and Pulsed Laser Deposition (PLD) were used for ZnTe deposition under varying oxygen pressure. The combination of these techniques provides a means to explore a large range of oxygen concentration, where MBE is limited to low oxygen partial pressure and PLD cannot provide the controlled incorporation of oxygen at low partial pressure. Schematics of the PLD and MBE processes are shown in Figure 2.1 (a) and (b) respectively.

In PLD, material is ablated under high vacuum from a sintered target by a pulsed laser beam. Critical deposition parameters include substrate temperature, laser beam power, laser beam repetition rate, and deposition ambient. The ablated material achieves high kinetic energy, enabling deposition under relatively high oxygen partial pressure. In

this work, samples were deposited on both c-plane sapphire and GaAs (001) substrates using a ZnTe target, KrF excimer laser (λ=248nm, 20ns pulse width, 6Hz repetition rate), deposition temperature of 300 ^{o}C, and varying ambients of high vacuum (<5x10^{-6} Torr), nitrogen, or oxygen. Deposition by PLD under nitrogen or oxygen conditions were done with partial pressure in the range of 10-100mTorr. Nitrogen incorporation is studied in this work as an experimental control, allowing separate comparison of differing chemical species and differing deposition partial pressure. The growth rate under these conditions was varied from approximately 0.4nm/s to 1.1nm/s, with sample thickness in the range of 0.7 μm to 1.9 μm.

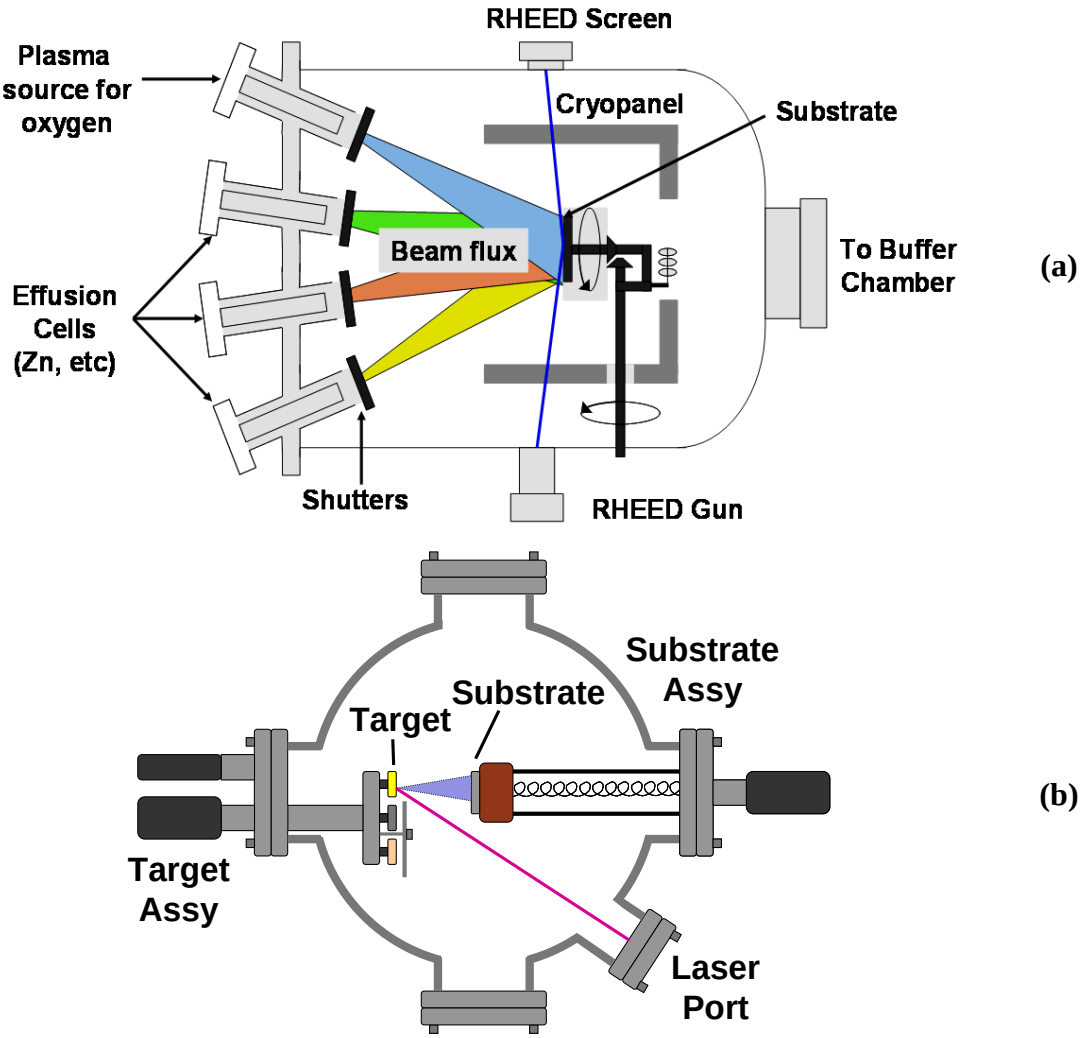

Figure 2.1 Schematics of (a) Molecular Beam Epitaxy (b) Pulsed Laser Deposition

The MBE technique utilizes separate elemental sources to grow material on a heated substrate under ultra-high vacuum. In contrast to PLD, MBE utilizes thermal effusion cells where source flux contains relatively low kinetic energy. Therefore, MBE was used to study ZnTeO growth under low oxygen partial pressure. MBE growth was performed with a base pressure near 10^{-9} Torr at a substrate temperature of 250^{o}C using zinc and tellurium solid source effusion cells, and a microwave plasma source to introduce oxygen or nitrogen. Oxygen or nitrogen flow rates of up to 1sccm were used, corresponding to a partial pressure of up to 10^{-5} Torr. ZnTe and ZnTeO samples grown by MBE were performed on GaAs (001) substrates, providing a suitable template for zinc-blend ZnTe with low concentration of oxygen or nitrogen. The MBE growth rate is in the range of 0.1~0.4nm/sec. The thickness of the samples for the following study is in the range of 1-2 μm. The process of introducing oxygen by a microwave plasma source is attached in Appendix I.

2.3 Structural Properties

The structural, chemical, and optical properties of the ZnTeO thin films were investigated to study the influence of oxygen incorporation in ZnTe. X-ray diffraction θ-2θ scans were used to determine crystal structure and crystalline orientation.X-ray diffraction measurements for ZnTe samples grown by PLD and MBE on GaAs (001) are shown in Figure 2.2 (a) and (b), respectively. In the absence of oxygen, zinc-blend ZnTe (001) is observed for both PLD and MBE growth, corresponding to epitaxial growth on GaAs (001). The introduction of nitrogen or oxygen during the PLD process resulted in the degradation of the ZnTe (002) and (004) crystalline reflections and absence of additional peaks that would correspond to alternative crystalline structures or orientations. High incorporation of oxygen likely results in the formation of complex oxide compounds, such as TeO_2, $Zn(TeO_3)$, and $Zn(TeO_4)$ All of the samples grown by MBE, including those with oxygen and nitrogen plasma, demonstrated ZnTe (002) and (004) reflections, indicating a clear ZnTe (001) orientation on GaAs (001). The introduction of oxygen resulted in a decrease in the peak intensity and increase in the linewidth of ZnTe reflections, indicating some degradation in crystalline quality. This degradation in crystalline structure was more pronounced for samples grown with nitrogen.

X-ray diffraction θ–2θ scans of ZnTe films grown on c-plane sapphire substrates by PLD and MBE exhibit different crystalline orientation in comparison to growth on GaAs (001), as shown in Figure 2.3. ZnTe deposited by MBE on sapphire (0001) with low oxygen and nitrogen flow exhibit poly-crystalline material with a dominant zinc-blend (111) orientation. The ZnTe (111) preferential orientation on sapphire (0001) is likely due to the hexagonal atomic arrangement of these two faces. ZnTe deposited by PLD under high oxygen and nitrogen pressure exhibit weak diffraction peaks corresponding to polycrystalline zinc-blend material, suggesting a low degree of crystallinity and/or amorphous material. There is no evidence of the wurtzite structure of ZnTeO for any of the samples studied.

The cyrstalline structure of ZnTe thin films grown by MBE on Si (100) substrates and ZnO c-plane orientated thin films were also investigated. The X-ray diffraction θ–2θ scanning curves, as shown in Figure 2.4, indicate that ZnTe thin films are poly-crystalline without preferential orientation on Si (100) substrates, and predominant (111) orientated on c-plane ZnO thin films.

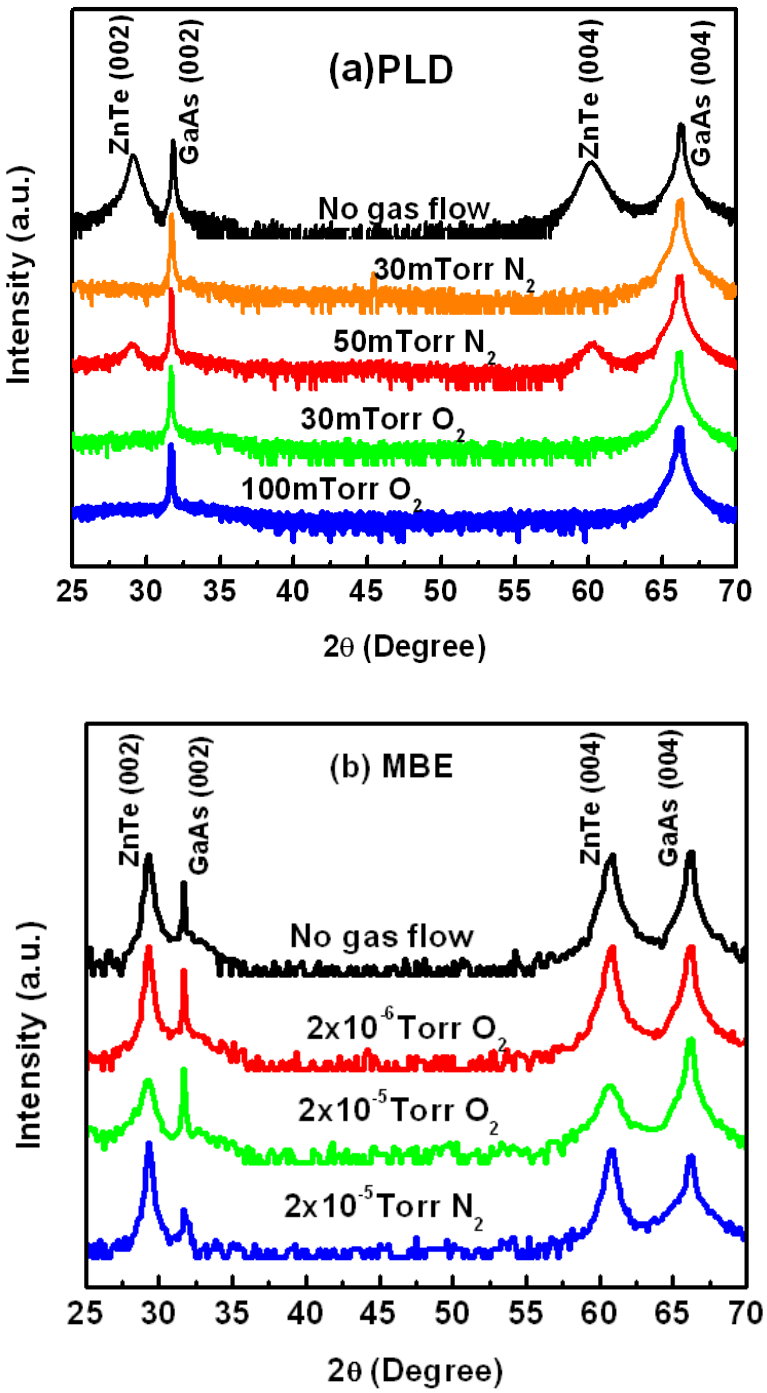

Figure 2.2 X-ray diffraction θ-2θ measurements of (a) ZnTe deposition by PLD under varying oxygen and nitrogen partial pressure on GaAs substrate, (b) ZnTe growth by MBE with and without the introduction of oxygen or nitrogen by a plasma source on GaAs substrate.

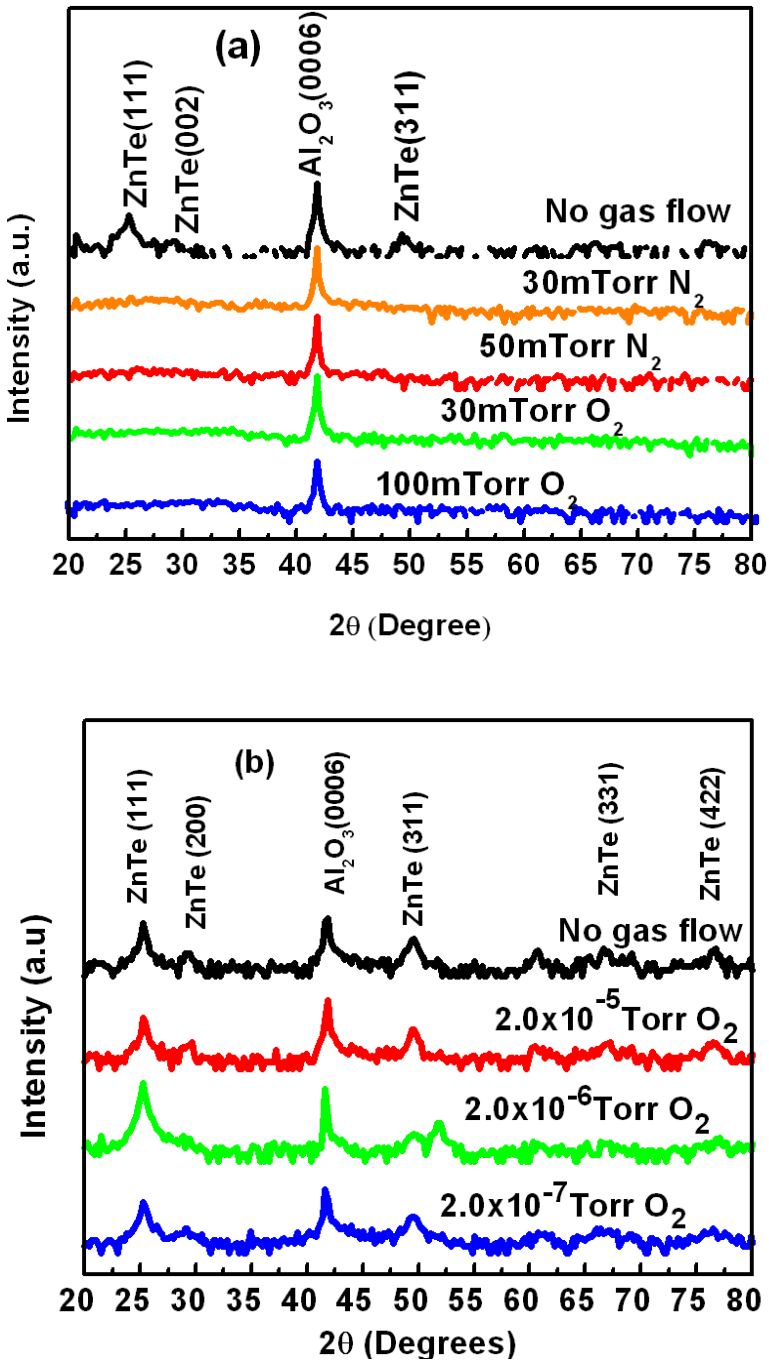

Figure 2.3 X-ray diffraction θ-2θ measurements of ZnTe on c-sapphire substrate (a) deposition by PLD under varying oxygen and nitrogen partial pressure and (b) growth by MBE with and without the introduction of oxygen or nitrogen by a plasma source.

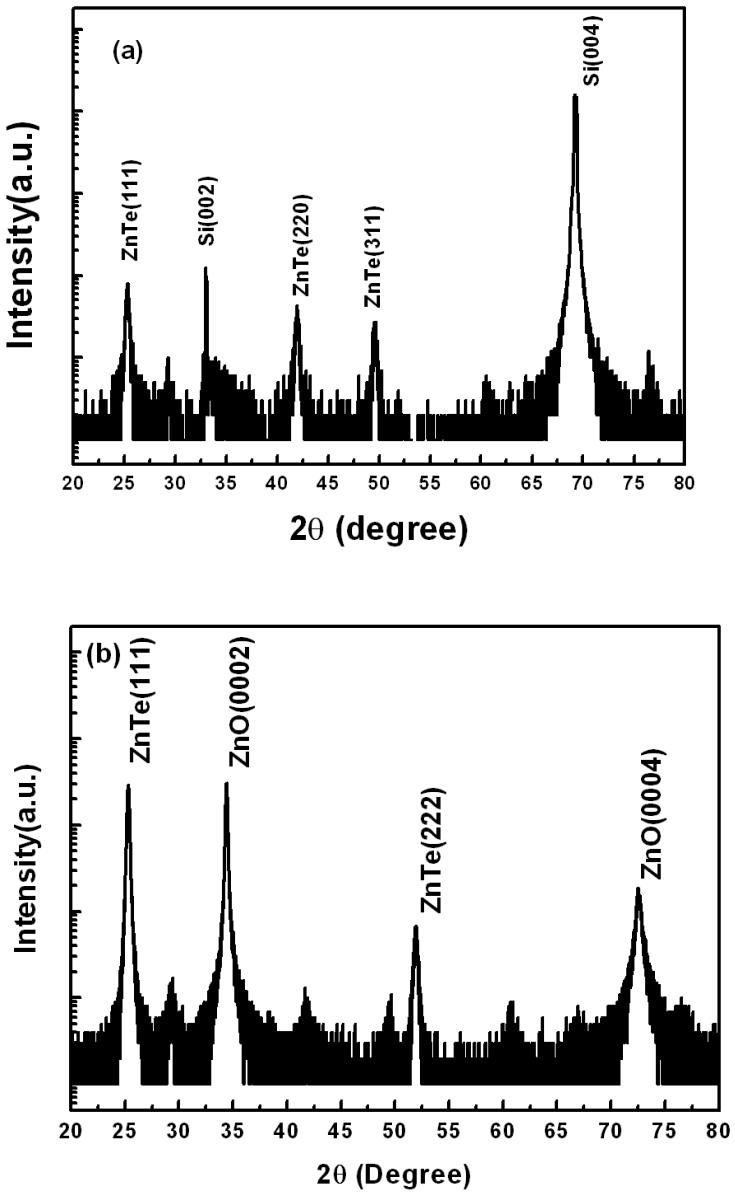

Figure 2.4 X-ray diffraction θ-2θ measurements of ZnTe grown by MBE (a) Si (001) substrate (b) c-plane ZnO substrate.

The polycrystalline structure observed for ZnTe growth on silicon is attributed to the inability to properly remove the native oxide on the silicon substrates. The removal of this oxide requires a high substrate temperature (>800^{o}C), which could not be obtained using the MBE substrate heater available in this study. The depositon of ZnTe on ZnO substrates is limited by the structural quality of the ZnO thin films, which were polycrystalline thin films deposited by PLD on sapphire. The highest quality ZnTe layers

were samples grown on GaAs substrates, where the ZnTe/GaAs process was selected to carry on a majority of the remaining studies on material properties and associated devices.

2.4 Chemical Properties

Relative concentrations of oxygen, nitrogen, and associated bonding configurations were determined using X-ray photoelectron spectroscopy. XPS measurements focusing on the tellurium signal for samples grown by PLD and MBE are shown in Figure 2.5(a) and (b), respectively. PLD samples deposited without oxygen or nitrogen show a clear peak corresponding to Te3d 3/2 and 5/2, the internal electron energy levels. PLD deposition under nitrogen ambient shows degradation of these peaks. PLD deposition under oxygen ambient shows a clear degradation and disappearance of the Te3d 3/2 and 5/2 peaks, and appearance of TeO_2 3/2 and 5/2 peaks indicating the formation of tellurium oxide. XPS measurements of all MBE samples measured indicate the presence of only Te3d 3/2 and 5/2 peaks, both with and without oxygen incorporation. There are at least three sites oxygen atoms may occupy in the ZnTe crystal, as shown in Figure2.6. No TeO_2 3/2 and 5/2 peaks could be identified for XPS scans on MBE samples, suggesting that the formation of tellurium oxide compounds is negligible under the MBE growth conditions studied. This data suggests that oxygen atoms likely occupy tellurium sites or interstitial sites rather than zinc sites. For oxygen-doped ZnTe films grown by MBE under all oxygen partial pressure from 2.0×10^{-7} Torr to 2.0×10^{-5} Torr, oxygen concentration is too low to be detected by XPS measurement. Assuming similar incorporation rates for nitrogen and oxygen using the ECR source, the oxygen concentration in ZnTe grown with 2×10^{-5} Torr oxygen partial pressure is estimated to be near $10^{19}cm^{-3}$.

For PLD samples, the higher oxygen content provided a means of estimating oxygen concentration, where the stoichiometry of films grown under 30mTorr oxygen was determined to be Zn:Te:O=0.49:0.26:0.25. The stoichiometry for ZnTeO deposited under 100mTorr oxygen is Zn:Te:O=0.45:0.24:0.31. There is a clear zinc deficiency for samples deposited under high oxygen pressure. The oxygen densities are more than 10^{22} cm^{-3} for these stoichiometry conditions.

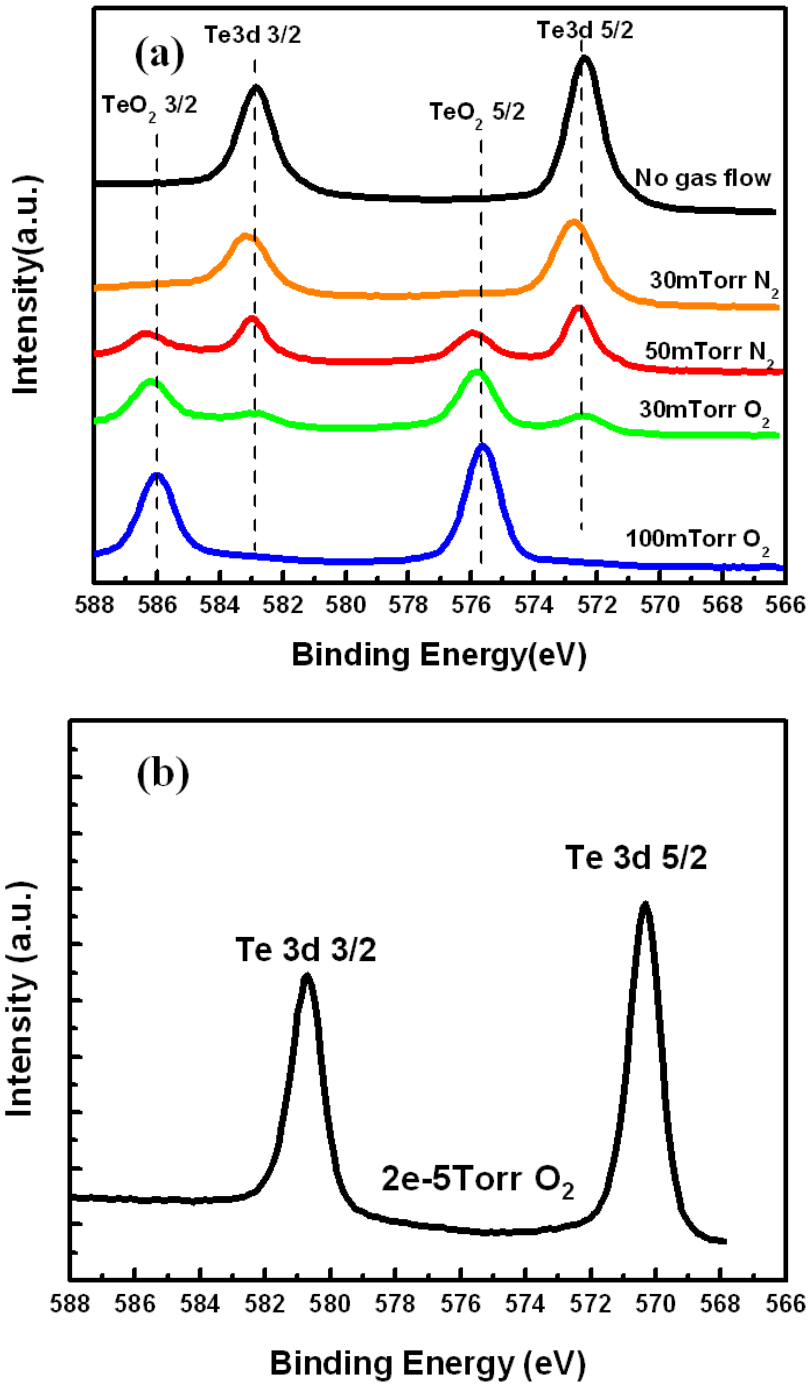

Figure 2.5 X-ray photoelectron spectroscopy of (a) ZnTe samples deposited by PLD under varying oxygen and nitrogen partial pressure and (b) a representative ZnTe sample grown by MBE with 0.1sccm oxygen flow through a plasma source.

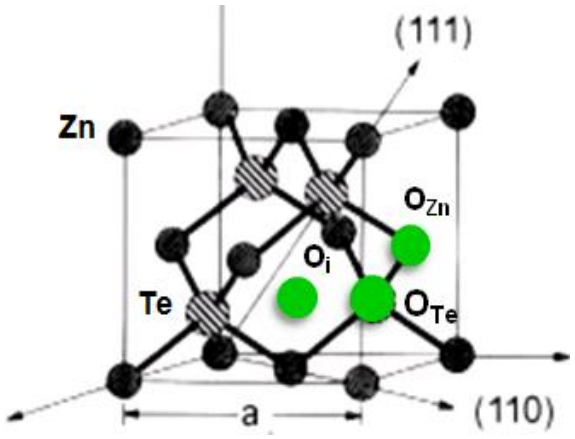

Figure2.6 Schematics of possible oxygen sites in ZnTe crystal

2.5 Electrical Properties

ZnTe films deposited by MBE without intentional doping were determined to be p type with hole concentration in the range of 10^{14}-10^{15} cm^{-3}. Capacitance-voltage (C-V) measurements on n^+-ZnO/p-ZnTe structures were used to determine these values due to the difficulty in achieving ohmic contacts for samples with low carrier concentration. The electron concentration of the ZnO layer is approximately 5×10^{18} cm^{-3}, providing an asymmetric doping profile to aid in analysis. Equation (2.1) is used to determine carrier concentration in ZnTe, where q is the charge of an electron, $\varepsilon=7.4\,\varepsilon_0$ is the static dielectric constant of ZnTe, and A is device area. Representative data for a junction with $A=0.01cm^2$ is shown in Figure 2.7, where an acceptor concentration of $p=5\times10^{14}$ cm^{-3} is determined. Based on the background p-type doping concentration, the Femi-level is approximately 0.3 eV above the edge of the valence band at room temperature under thermal equilibrium.

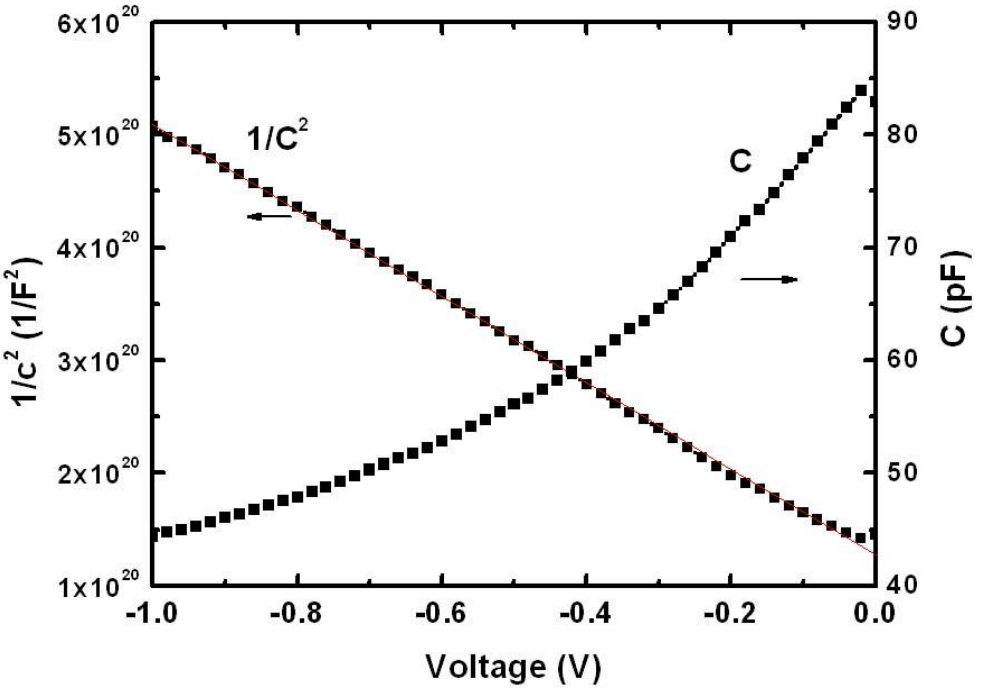

Figure 2.7 C-V and $1/C^2$-V curves of n^+-ZnO/p-ZnTe junction .

$$N_A = \frac{2}{q\varepsilon\ A^2 d(1/C^2)/dV} \tag{2.1}$$

Nitrogen doping of ZnTe was investigated in this study to provide p-type material with higher conductivity. Nitrogen doped ZnTe thin films on GaAs substrates grown by MBE show high p-type conductivity with hole concentration of 10^{19} cm^{-3} and mobility 40 cm^2/V.s. The formation of n-type ZnTe remains a major challenge, where reports have only experimentally demonstrated n-type behavior for ZnTe epitaxial growth on ZnTe substrates[54].

2.6 Summary

The material properties of ZnTe thin films with oxygen concentration at the range of 10^{17}-10^{21} cm^{-3} have been explored. These studies conclude that high oxygen partial pressure in ZnTe growth likely results in complex tellurium oxide (TeO_x), and low oxygen partial pressure is preferred to generate oxygen impurities in the ZnTe crystal, such oxygen tellurium substitutional impurities and oxygen interstitials. ZnTe thin films grown on GaAs by MBE demonstrate epitaxial growth with background hole concentration of 10^{14}-$10^{15}$$cm^{-3}$, serving as a baseline for study of ZnTeO materials for

intermediate band solar cells. ZnO and ZnSe thin films demonstrate n-type conduction suitable for heterojunctions with ZnTe.

Chapter 3

Optical Properties of ZnTeO

In this chapter, optical properties of ZnTeO are explored intensively by reflection, transmission and photoluminescence measurements in order to reveal the role of oxygen states in ZnTe for carrier generation and recombination processes which are most critical to achieving the advantage of Intermediate Band Solar Cells (IBSC).

3.1 Reflection and Transmission

Optical reflectance spectra were used to determine layer thickness and to approximate optical absorption characteristics. Optical transmission measurements were performed on the ZnTeO samples deposited on c-plane sapphire substrates to determine optical absorption spectra.

The samples grown by PLD under varying oxygen and nitrogen ambient demonstrate dramatic changes in optical transparency, as shown in Figure 3.1 (a). Visual inspection of samples grown on sapphire indicate samples changing from a red color to increasing transparency for increasing oxygen partial pressure, while becoming increasingly opaque for increasing nitrogen pressure. Optical reflectance measurements Figure 3.1(b) are consistent with the changing optical transparency, where reduced attenuation of interference fringes is observed at higher energies for increasing oxygen partial pressure. Optical transmission spectra also support these observations Figure 3.1 (c), where an increasing optical transparency is observed at short wavelengths for increasing oxygen partial pressure, and a decrease in transparency for nitrogen incorporation. It should be noted that while an optical transparency change is observed for increasing nitrogen or oxygen pressure, the turn-on characteristic has a more gradual slope.

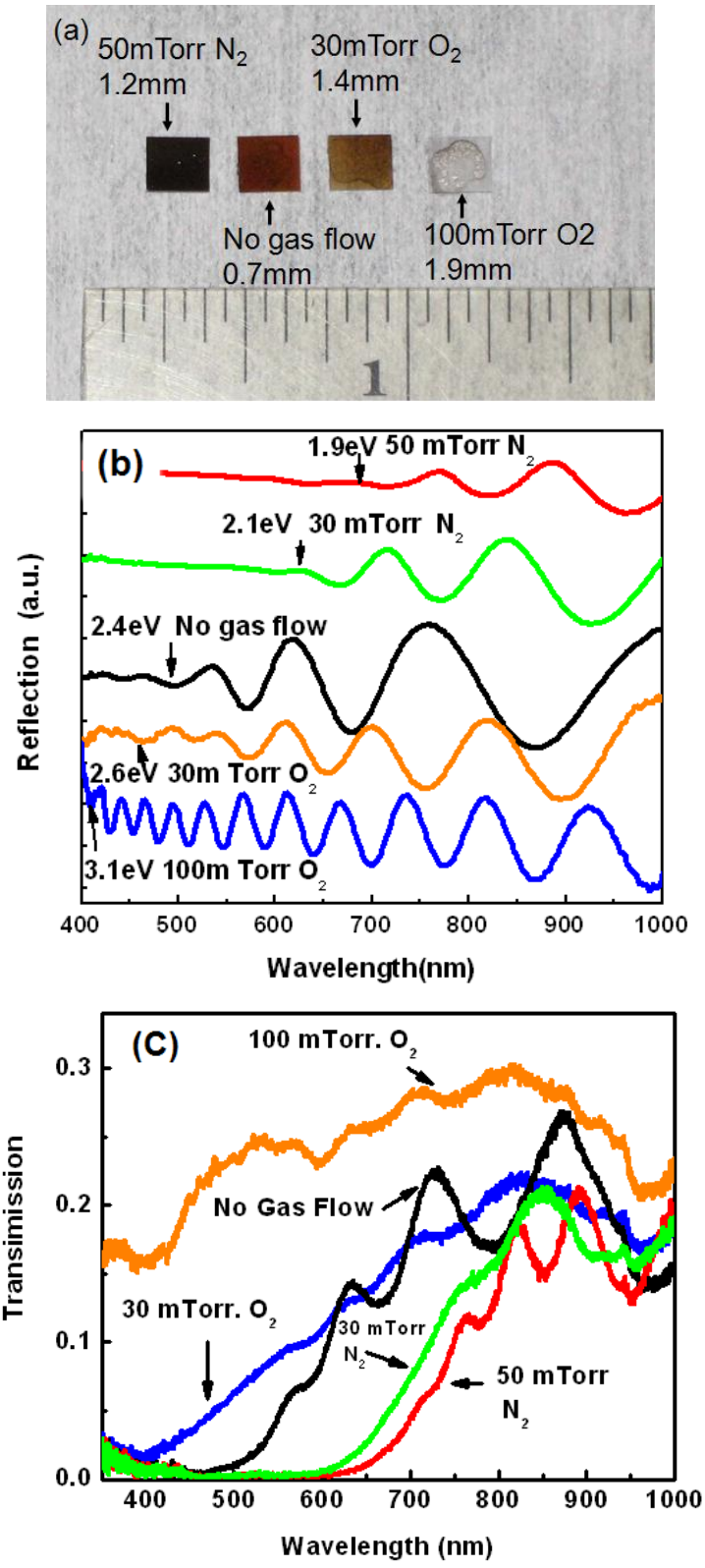

Figure 3.1 Optical transparency of ZnTe samples deposited by PLD under varying oxygen and nitrogen partial pressure as shown by (a) photograph (b) reflectance spectra, and (c) transmission spectra.

The PLD process under the conditions of high oxygen or nitrogen partial pressure provides dramatic changes in optical transparency. These changes are attributed to the formation of tellurium oxide (oxygen incorporation) whose optical transmission range is from 330nm to 5000nm, or incorporation of nitrogen acceptors (nitrogen incorporation). The formation of tellurium oxide is apparent based on XPS measurements where TeO_2 bonding is observed, increased optical transparency corresponding to the larger bandgap of this material, and lack of crystal structure observed by x-ray diffraction, which have been shown in Figure 2.3 (a) and Figure 2.5 (a). The gradual transmission spectra observed for oxygen incorporation, and presence of Te3d bonding in XPS, suggests that these thin films consist of a composite of both ZnTe and amorphous TeO_x. The formation of crystalline semiconducting Zn (Te,O) alloys is clearly inhibited for the PLD process under the conditions studied, possibly requiring the introduction of reactive oxygen in the form of a plasma source or ozone. However, the formation of the amorphous ZnTeO composite may provide a valuable technique for integrated optical/electronic devices based on this material system where optically transparent and/or electrically insulating layers are needed.

In contrast, the optical transparency of samples with ZnTeO films on sapphires by MBE all demonstrate a shift to lower energy with respect to undoped ZnTe for both oxygen and nitrogen incorporation. The shifts in optical reflectance observed are less dramatic than those observed for PLD samples. The optical reflectance spectra for four MBE samples with varying oxygen partial pressures are shown in Figure 3.2 (a), indicating an increased optical attenuation below the ZnTe bandedge for higher absorption states related to higher oxygen partial pressure. Optical transmission spectra of samples with varying oxygen pressure clearly show increased absorption at energies below the ZnTe bandgap Figure 3.2(b). In contrast to the gradual shift in transmission observed for PLD samples, oxygen incorporation in the MBE samples demonstrates a resonant-like behavior near 650nm (1.9eV). Transmission curves were used to extract the optical absorption coefficient.

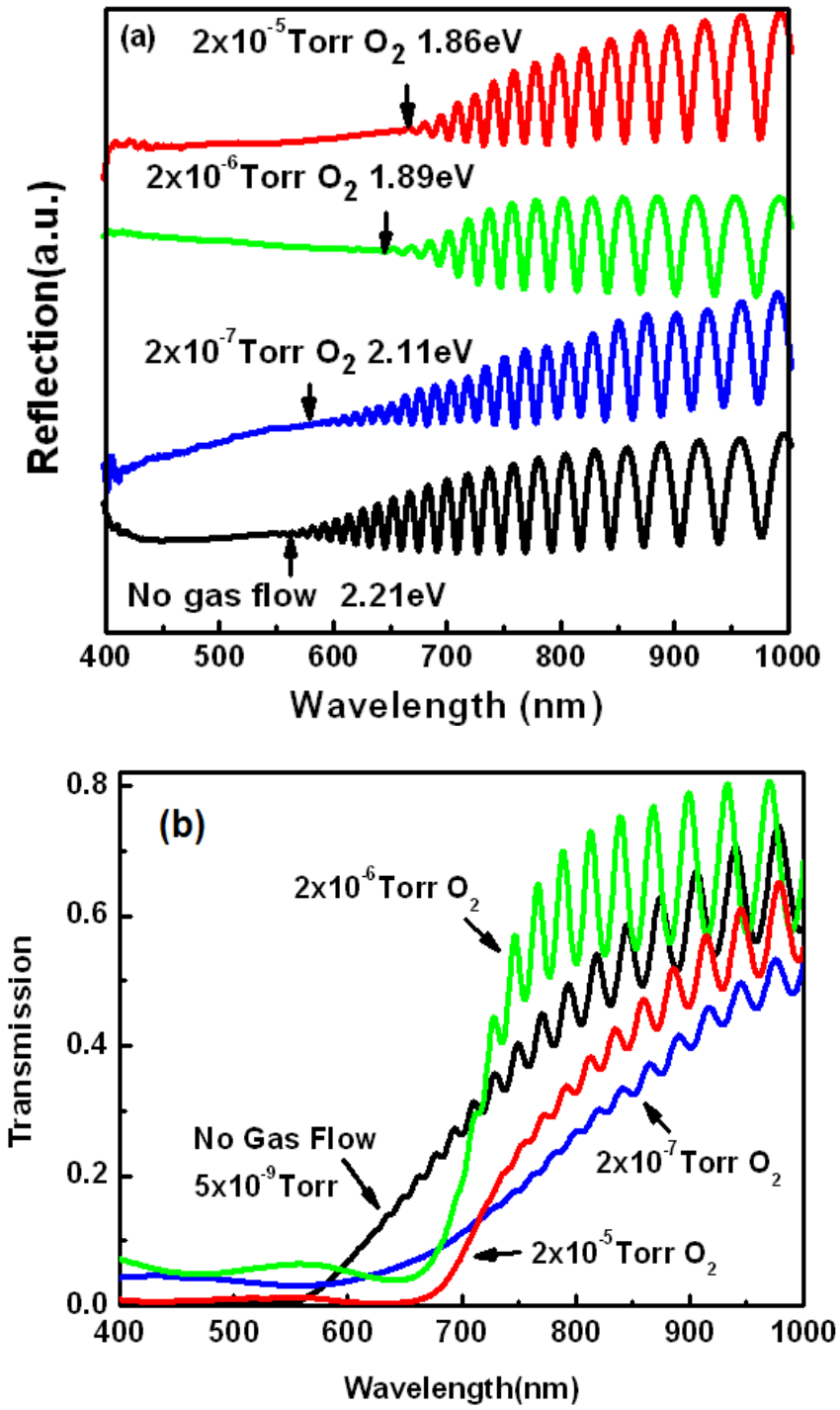

Figure 3.2 Optical transparency of ZnTe samples grown by MBE with oxygen plasma as shown by (a) reflectance spectra and (b) transmission spectra.

3.2 Absorption Coefficient

A model for optical transmission for a two-layer (ZnTe or ZnTeO/on sapphire substrate) film can be expressed as follows

$$T = \frac{(1 - R_1 T_x) e^{-\alpha d}}{1 - R_1 R_x e^{-2\alpha d}} \tag{3.1}$$

where α is the optical absorption coefficient and d is the layer thickness. The transmission (T_x)_and reflection (R_x) coefficients are then given by

$$T_x = \frac{(1 - R_2)(1 - R_3)}{1 - R_2 R_3} \tag{3.2}$$

$$R_x = R_2 + \frac{R_3 (1 - R_2)^2}{1 - R_2 R_3} \, . \tag{3.3}$$

In equations (3.1), (3.2) and (3.3), $R_1=(1-n_1)^2/(1+n_1)^2$, $R_2=(n_1-n_2)^2/(n_1+n_2)^2$ and $R_3=(n_2-1)^2/(n_2+1)^2$ are the interface reflectivities for air/ZnTe(or ZnTeO), ZnTe (or ZnTeO)/sapphire, and sapphire/air, respectively, where n_1 and n_2 are wavelength-dependent refractive indices of ZnTe[55] and sapphire. The refraction index of ZnTeO is assumed to be the same as ZnTe. The interference fringes below absorption edges were removed by a fast Fourier transfer filter[56]. The extracted absorption coefficient spectra of ZnTe and ZnTeO are shown in Figure 3.3. An absorption coefficient of oxygen states as high as $10^4 cm^{-1}$ has been achieved under oxygen partial pressure at 10^{-5}Torr.

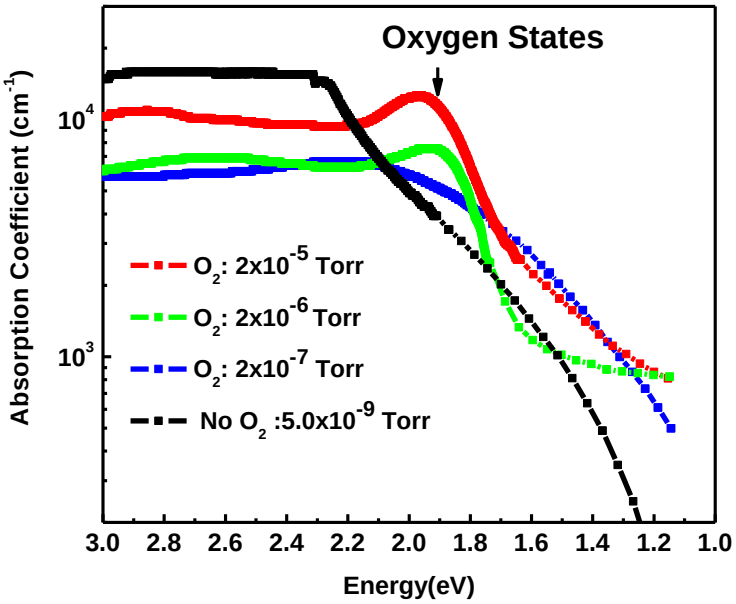

Figure 3.3 Absorption coefficients of ZnTe samples grown by MBE with oxygen plasma extracted from transmission measurements.

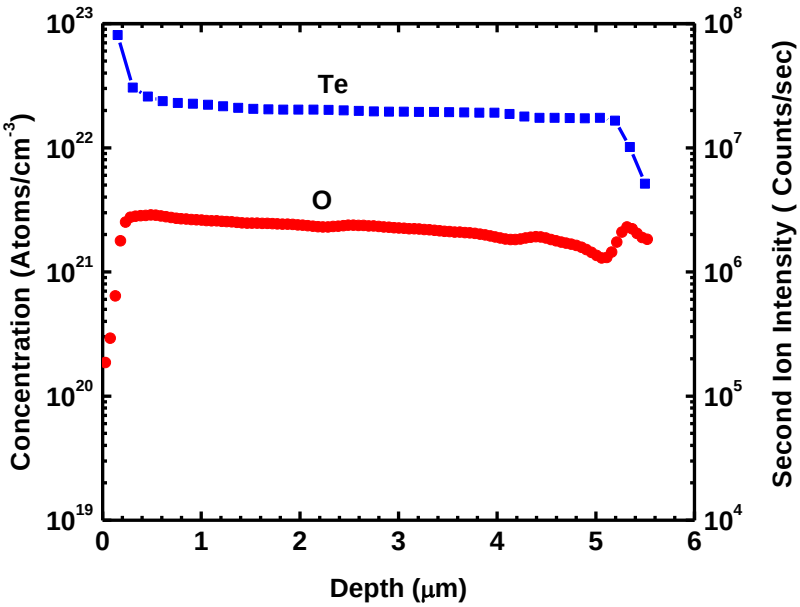

Figure 3.4 Oxygen concentration in ZnTeO/sapphire measured by SIMS.

The oxygen concentration of one of ZnTeO/sapphire samples grown under 2×10^{-7} Torr. oxygen partial pressure used for absorption coefficient estimation is measured by SIMS, as shown in Figure 3.4. The oxygen density is maintained at 2×10^{21} cm^{-3} in the

bulk region from the depth of 0.3μm to 5.5 μm, but falls to near 10^{20} cm^{-3} in the surface region with depth smaller than 0.3μm possibly due to diffusion process from the bulk to atmosphere. Oxygen atoms measured by the SIMS measurement include all formation of oxygen states including interstitial oxygen impurity, substitutional oxygen impurity (O_{Te} and O_{Zn}), and other complexes. However, only O_{Te} states are confirmed to contribute the absorption peaks near 1.8eV. The ratio of O_{Te} states to other oxygen states under MBE growth is uncertain.

The MBE samples studied in this work clearly show that Zn(Te,O) alloys are achievable in the ZnTe zinc-blend crystal structure. The previous X-ray diffraction measurements indicate slight degradation in the crystal structure, but this degradation is relatively minor in comparison to nitrogen doping. The previous XPS measurements indicate that oxygen incorporation is primarily due to O-Te substitution, rather than the formation of TeO_x. The resonant-like optical absorption below the ZnTe bandedge for samples grown with oxygen indicates the presence of an efficient optical transition corresponding to an optically active defect level or ZnTeO alloy with intermediate band or large bandgap bowing. For oxygen concentration lower than a threshold value[57], typically near 10^{18} cm^{-3}, the oxygen state is localized. The energy level of the oxygen state is fixed at 0.4eV below the conduction band edge where the energy level is determined by the difference of eletronegativity between atomic oxygen and tellurium[,58]. With increasing oxygen concentration, oxygen states will be coupled as oxygen-oxygen pairs, or oxygen clusters[59, 60] with energy level shifting further away from the conduction band. With a further increase in oxygen concentration, typically Te/O ratio of 1%, an intermediate band may be formed whose energy level shifts with oxygen concentration[51]. At higher oxygen concentration, a phase separation is believed to occur due to the differing crystal structure for ZnTe and ZnO. Tellurium oxide may also be formed as demonstrated in our ZnTeO films grown by PLD. The extreme case of ZnTeO is tellurium doped ZnO, where the valance band of ZnO may be shifted to higher energy[61]. The optical transitions observed in our samples are believed to result from oxygen pairs or oxygen clusters instead of the formation of an intermediate band alloy where a shift with oxygen concentration would be expected. The large absorption coefficient observed,

however, is more consistent with a high density of states that would be typically observed for a defect level transition.

3.3 Photoluminescence

3.3.1 Room Temperature PL

Photoluminescence measurements were also used to more carefully identify the band edge and associated spontaneous emission transitions. The undoped ZnTe, oxygen doped ZnTe, and nitrogen doped ZnTe grown by MBE on intrinsic GaAs substrates were were measured by photoluminescence at room temperature with a HeCd laser operating at 325nm.

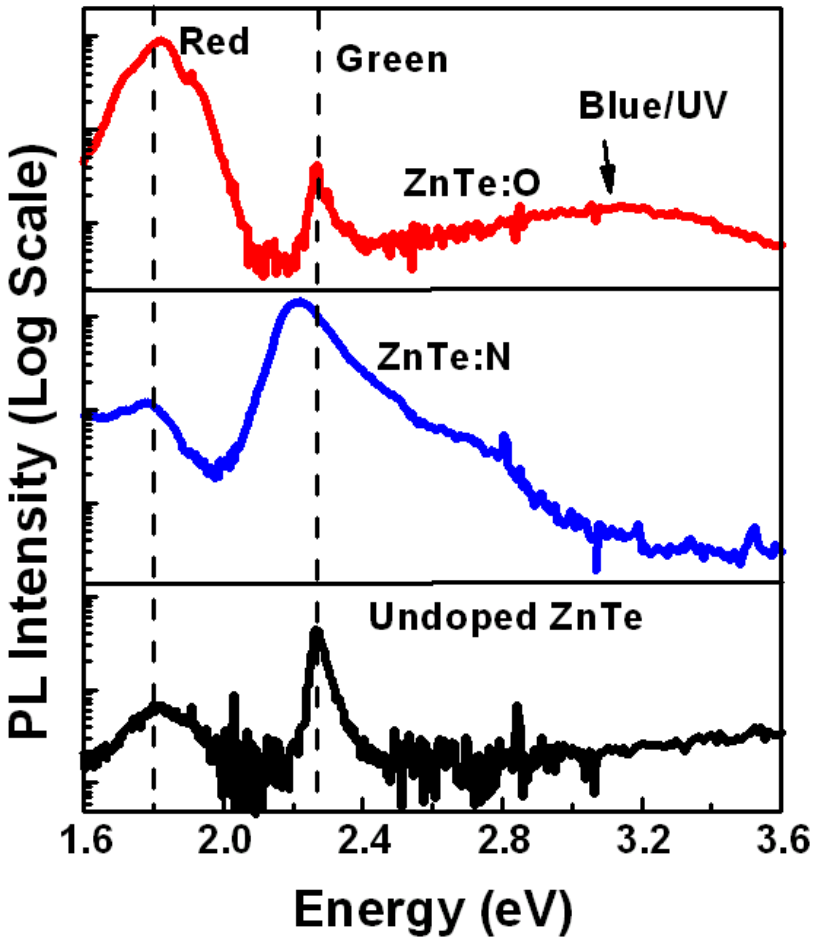

Figure 3.5 Room temperature photoluminescence spectra of undoped, nitrogen-doped and oxygen-doped ZnTe.

Photoluminescence spectra are shown in Figure 3.5. Samples deposited by PLD only demonstrated weak PL emission, which degraded further upon oxygen and nitrogen doping, and were therefore not studied in this work. MBE samples grown without nitrogen or oxygen demonstrate a predominant peak near 2.3eV, corresponding to the ZnTe bandedge. Emission at longer wavelength, near 1.8eV, is also observed and attributed to deep level defects and/or unintentional background oxygen incorporation due to residual oxygen in the growth chamber or incorporation of oxygen into the zinc source and the tellurium source. For ZnTe with nitrogen incorporation, the band edge transition becomes broadened and moves to a lower energy near 2.2eV. The altered band edge emission may be attributed to the incorporation of nitrogen acceptor states. For oxygen doping, a dramatic increase in net PL emission is observed with a dominant transition near 1.8 eV. The spectral position of the optical transition near 1.8eV observed in optical absorption and PL spectra for oxygen-doped samples is consistent with previously reported oxygen defects in ZnTe [62, 63]. In addition to the dominant peak at 1.8eV, oxygen doped samples exhibit a peak at 2.3eV corresponding to ZnTe, as well as a peak in the 3.0-3.4eV range that may be related to the formation of ZnO or a related ZnOTe alloy.

3.3.2 Temperature Dependent PL

The temperature dependent photoluminescence spectra provide more information on the spontaneous emission from the band edges and oxygen states. Measurements were performed on an oxygen doped ZnTe sample grown on a GaAs substrate by MBE. Three temperature regions are observed based on integrated luminescence intensity of the band-to-band transition (CB-VB, or the green band from 520nm to 560nm). In the first region from 10K to 80K, the intensity of both the green band and the red band (radiative emission from 630nm to 710nm) decrease monotonically as shown in Figure 3.6 (a). The peak intensity of the green band is higher than the peak intensity of the red band for temperatures below 20K. However, the green band peak intensity decreased more rapidly than the red band with increasing temperature. Both the green band and the red band consist of multiple peaks. The red band emission from 650nm to 680nm is attributed to O_{Te} substitutional impurities, where the fine structure at low temperature has been

described as multi-phonon coupling[64,65]. The red peak at 700nm may also be related to oxygen states in ZnTe as complex defects. The green emission at 535nm is attributed to an acceptor bound exciton (A^0X), and the peak at 525 nm may result from free exciton (FE) emission as shown in Figure 3.6 (b). Intensities of both A^0X and FE peaks decrease with temperature.

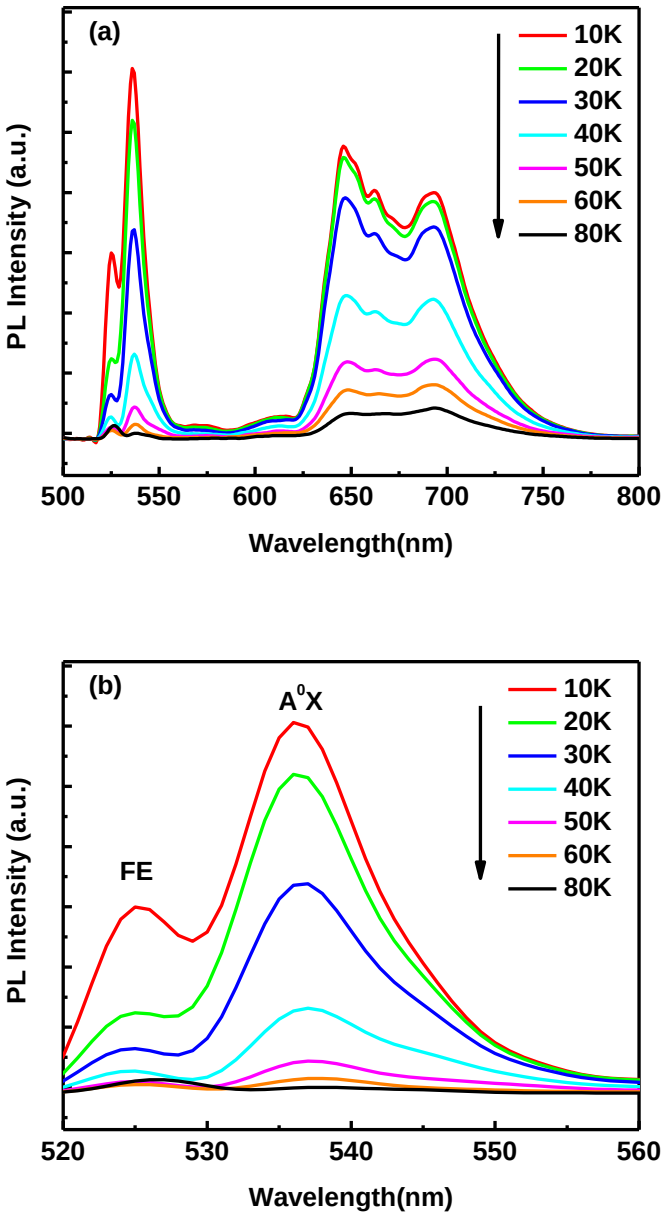

Figure 3.6 Temperature dependent photoluminescence spectra of ZnTeO on GaAs from 10K to 80K (a) full bands from 500nm to 800nm (b) greed band from 520nm to 560nm.

In the second temperature region from 80K to 120K, the intensity of the green band increases with temperature, while the red band does not follow a consistent change with temperature, as shown in Figure 3.7 (a) and (b). The intensity of the A^0X peak decreases with temperature, while the FE emission increases with temperature, with an overall increase in intensity of the green band. The FE peak and A^0X peak exhibit a red shift with increasing temperature following the Varshni relation for the bandgap energy change with temperature[66]

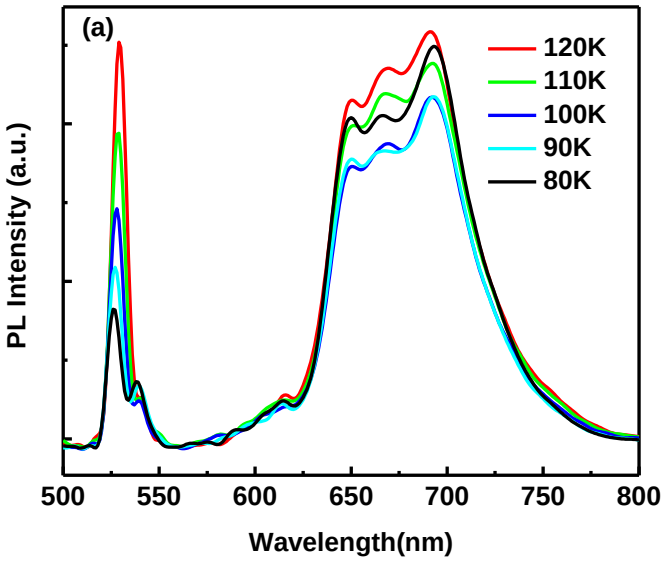

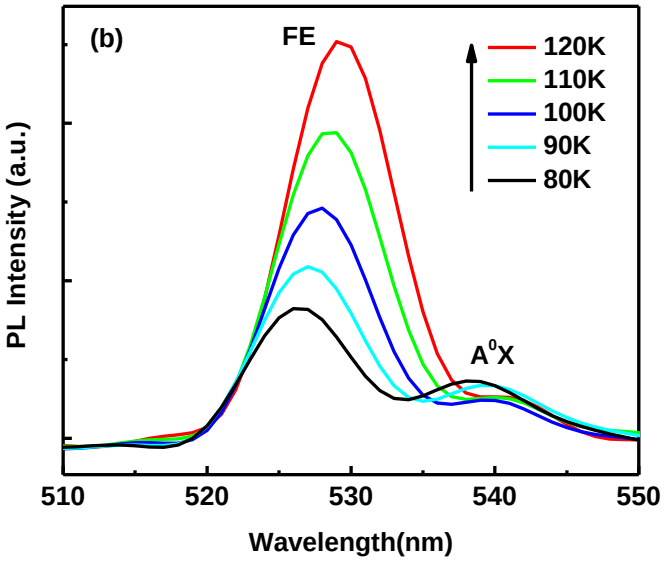

Figure 3.7 Temperature dependent photoluminescence spectra of ZnTeO on GaAs from 80K to 120K (a) full bands from 500nm to 800nm (b) greed band from 510nm to 550nm.

In the third temperature region from 120K to 280K, the intensity of the green band decreases with temperature, while the intensity of the red band increases with temperature, as shown in Figure 3.7 (a). The peak energy of the green band emission demonstrates a strong red-shift from 530nm to 547nm corresponding to a combination of the band gap decrease with temperature and dissociation of the free excitons with increasing temperature. The binding energy of excitons in ZnTe is approximately 12.8meV[66], corrponding to a thermal energy kT at approximately 150 K.

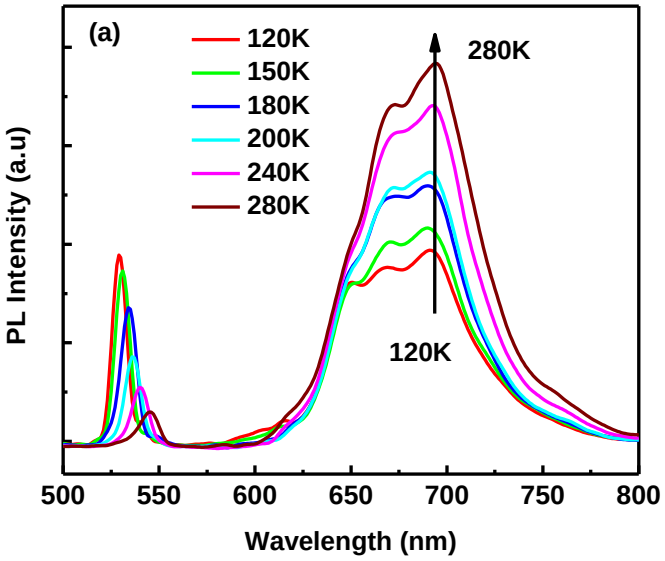

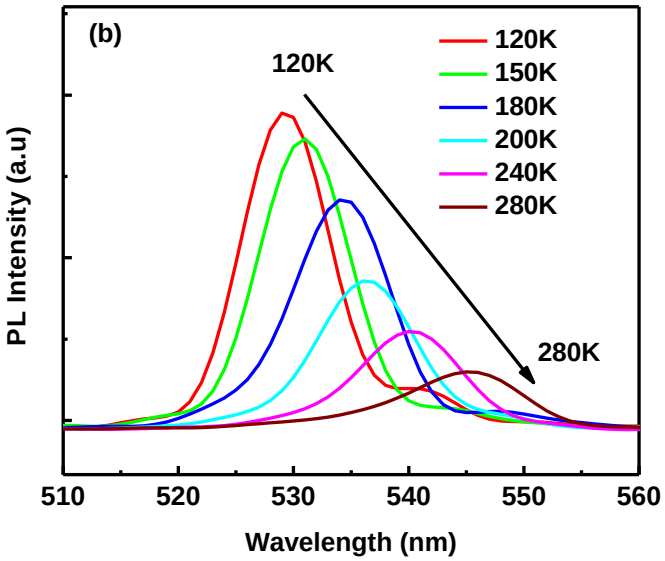

Figure 3.8 Temperature dependent photoluminescence spectra of ZnTeO on GaAs from 120K to 280K (a) full bands from 500nm to 800nm (b) greed band from 510nm to 550nm.

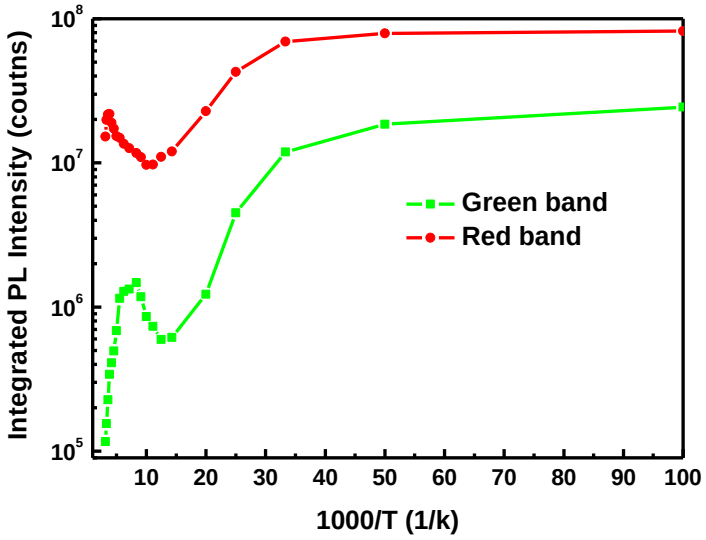

Figure 3.9 Integrated PL intensities of the green band and the red band varying temperature from 10K to 300K.

The temperature dependence of the integrated PL intensity for the green band and the red band are shown in Figure 3.9. A local minimum and maximum are observed for

both the green band and the red band, and may indicate electron transfer by thermal emission and capture processes between these two bands, which has similarly been observed in AlGaAs/InGaAs multiple quantum well structures[67]. Qualitative behavior may be explained by the following analysis. The PL intensity of each bands can be described by

$$I(T) = I_0 \eta_{\text{int}} \int n dV \tag{3.4}$$

$$\eta_{\text{int}} = \frac{\tau_{nrad}}{\tau_{rad} + \tau_{nrad}} \tag{3.5}$$

where I_0 is the reference intensity, η_{int} is the internal quantum efficiency determined by the ratio of the non-radiative lifetime (τ_{nrad}) and the radiative lifetime (τ_{rad}), n is the electron density at the electron states under analysis, and V is the volume of the active region. Increasing temperature will decrease the non-radiative lifetime of electrons, while the radiative lifetime will remain nearly constant. The internal quantum efficiency will exhibit a corresponding decrease with temperature. An increase in luminescence intensity for the green band with increasing temperature may be explained by a net electron injection into the conduction band from the oxygen states or other shallow nonradiative defects states via the thermal emission when the temperature is in the range of 80K to 120K. And there is a net electron injection into the oxygen states from the conduction band or the non-radiative defect states with the temperature at the region from 120K to 280K. Therefore, temperature dependent PL spectra show presence of coupling between the conduction band and the oxygen states. Overall, the strong radiative emission and absorption properties of these ZnTeO thin films is useful for optical emission or optical conversion devices, as well as an impurity band or intermediate band detector that is currently sought for high-efficiency solar cells.[68,69]

3.4 Summary

Oxygen incorporation is demonstrated in ZnTe samples synthesized by PLD and MBE. The high oxygen partial pressure in the PLD process was found to result largely in the formation of amorphous TeO_x, where thin films exhibiting increasing optical transparency in the visible spectral region. These thin films may find application as

electrically insulating or optically transparent layers for electronic or optical devices based on ZnTe, ZnO, or related semiconductor material systems. The low oxygen content and active oxygen component in the MBE process was found to result in the formation of ZnTe with a defect band or intermediate band 0.4eV-0.7eV below the bandedge. The defect or intermediate band resulting from oxygen incorporation exhibits high radiative efficiency and strong optical absorption properties, and likely be useful for optical emitters/converters or intermediate/defect band solar cells.

Chapter 4

Dynamic Processes of Photo-Carriers

Chapter 3 has demonstrated that incorporation of oxygen results in electronic states in the band gap with high radiative properties. In this chapter, dynamic carrier generation and recombination processes via oxygen states will be analyze experimentally and theoretically.

4.1 Experimental Study

The energy band diagram for ZnTe:O and associated optical transitions are shown in Figure 4.1 (a).

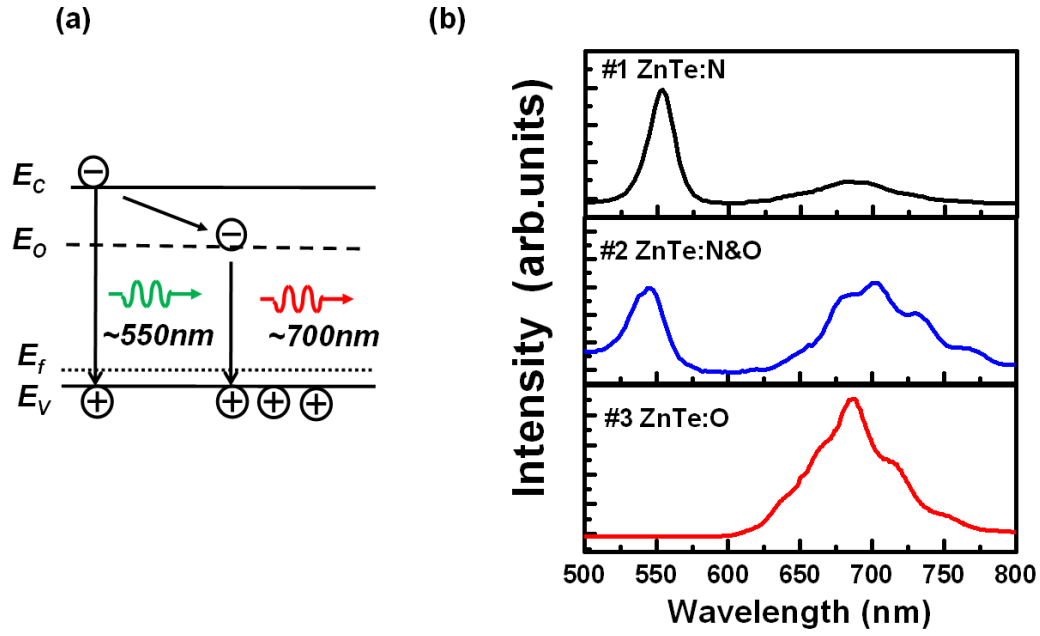

Figure 4.1 (a) Schematic energy band diagram for ZnTe:O and illustration of optical transitions, and (b) room temperature photoluminescence spectra for ZnTe:N, ZnTe:NO and ZnTe:O samples.

The small peaks in the sub-bandgap luminescence in the ZnTe:N&O sample suggest phonon emission and a strong Huang-Rhys factor, the latter occurs when there is a strong coupling of the transition to the lattice (e.g. when an electron leaves a given site the lattice is strongly perturbed) and is often associated with donor-acceptor pair transitions and point defects, rather than a band. In this section, carrier lifetimes in ZnTe:O are measured and applied to a rate equation model to assess generation-recombination processes relevant for IBSC.

ZnTe:O samples were grown on GaAs (100) substrates by molecular beam epitaxy using solid source effusion cells for Zn and Te, and an Electron Cyclotron Resonance (ECR) plasma cell for oxygen and nitrogen incorporation. The nominal thickness of ZnTe samples is 2μm, with further details on material growth reported in the chapter 2. Three samples were studied for comparison with varying oxygen and nitrogen incorporation, as shown in Table 4-1 Doping concentration, TRPL measurement conditions for 550nm and 700nm emissions and measured lifetimes of ZnTe:N, ZnTe:NO and ZnTe:O samples.

	ZnTe:N	ZnTe:NO	ZnTe:O
Hole concentration (cm^{-3})	10^{19}	10^{19}	10^{15}
Oxygen concentration (cm^{3})	--	10^{19}	10^{18}
Lifetime for CB electrons (ps)	<100	<100	<100
Lifetime for O-state electrons	990 ps	160 ps	0.6-4μs

Table 4-1 Doping concentration, TRPL measurement conditions for 550nm and 700nm emissions and measured lifetimes of ZnTe:N, ZnTe:NO and ZnTe:O samples.

Hall-effect measurements indicate that samples doped with nitrogen at a flow rate of 0.8 sccm exhibit p-type conduction with a carrier concentration of 10^{19} cm^{-3}. The sample doped with oxygen only demonstrated p-type conduction with a background concentration of 10^{15} cm^{-3}, attributable to native zinc vacancies[70]. Oxygen incorporates as a substitutional impurity in the tellurium site (O_{Te}) under these growth conditions, resulting in isoelectronic states in ZnTe[71]. The density of O_{Te} state is estimated from the absorption coefficient based on the relation $N_O\ (cm^{-3})=10^{16}\alpha_0\ (cm^{-1})$ (Ref.70), where N_o is the density of O_{Te} state and α_o is the optical absorption coefficient of transition between the valence band and O_{Te} states. The optical absorption coefficient has been characterized

previously on ZnTe:O/sapphire structure in Chapter 3. For oxygen flow rates of 0.08sccm and 0.02sccm, the absorption coefficients are approximately $10^3 cm^{-1}$ and $10^2 cm^{-3}$ resulting in oxygen concentration of 10^{19} cm^{-3} and 10^{18} cm^{-3}, respectively. However, the oxygen doping concentration may be higher than these values because of high possibility of forming oxygen interstitial in ZnTe[72]. Photoluminescence (PL) spectra were measured at room temperature using a He-Cd laser at 325nm, monochrometer, and lock-in detection. Time-resolved photoluminescence (TRPL) measurements were also conducted at room temperature using excitation at 400nm and detection at 550nm and 700nm.

Photoluminescence spectra for the three ZnTe samples with differing oxygen/nitrogen incorporation are shown in Figure 4.1(b). The ZnTe:N sample demonstrates emission predominantly at 550nm (2.25eV), corresponding to the conduction band (CB) to the valence band (VB) transition for ZnTe. The ZnTe:NO sample also shows a conduction to valence band transition at 550nm, as well as a broad peak centered near 700nm corresponding to transitions from oxygen states (intermediate band, IB) to valence band. The ZnTe:O sample doped exclusively with oxygen, however, only the transition from the oxygen states to the VB is observed. The lack of a clear conduction-valence band transition for the ZnTe:O sample is attributed to fast electron relaxation from conduction band to oxygen states, as described in more detail in the following discussion section. Time-resolved photoluminescence data for the three samples are summarized in Table 4-1, with representative scans at 550nm and 700nm shown in Figure 4.2. The emission peaks at 550nm demonstrate fast decay times for both ZnTe:N and ZnTe:NO, with time constants on the order of 100 ps. The time resolution of the TRPL setup is on the order of tens of picoseconds, similar to the time constants for conduction to valence band transitions, suggesting that the carrier lifetime for electrons in the conduction band is <100ps. The emission at 700 nm follows a biexponential function with two time constants, where the PL intensity follows the relation $A_o+A_1exp(-t/\tau_1)+A_2exp(-t/\tau_2)$.

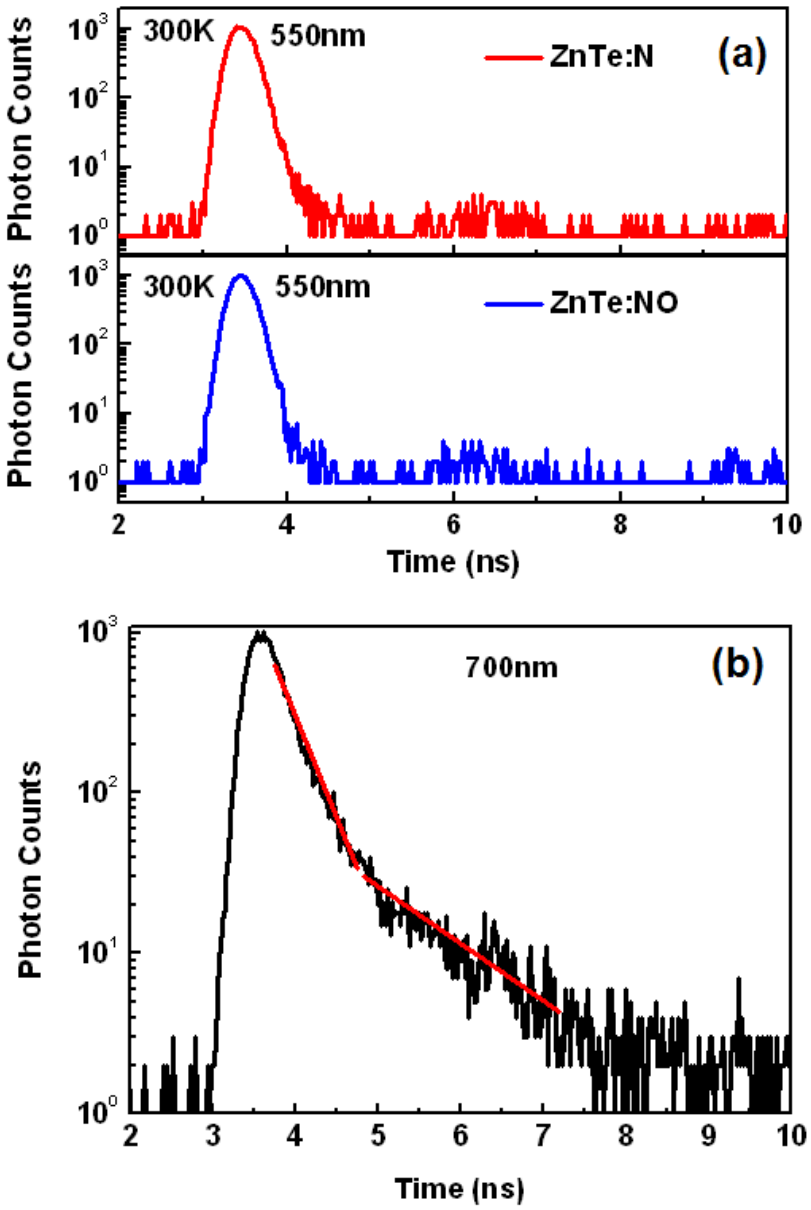

Figure 4.2 Time-resolved photoluminescence spectra of (a) ZnTe:N and ZnTe:NO at 550nm and (b) ZnTe:NO at 700nm.

For the ZnTe:O sample, long decay times exceeding 1μs are observed at low injection levels. In contrast to the ZnTe:N and ZnTe:NO samples, the decay time constant for bulk recombination in the ZnTe:O sample exhibits a dependence on injection level, as illustrated in Figure 4.3(a) with extracted time constants shown in Figure 4.3(b).

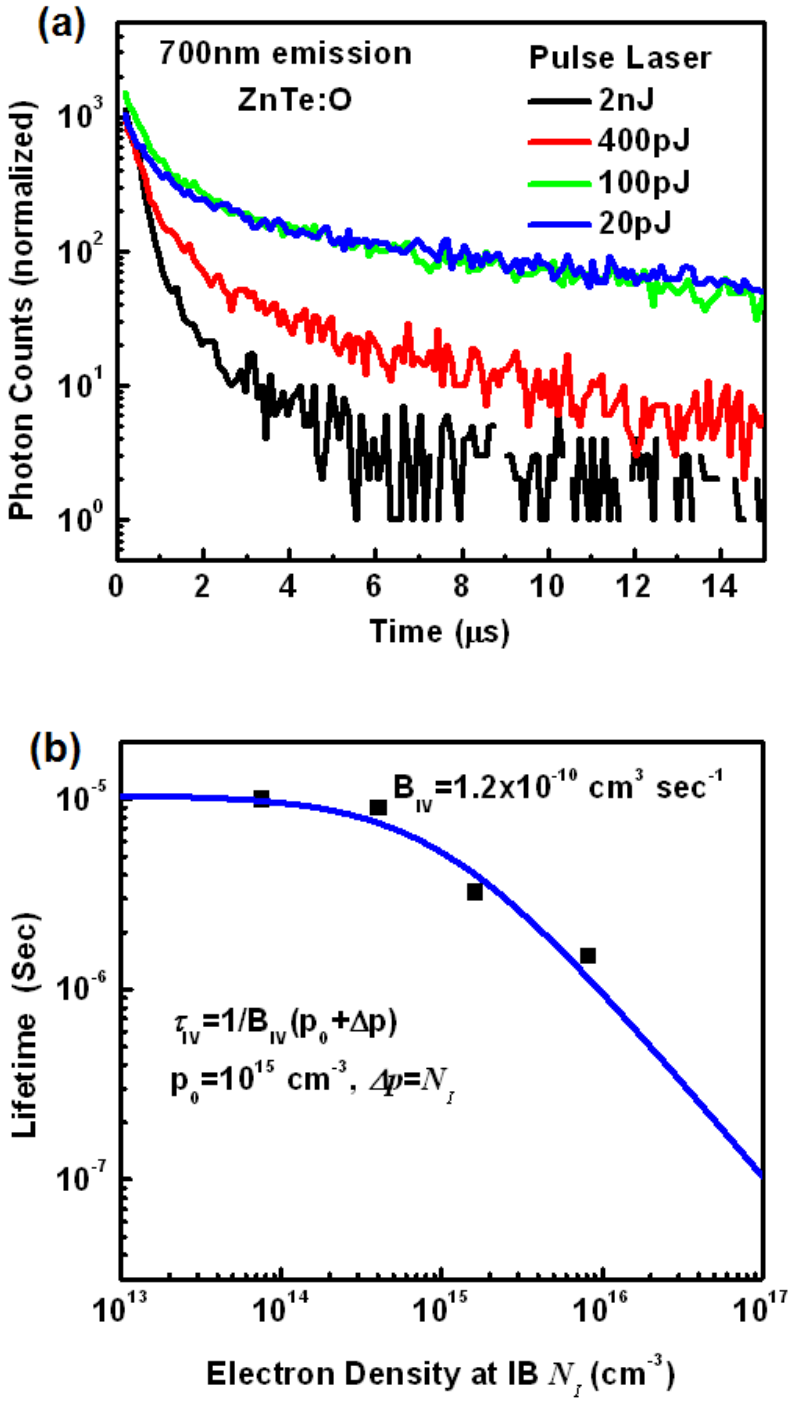

Figure 4.3 Excitation-dependent time-resolved photoluminescence spectra of (a) ZnTe:O at 700nm and (b) resulting carrier lifetime time constants.

4.2 Dynamic Processes without Bias

The variations in PL and TRPL behavior in the ZnTe samples with varying nitrogen and oxygen content may be attributed to carrier concentration and density of oxygen electronic states, as described in the following analysis. The ZnTe:N sample exhibits a short recombination time attribute to the fast radiative recombination rate (B_0p) and the Auger recombination rate (C_0p^2) in ZnTe material with high p type doping, where the radiative recombination coefficient (B_0) is estimated to be 7.1×10^{-10} cm^3/sec (Ref.[73]), and the Auger recombination coefficient (C_0) is typically about 10^{-29} cm^6/sec, (Ref.[74])] The incorporation of oxygen in the ZnTe:NO sample provides an additional recombination path for photo-generated carriers, resulting in the observed peak centered at 700nm. The electronic states corresponding to oxygen provide a means to trap electrons from the CB, where the resulting strong emission from the oxygen states demonstrates a significantly longer carrier lifetime due to the nature of the localized oxygen defect. The CB to VB transition disappears for the ZnTe:O sample with a high concentration of oxygen states and no p-type doping, while the transition corresponding to oxygen states increases. This behavior may be explained by fast capture into the high density of oxygen states, in conjunction with reduced CB to VB recombination rates due to reduced hole concentration. The longer carrier lifetime associated with oxygen states in the ZnTe:O sample may also be attributed to reduced hole concentration in comparison to the ZnTe:N and ZnTe:NO samples. The carrier populations in the CB, VB, and IB can be expressed by the following rate equations (in the absence of external generation)

$$\frac{dn}{dt} = -\frac{n}{\tau_{CV}} - \frac{n}{\tau_{CI}} + \frac{N_I}{\tau_e}, \tag{4.1}$$

$$\frac{dN_I}{dt} = \frac{n}{\tau_{CI}} - \frac{N_I}{\tau_{IV}} - \frac{N_I}{\tau_e} \tag{4.2}$$

$$\frac{dp}{dt} = \frac{dn}{dt} + \frac{dN_I}{dt}. \tag{4.3}$$

where n, p, and N_I are the electron density in the CB, hole density in the VB, and electron concentration in the oxygen states, respectively. The electrons in the CB can transit to the VB, empty states in the IB, or by SRH process. Electrons can also be thermally injected into the VB from the CB. The population of electrons in the IB is determined by injection

from the IB, and emission out to the VB and CB. Finally, the change of hole population is equal to that of electron population. For the simplest case, the initial values of *n* and *p* are equal to injection carrier density, and the initial value of N_I is zero. Radiative recombination is assumed to be the dominant process for this analysis, with the exception of relaxation of carriers from CB to oxygen states and thermal emission of electrons from the IB to the CB. The carrier lifetimes for various transitions are given by the variables τ_{CV} (CB to VB), τ_{IV} (IB to VB), τ_{CI} (CB to IB) and τ_e (IB to CB) [Ref.75] can be expressed by

$$\tau_{CV} = \frac{1}{B_0(p_0 + n_0 + \Delta p)} \cong \frac{1}{B_0 p} \tag{4.4}$$

$$\tau_{IV} = \frac{1}{B_1(p_0 + \Delta p)} \cong \frac{1}{B_1 p} \tag{4.5}$$

$$\tau_{CI} = \frac{1}{v_{th}\sigma_n(N_o - N_I)} \tag{4.6}$$

$$\tau_e = \frac{\exp((E_c - E_I)/kT)}{v_{th}\sigma_n N_c} \tag{4.7}$$

where B_0 is the radiative recombination coefficient for CB to VB transition in ZnTe, with a value of 7.1×10^{-10} cm^3/sec[76]. B_1 is the radiative recombination coefficient extracted from the power dependent TPRL shown in Figure 4.3(b). The electron and hole concentrations p_0 and n_0 are values under thermal equilibrium, where Δp is the injected hole concentration. The equilibrium electron concentration is neglected in the lifetime expressions due to p-type conductivity in all samples. The value of τ_{CI} is determined using the thermal velocity of electrons at room temperature v_{th} $=2.6\times10^7$cm/s, concentration of oxygen atoms N_O inferred from absorption measurements, and assuming a capture cross section for electrons of σ_n $=2\times10^{-14}cm^2$(Ref.70). As shown in Equation (4.7), τ_e is about 2×10^{-3} s from the Equation (4.7), where E_I is the energy level of the IB, *k* is Boltzmann constant, T is absolute temperature, and N_c is the effective density of state at the CB. Here the oxygen states lies in at least 0.5ev below the bottom of the CB, τ_e is much smaller than τ_{CI} unless the oxygen states in nearly full occupation. The injected carrier density may be related to the TRPL excitation conditions assuming the the

absorption coefficient for ZnTe at 3.1eV of approximately $\alpha=1.5\times10^{4}cm^{-1}$ (Ref. 77) and a uniform carrier distribution in the ZnTe layer.

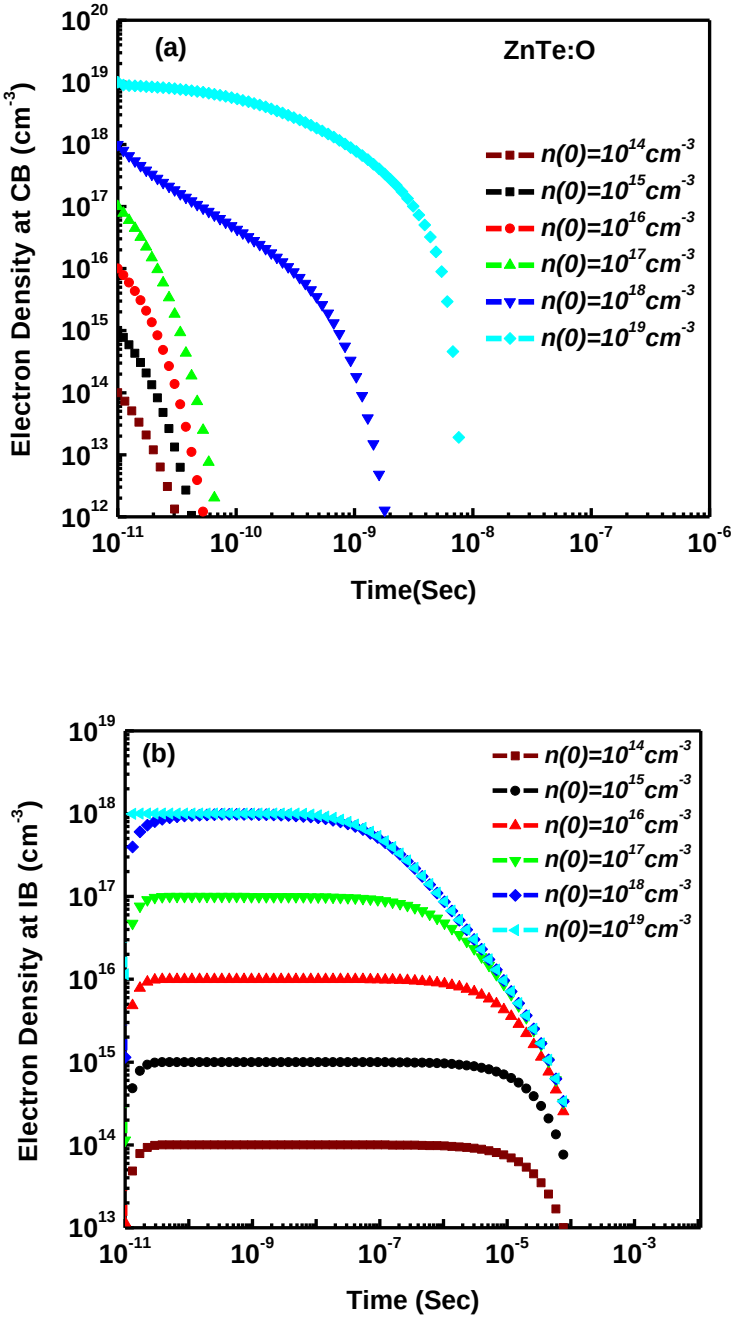

Figure 4.4 Time resolved electron population at (a) the CB (b) the IB.

The calculated evolution of the electron population at the CB and the IB under varying excitation intensity is shown in Figure 4.4 (a) and (b) respectively. The electron

population at the CB decreases at approximately the same rate when *n(0)* is at least one order of magnitude lower than $10^{18}cm^{-3}$. There is a clear saturation in the filling of IB states, which occurs at time scale less than 50ps as shown in Figure 4.4(b). For full occupation of IB states, electron transitions from The CB to IB are prohibited. The electron lifetime at the CB is significantly increased as a result of IB occupation, as shown in Figure 4.4 (a).

The evolution of the hole population is shown in Figure 4.5. When the injection density is less than the doping level, $10^{15}\ cm^{-3}$, the hole population is nearly fixed. With increasing the injection level, the evolution curves match closely with those of electron in the IB until the injection level is over the density of IB, $10^{18}cm^{-3}$, where the recombination from the CB to the VB is dominant at the beginning.

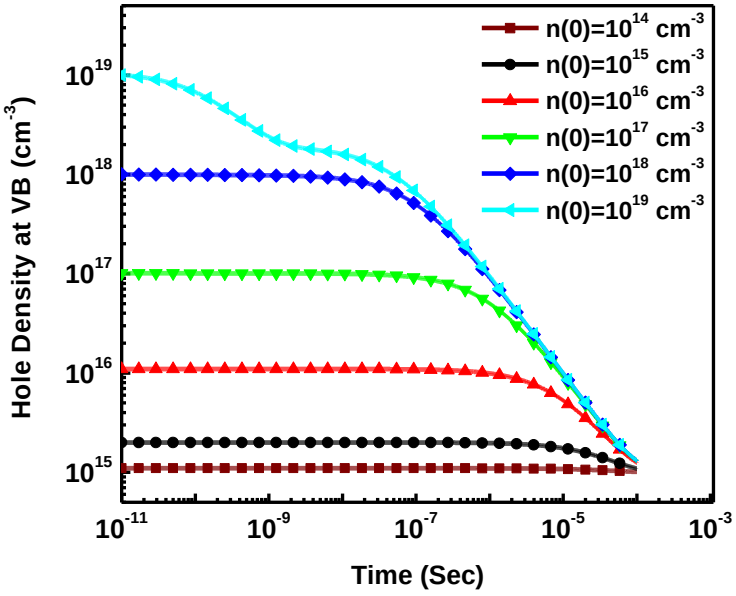

Figure 4.5 Time resolved hole population at the VB.

The simulated decay time constants for electrons in the IB under varying excitation are shown in Figure 4.6 , and are in good agreement with TRPL measurements. The effective carrier lifetime for electrons in the CB based on simulations of the above rate equations is also shown in Figure 4.6 for varying injection density, along with the lifetime of electrons in the IB. Based on these simulations, the effective carrier lifetime for CB electrons show the expected increase with increasing excitation density due to an

increase in electron population in IB states. The carrier lifetime for IB electrons also show a corresponding decrease with injection density, though is still orders of magnitude higher than the lifetime for CB electrons. The dependence of lifetime for CB and IB electrons may be divided into three regions according to injection density relative to the background hole concentration (10^{15} cm^{-3}) and IB state density (10^{18} cm^{-3}). The effective lifetime of CB electrons may be extended to approximately 1ns when the IB states are fully occupied, which would greatly improve the ability to extract carriers generated from a multi-photon process in an IBSC device.

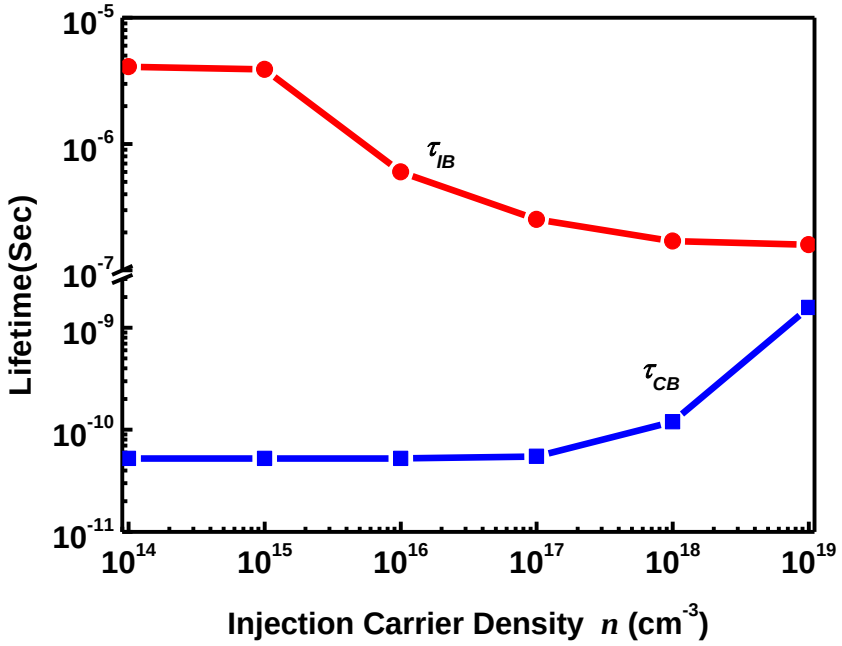

Figure 4.6 Simulated effective carrier lifetime for electrons at the CB and IB for varying injection.

In reality, electrons may also be promoted to the IB from deep within the VB. Therefore, the initial values of the n, N_I, p can be expressed as following: $n=p_0N_c/(N_c+N_T)$, $N_I=p_0 N_T/(N_c+N_T)$, $p=p_0$, where p_0 is the injected photon number, N_c is the effective density of state at the CB, and N_T is the density of oxygen states. The overall carrier population evolution of these initial conditions is nearly the same as the more simplified model, with the exception of high IB occupation for high injection levels.

4.3 Dynamic Processes with Applied Electric Field

The application of an electrical field (as shown in Figure 4.7) results in fast extraction of electrons in the CB and holes in the VB. Consequently, the probability for electrons in the oxygen states to recombine with holes in the VB is reduced significantly. Electron lifetime in the oxygen states may be determined by the emission process.

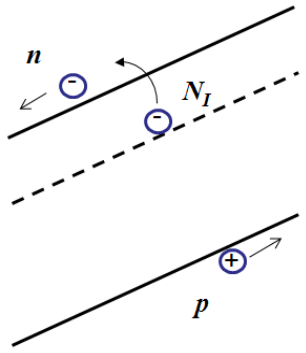

Figure 4.7 The band diagram of ZnTeO under an external electrical field.

The carrier population in the CB, IB and VB under bias can be described by the following rate equations.

$$\frac{dn}{dt} = -\frac{n}{\tau_{CV}} - \frac{n}{\tau_{CI}} - \frac{n}{\tau_{dr1}} + \frac{N_I}{\tau_e}, \tag{4.8}$$

$$\frac{dN_I}{dt} = \frac{n}{\tau_{CI}} - \frac{N_I}{\tau_{IV}} - \frac{N_I}{\tau_e}, \tag{4.9}$$

$$\frac{dp}{dt} = -\frac{p}{\tau_{dr2}} - \frac{p}{\tau_{CV}} - \frac{p}{\tau_{IV}}. \tag{4.10}$$

where τ_{dr1} and τ_{dr2} are the drift times for electrons and holes respectively. Drift time is defined as $\tau_{dr} = {}^{D}/_{\mu E}$, where D is the thickness of the ZnTe:O film, assumed to 5μm in our simulation, E is the bias electrical field, assumed to 10^4V/cm, μ is mobility, assumed to 100 cm^2/Vs for electrons and 50 cm^2/Vs for holes. Finally, the maximum drift time for electrons and holes in the film are 0.5ns and 1ns, respectively. Other parameters have been defined in the Section 4.2. The initial values of the n, N_I, p can be expressed by $n=p_0N_c/(N_c+N_T)$, $N_I=p_0 N_T/(N_c+N_T)$, and $p=p_0$ as defined in the Section 4.2.

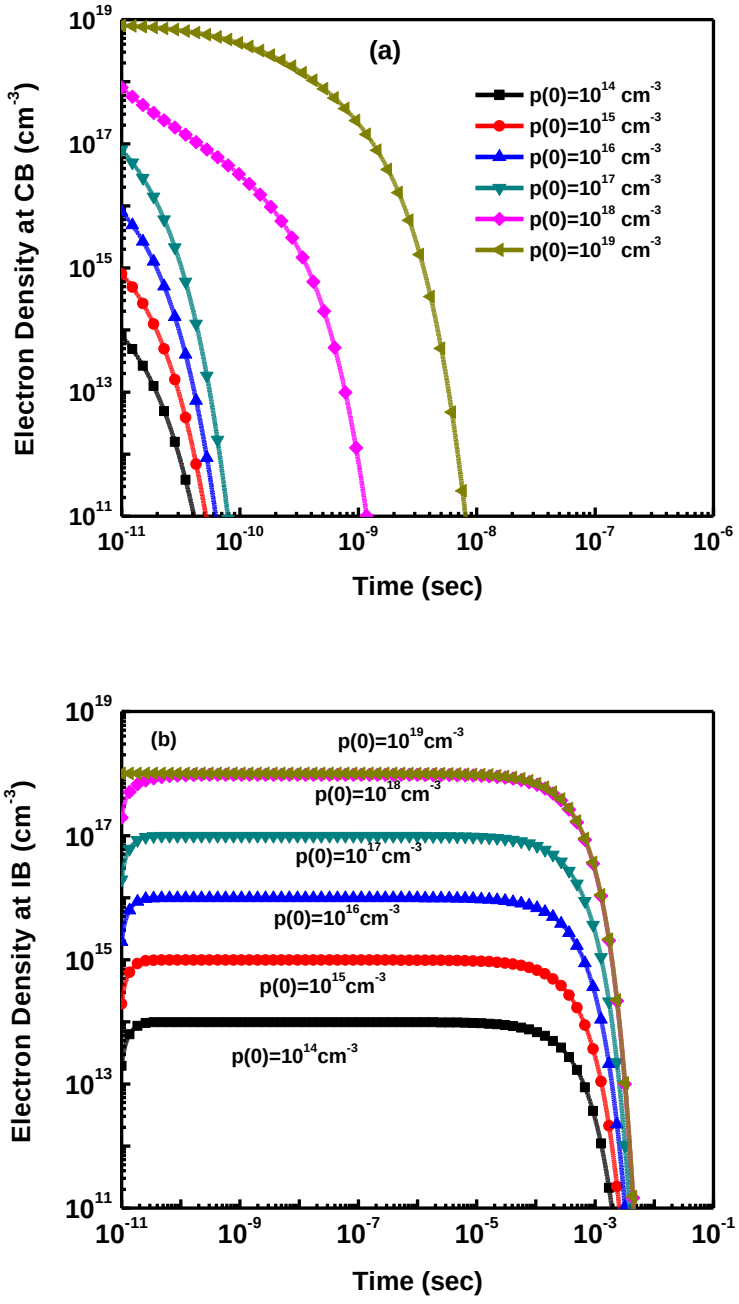

Figure 4.8 Time resolved electron population under electrical field bias at (a) the CB (b) the IB.

The time evolution of the electron population in the CB is illustrated in Figure 4.8 (a), where behavior is very similar to that without electrical field bias in the near the initial carrier injection to a time of approximately 10^{-7}sec. Because the effective time (τ_e) of thermal emission from the IB to the CB is more than 0.1 ms, which is much longer

than the drift time and the recombination time from the CB to the IB and from the CB to the VB, the effect of thermal emission is negligible.

In contrast, a majority of holes are extracted within 1ns as shown in Figure 4.9 Therefore, electrons will be trapped in the IB until the thermal emission is significant (after 10^{-5}s) as shown in Figure 4.8 (b). The carrier dynamics become more complex at this time scale, where the electron population in the CB and the IB are tightly coupled. After electrons emit from the IB to CB, fraction of them will drift out directly, while the remaining carriers will relax back to the IB. The electrons will continue to cycle untilelectrons from the IB are extracted. Therefore, the effective lifetime of electrons at the IB may be larger than the thermal emission time. Long electron lifetime in the IB is beneficial to achieving full or half full occupation in the IB with low photon flux.

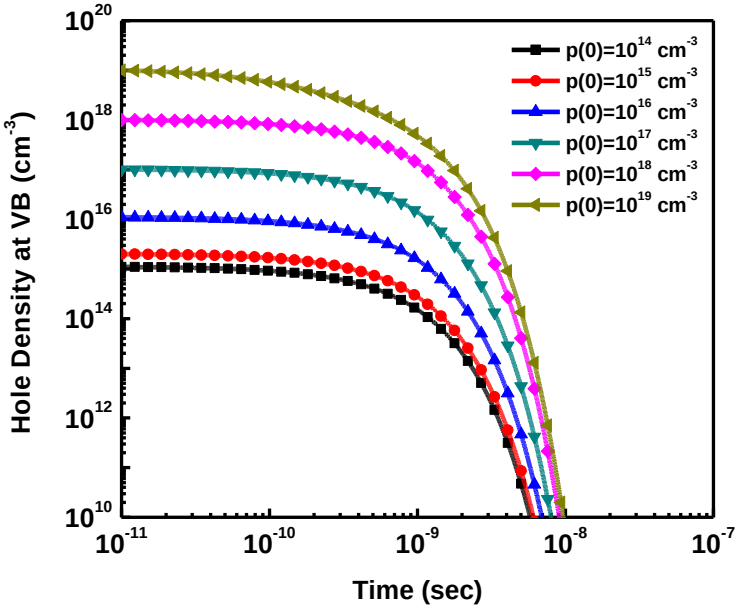

Figure 4.9 Time resolved hole population at the VB under electrical field bias.

4.4 Summary

Carrier generation and recombination processes are studied for ZnTeO thin films grown by molecular beam epitaxy. Long carrier lifetime (>1μs) is measured for electrons in oxygen states in ZnTe, where lifetime shows an inverse proportionality with hole density. Shorter carrier lifetime is measured for IB states in p-doped ZnTe:NO and

ZnTe:N material where hole population is significantly larger. Short lifetime (<100ps) is observed for electrons in the CB, and is attributed to the fast relaxation of carriers from the CB to IB. The radiative recombination coefficient for optical transitions from oxygen states to the valence band are extracted to be 1.2×10^{-10} cm^3 sec^{-1} based on the excitation dependence of decay time constants.

Rate equation analysis suggests that the effective lifetime of CB electrons also exhibits a dependence on injected carriers, where increase in lifetime is possible when injection is on the order of the IB state density. High injection conditions, such as would be present in solar concentrator cells, would serve to enhance the carrier lifetime for CB electrons and resulting conversion efficiency for intermediate band solar cells based on these materials.

Rate equation analysis also suggests that the effective lifetime of IB electrons can be extended to thermal emission time which is much longer than the radiative recombination time by applying an electrical field bias. And it will increase further with the electron cycling effect. Long electron lifetime in the IB is beneficial to achieving full or half full occupation in the IB with low photon flux, which may provide more space to reduce the cost of optics for high concentrate solar system, which will be discussed in the next chapter.

Chapter 5

Design of ZnTeO Based IBSC

In this chapter, a device model for ZnTeO based IBSC is developed to optimize the device parameters and operation conditions for achieving maximum conversion efficiency. Parasitic factors in a ZnTe diode are also discussed.

5.1 Device Model

The theoretical model for IBSC operating under ideal conditions has predicted that the maximum conversion efficiency is 63.1% with the following assumptions: 1) nonradiative transitions between any two of the three bands are forbidden; 2) carrier mobility is infinite; 3) no carrier can be extracted from the impurity band; 4) the cell is thick enough to assure full absorption of the photons; 5) radiative emission loss at the cell's backside is zero; 6) for every range of energies only one of the three absorption lengths is important; 7) the cell illumination is isotropic[78]. However, the operation conditions for real devices are far from the ideal cases. Therefore, a theoretical model based on semiconductor device physics without holding the above assumptions needs to be developed in order to guide the device design for maximum conversion efficiency.

5.1.1 Carrier Recombination and Transportation Model

The Carrier Recombination and Transportation (CRT) model based on p-i-n device structure with intermediate band states located in the intrinsic region has been developed to estimate the overall conversion efficiency depending on the device parameters such as optical absorption coefficient, minority carrier lifetime, carrier transportation, density of intermediate band, energy position of intermediate band and so on[79]. The model concludes that the conversion efficiency degrades for short minority carrier lifetime or

long absorption length relative to minority carrier drift length as shown in Figure 5.1 and Figure 5.2 respectively.

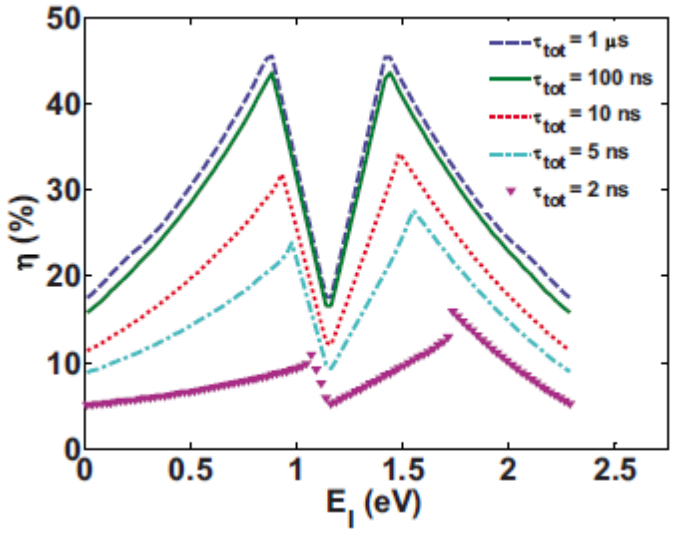

Figure 5.1 Efficiency vs IB energy level (E_I) for varying recombination lifetime values with $\alpha_{VC}=10^4 cm^{-1}$, E_G=2.3eV, $\mu_n=\mu_p=100 cm^2/Vs$, W=10μm, and $\alpha_{IC0}=\alpha_{VI0}=10^4 cm^{-1}$. (Ref. 79: *A. Lin, W. Wang, J. Phillips, J. Appl. Phys.105, 064512 (2009)*)

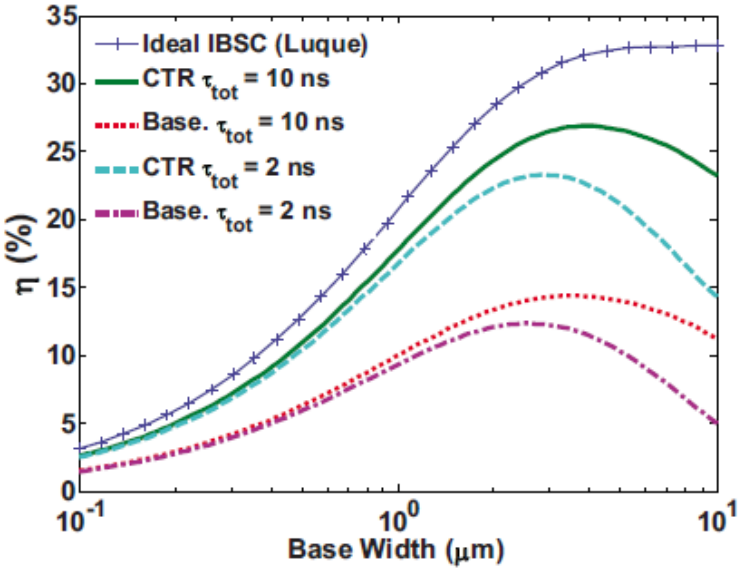

Figure 5.2 Efficiency vs base width comparing the CTR model to an ideal IBSC solar cell without an IB. Material and device parameters are $\alpha_{VC}=10^4 cm^{-1}$, E_G=2.3eV, E_I=1.8eV, $\mu_n=\mu_p=100\ cm^2/Vs$, and $\alpha_{IC0}=\alpha_{VI0}=10^4 cm^{-1}$. (Ref. 79: *A. Lin, W. Wang, J. Phillips, J. Appl. Phys.105, 064512 (2009)*)

However, the CRT model may be not precise enough to guide the design of IBSC based on without including the following factors:

(1) The electrical field redistribution in the base region (or intrinsic region) because of electron occupation in the intermediate band whose density may vary from 10^{15}-10^{20} cm^{-3}. The redistributed the electrical field and potential profile in the device will significantly reform the base width and carrier transportation[80].

(2) The minority carrier lifetime extremely depends on the electron occupation of the intermediate band.

5.1.2 Update of the CRT Model

Because electron mobility is usually faster than hole mobility for most of semiconductor materials, an n^+-p asymmetric junction is most commonly used for a solar cell device. The device structure of a ZnTeO based IBSC is defined in Figure 5.3, where the n^+-layer is an electron emitter and the p layer incorporating oxygen states as a main absorber. Photons are injected from the n^+-layer side. L_p is the effective hole diffusion length at the n layer, x_n is the depletion width in the n layer, x_p is the depletion width at the p layer, and L_n is the effective electron diffusion length at the p layer. The static electrical field and potential is defined by Poisson's equation.

$$\frac{d^2\phi}{dx^2} = -\frac{\rho}{\varepsilon} \tag{5.1}$$

where ϕ is the electrical potential, ε is the dielectric constant of ZnTe, and ρ is the charge density defined in the following equations.

$$\rho = qN_D \ (-x_n \leq x < 0) \tag{5.2}$$

$$\rho = -q(N_I + N_A) \ (0 < x \leq x_p) \tag{5.3}$$

where q is electronic charge unit, N_D is the net donor density at the n region, N_A is the net acceptor density at the p region, and N_I is the electron density at the IB.

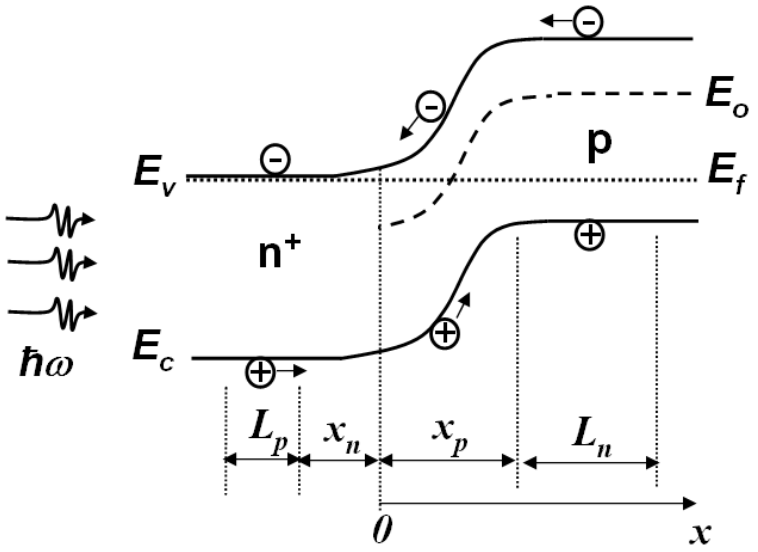

Figure 5.3 Device schematic of n^+-p ZnTe asymmetric junction with oxygen intermediate band in p- side.

Furthermore, the depletion width of the junction is determined by the following equation assuming all external voltage is applied on the depletion region.

$$W = \left\{ \frac{2\varepsilon(V_{bi} - V_a)}{q} \left[\frac{1}{N_A + N_I} + \frac{1}{N_D} \right] \right\}^{1/2} \tag{5.4}$$

where V_{bi} is the self-built potential of n^+-p ZnTe homojunction, and V_a is the apply forward voltage. Obviously, the depletion region (W) will shrink because of electron occupation in the IB, whose value can be determined from the following current continuity equations at steady state:

$$\frac{dn}{dt} = -R_{CV} - \frac{n}{\tau_{CI}} + \frac{N_I}{\tau_e} + G_{IC} + G_{VC} + \frac{1}{q}\frac{dJ_n}{dx} = 0 \tag{5.5}$$

$$\frac{dN_I}{dt} = \frac{n}{\tau_{CI}} - R_{IV} - \frac{N_I}{\tau_e} - G_{IC} + G_{VI} = 0 \tag{5.6}$$

$$\frac{dp}{dt} = -R_{CV} - R_{IV} + G_{VI} + G_{VC} - \frac{1}{q}\frac{dJ_p}{dx} = 0. \tag{5.7}$$

The recombination lifetime from the CB to the IB (τ_{CI}) and the thermal emission lifetime from the IB to the CB (τ_e) have been defined in the Chapter 4. The radiative recombination rate from the CB to the VB (R_{CV}) and from the IB to the VB (R_{IV}) can be

defined by $R_{CV}=B_1np$, $R_{CV}=B_2N_1 p$, where B_1 and B_2 are the radiative recombination coefficients also presented in the Chapter 4.

The current densities J_n and J_p are defined by the carrier transport equations:

$$J_n = q\mu_n nE + qD_n \frac{dn}{dx} \tag{5.8}$$

$$J_p = q\mu_p pE - qD_p \frac{dp}{dx} \tag{5.9}$$

where D_n and D_p are the diffusion coefficient for electrons and holes.

The photon carrier generation rates: G_{IC}, G_{VC}, and G_{VI} are defined in the below equations.

$$G_{CV}(x) = (1-R)\eta\phi_{CV}\alpha_{CV}\exp(-\alpha_{CV}x) \tag{5.10}$$

$$G_{IC}(x) = (1-R)\eta\phi_{IC}\alpha_{IC}\exp(-\alpha_{IC}x) \tag{5.11}$$

$$G_{VI}(x) = (1-R)\eta\phi_{VI}\alpha_{VI}\exp(-\alpha_{VI}x) \tag{5.12}$$

The reflection (R) at air/semiconductor interface is assumed to be zero, and internal quantum efficiency η to be unit for ideal situation. In these equations, ϕ_{CV} ϕ_{VI} and ϕ_{IC} are the photon fluxes whose photon energy $E_{ph}\geq E_g$, $E_g\geq E_{ph}\geq Eo$ and $E_o\geq E_{ph}\geq E_g$-Eo respectively in the AM1.5 solar spectrum. Based on the room temperature photoluminescence results shown in Chapter 3, the oxygen related IB covers from 1.6eV to 1.9eV above the VB. The values of ϕ_{CV} ϕ_{VI}, ϕ_{IV} and the corresponded maximum photon current densities are listed in the Table 5-1.

	Flux Intensity (No. cm^{-2} sec^{-1})	Max. J_{ph} ($mA.cm^{-2}$)
$\phi_{AM1.5}$	4.00×10^{17}	63.9
ϕ_{CV} ($E_{ph}\geq$2.29eV)	4.6×10^{16}	7.4
ϕ_{VI} (2.29eV>$E_{ph}\geq$1.6eV)	8.6×10^{16}	13.8
ϕ_{IC} (1.6eV>$E_{ph}\geq$0.4eV)	2.48×10^{17}	38.7

Table 5-1 Photon fluxes, maximum photo current densities for transition from the VB to the CB, from the VB to the IB, from the IB to the CB under AM1.5.

α_{CV} is the absorption coefficient of ZnTe above the bang gap. The absorption coefficients from the VB to the IB (α_{VI}) and from the IB to the CB are defined in the following equations:

$$\alpha_{IC} = \sigma_{opt} N_I \tag{5.13}$$

$$\alpha_{VI} = \sigma_{opt} (N_o - N_I) \tag{5.14}$$

where σ_{opt} is the optical cross section of the IB, also defined in the Chapter 4, and N_o is the oxygen related IB density.

The overall photo carrier generation rates for different transitions are given in the following:

$$S_{VC} = \int_{-x_n - L_p}^{x_p + L_n} G_{VC}(x) dx \tag{5.15}$$

$$S_{IC} = \int_{0}^{x_p + L_n} G_{IC}(x) dx \tag{5.16}$$

$$S_{VI} = \int_{0}^{x_p + L_n} G_{VI}(x) dx \tag{5.17}$$

.

Since the oxygen related IB only locates in the p region, the transitions via IB only happen there.

Finally, the J-V curves can be solved numerically from the current continuity equations with the boundary conditions given by the applied voltage. The overall conversion efficiency is determined by the equation below.

$$\eta_{con} = \frac{J_{SC} \times V_{OC} \times FF}{XP_{AM1.5}} \tag{5.18}$$

where J_{sc} is the short circuit current density, V_{oc} is the open circuit voltage, FF is the fill factor in the J-V curve, X is the concentrated time of incident sun light, and $P_{AM1.5}$ is the total power of AM1.5 spectrum. Ideally, J_{sc} is equal to the photo current J_{ph}, which consists of three parts: J_{ph_1} generated in the hole diffusion length of the n side, J_{ph_2} generated in the electron diffusion length of the p side, and J_{ph_3} generated in the depletion region.

5.1.3 Effect of Electron Occupation

Electron occupation in the IB is the most critical parameter to determine working conditions of ZnTeO based IBSC, which is solved from self consistence of the current continuity equations under steady state.

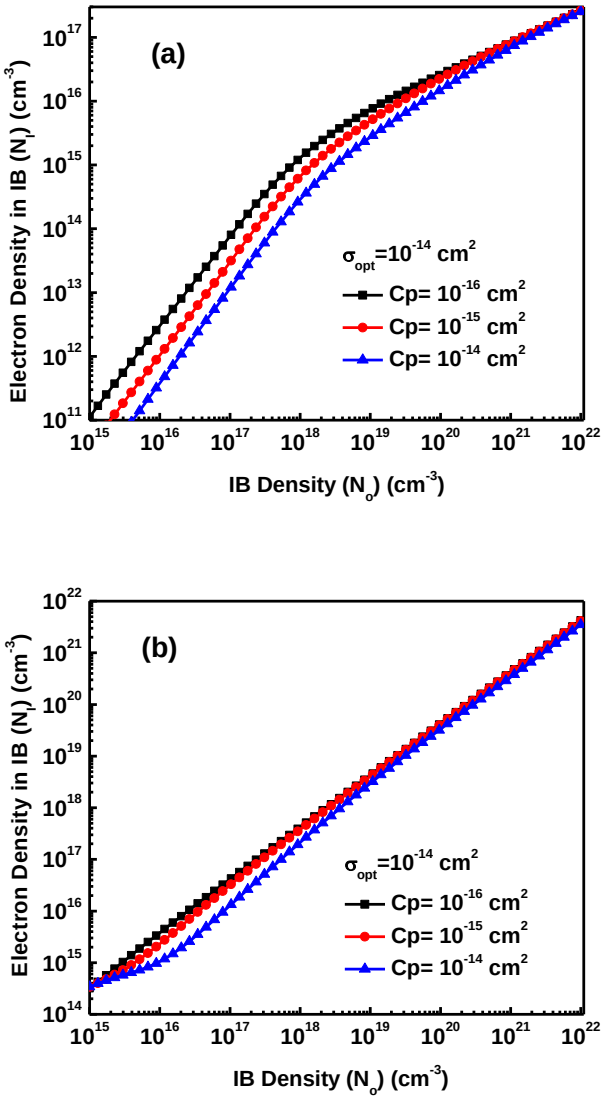

Figure 5.4 Electron occupation vs IB density in (a) the diffusion region (b) the depletion region of a n^+-p ZnTeO diode under AM1.5 illumination.

In the depletion region, both holes and electrons either generated from the doping or photon excitation are swiped out by the self-built electrical field. However, the hole concentration in the p side diffusion region is still maintained at doping level. Therefore,

the electron lifetime of the IB at the depletion region is much larger than that in the p side diffusion region. Under AM1.5 illumination, the IB occupation in the diffusion region is less than 0.01%, nearly empty, but the IB in the depletion region is nearly half filled as shown in Figure 5.4.

The depletion width, the electron diffusion length, the absorption coefficients, and photon carrier rates are all dependent on the electron occupation in the IB shown in the following figures.

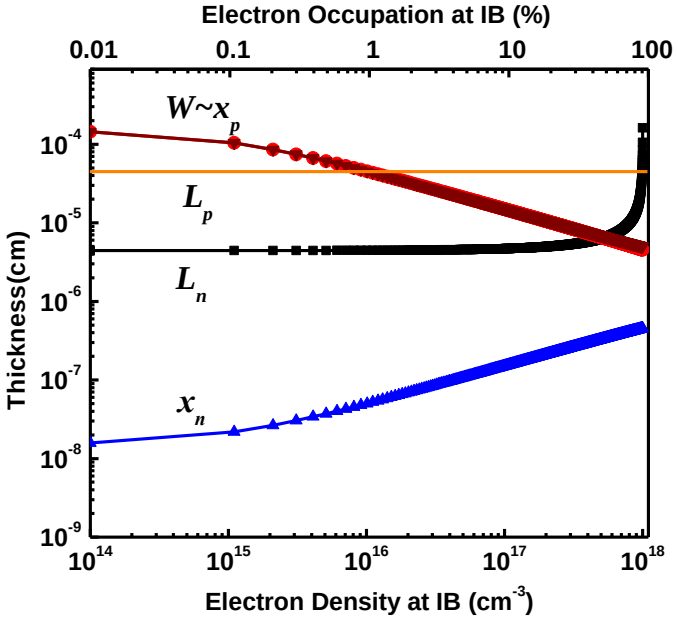

Figure 5.5 Critical scales as a function of electron density and occupation in IB in ZnTe homo-junction with zero voltage bias, IB density No=10^{18}cm^{-3}, N_A=10^{15}cm^{-3}, N_D=10^{19}cm^{-3}, E_G=2.29eV, E_O=1.75eV, μ_n=μ_p=100 cm^2/Vs.

In the n$^+$-p asymmetric junction, the total depletion width (W) is almost equal to the depletion width in the p region (x_p). At low level of electron occupation in the IB, x_p is more than 1μm, much larger than other scale parameters (L_p, L_n and x_n), indicating the photon current mainly generates in that region. With increasing the electron occupation, the total depletion region shrinks, and decreases to around 50nm at full electron occupation as predicted by the equation (5.4), but the electron diffusion length (L_n) expands from 50nm to more than 1 μm because of increase of electron lifetime. However, the IB should be nearly 50% filled in order to balance the sub-band absorption. In this case, both x_p and L_n will be around 100nm, which are too thin to capture all sub-band

photons if absorption coefficients (α_{VI}, α_{IC}) are around 5000 cm^{-1}, as shown in Figure 5.6. The carrier generation rates (S_{VI}, S_{IC}) of sub-band absorption shown in Figure 5.7 indicate that the occupation is about 30% with S_{VI} equal to S_{IC} under AM1.5.

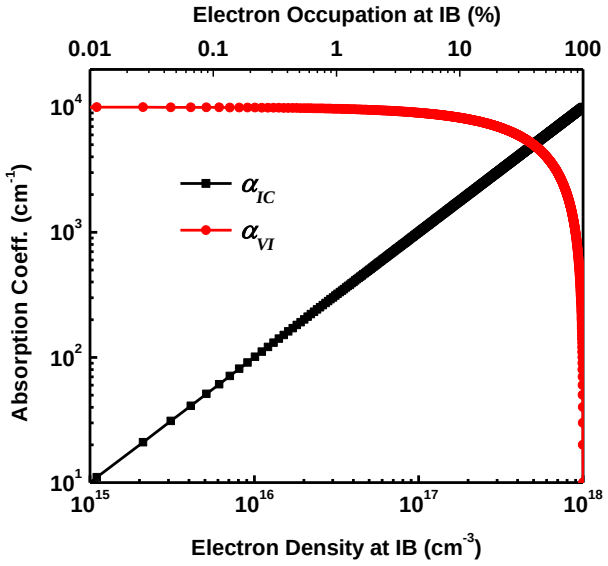

Figure 5.6 Absorption coefficients (α_{VI}, α_{IC}) vs electron density and occupation in IB in ZnTe homo-junction with zero voltage bias, IB density No=$10^{18}cm^{-3}$, $N_A=10^{15}cm^{-3}$, $N_D=10^{19}cm^{-3}$, E_G=2.29eV, E_O=1.75eV, optical cross section $\sigma_{opt}=10^{-14}cm^2$.

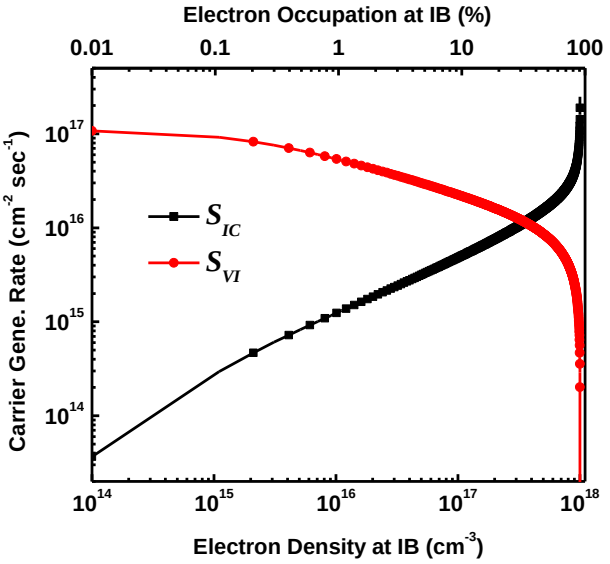

Figure 5.7 Carrier generation rates (S_{VI}, S_{IC}) vs electron density and occupation in IB in ZnTe homo-junction with zero voltage bias, IB density No=$10^{18}cm^{-3}$, $N_A=10^{15}cm^{-3}$, $N_D=10^{19}cm^{-3}$, E_G=2.29eV, E_O=1.75eV, optical cross section $\sigma_{opt}=10^{-14}cm^2$, under AM1.5.

5.2 Optimization of Device Parameters

Based on the updated CRT model, the impacts of material parameters, device doping profile and operation conditions on the overall conversion efficiency are reevaluated to give the clues of device design.

5.2.1 Intermediate band density (No)

The optimal value of the IB density is estimated first since it is the primary parameter to determine the IBSC's performance. The J-V curves of ZnTe based solar cells with and without an IB are illustrated in the Figure 5.8. The short circuit current (J_{sc}) increases because of additional absorption from the IB, but the open circuit voltage (V_{oc}) decreases because electron lifetime degrades with existence of unoccupied states in the IB. The Fill Factor (FF) also degrades because of the following mechanics. The percentage of photo current generated in the depletion region is much higher for a ZnTeO solar cell than that for a ZnTe solar cell. Therefore, more significant decrease of photon current in a ZnTeO cell when the depletion region is shrunk by applied forward voltage. However, the conversion efficiency improvement can be achieved once the enhancement of J_{sc} is significant enough to overcome the scarification of V_{oc} and FF.

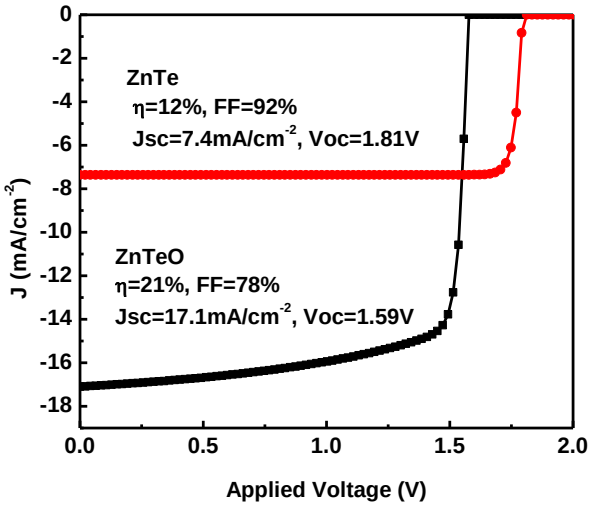

Figure 5.8 J-V curves for n^+-p ZnTe homejunction with and without the oxygen states in the p region , capture cros-section $Cp=10^{-14}cm^2$, optical cross-section $\sigma_{opt}=10^{-13}cm^2$, $No=10^{20}$ cm^{-3}, $N_A=10^{15}cm^{-3}$, $N_D=10^{19}cm^{-3}$, E_G=2.29eV, E_O=1.75eV, $\mu_n=\mu_p=100$ cm^2/Vs, underAM1.5.

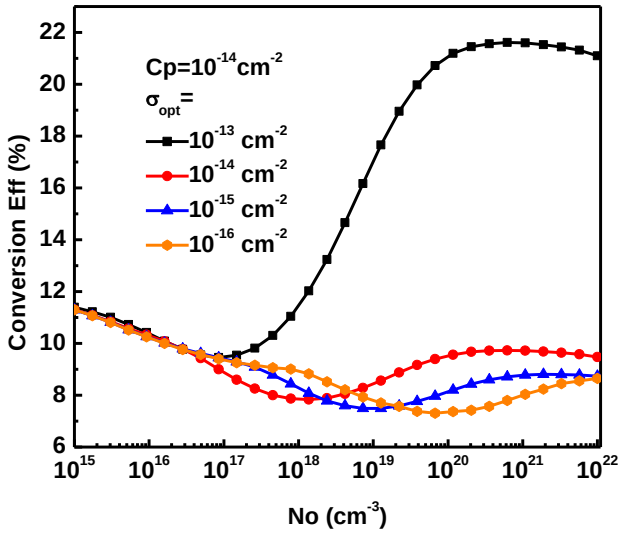

Figure 5.9 Conversion efficiency of a ZnTeO IBSC in n^+-p structure with the IB only in p region, vs the IB density with varying optical cross-section σ_{opt} with the capture cross-section $Cp=10^{-14}cm^2$, $N_A=10^{15}cm^{-3}$, $N_D=10^{19}cm^{-3}$, E_G=2.29eV, E_O=1.75eV, $\mu_n=\mu_p=100\ cm^2/Vs$, under AM1.5.

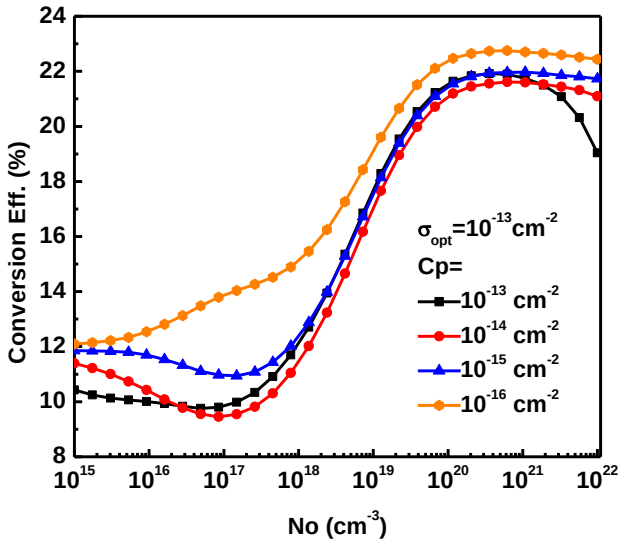

Figure 5.10 Conversion efficiency of a ZnTeO IBSC in n^+-p structure with the IB only in p region, vs the IB density with varying capture cross-section Cp with the optical cross-section $\sigma_{opt}=10^{-13}cm^2$, $N_A=10^{15}cm^{-3}$, $N_D=10^{19}cm^{-3}$, E_G=2.29eV, E_O=1.75eV, $\mu_n=\mu_p=100\ cm^2/Vs$, underAM1.5.

The optimal value of the IB density results from not only the balance of carrier recombination and generation but also the tradeoff between shrink of the depletion width and increase of absorption. As shown in Figure 5.9 and Figure 5.10, the efficiency is

extremely dependent on the optical cross section (σ_{opt}) of oxygen states, but nearly independent on the capture cross-section (Cp). It is because the IB occupations in both the depletion region and the diffusion region are almost fixed given a constant illumination as illustrated in Figure 5.4. Therefore, ratio of carrier recombination to generation doesn't change. When the σ_{opt} is about 10^{-13} cm^2, the optimal IB density is in the range of 10^{20}-$10^{21}cm^{-3}$, and the conversion efficient is nearly double of that without an IB.

5.2.2 Donor Density (N_D)

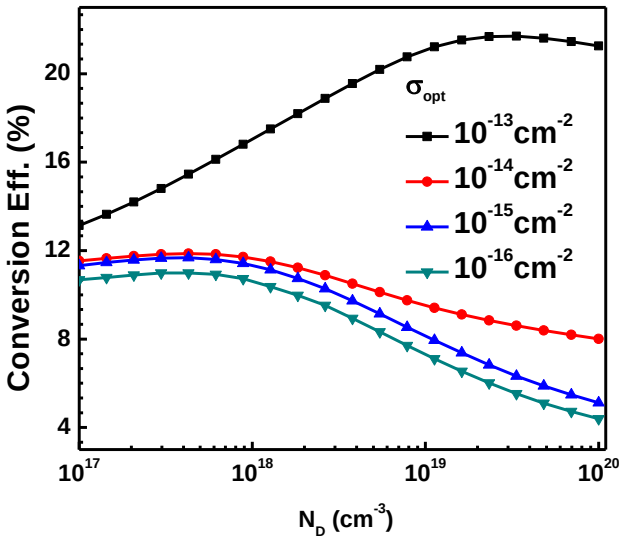

Figure 5.11 Conversion efficiency vs donor density (N_D) in an n^+-p ZnTeO IBSC with the IB in p side, Cp=$10^{-14}cm^2$, N_A=$10^{15}cm^{-3}$, No=10^{20} cm^{-3}, E_G=2.29eV, E_O=1.75eV, μ_n=μ_p=100 cm^2/Vs, underAM1.5 .

Despite no sub-band absorption in the n side of the cell, two factors incorporating the donor density (N_D) in this region reshape the conversion efficient. One is the increase of self-build potential and decrease of diffusion current for high donor density, leading to increase the V_{oc} and then conversion efficient. On the other hand, both the hole diffusion length (L_p) and the n side depletion width (x_n) are shorten by increasing donor density with negligibly changing the electron diffusion length (L_n) and the p side depletion region(x_p), consequently reduce absorption and the efficiency. Higher optical cross

section of the IB leads to less dependence of photon current on the n side, and higher optimal N_D as shown in Figure 5.11.

5.2.3 Acceptor Density (N_A)

Increase of the acceptor density (N_A) also results in large self-built potential and small electron diffusion current, leading to large open circuit voltage and high the conversion efficiency as shown in Figure 5.12.

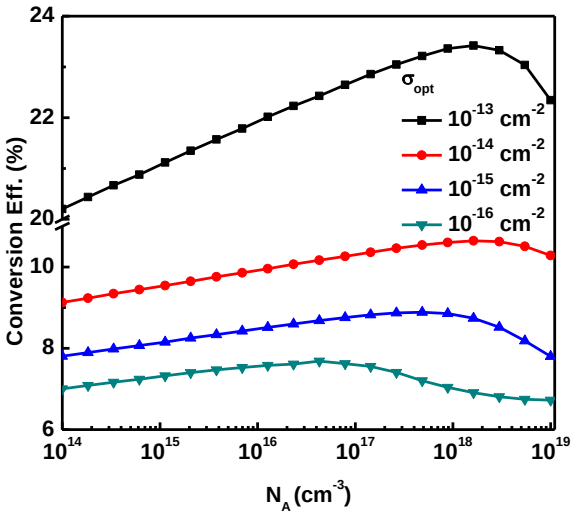

Figure 5.12 Conversion efficiency vs donor density (N_A) in an n^+-p ZnTeO IBSC with the IB only in p region, Cp=10^{-14}cm^2, N_D=10^{19}cm^{-3}, No=10^{20} cm^{-3}, E_G=2.29eV, E_O=1.75eV, μ_n=μ_p=100 cm^2/Vs, underAM1.5.

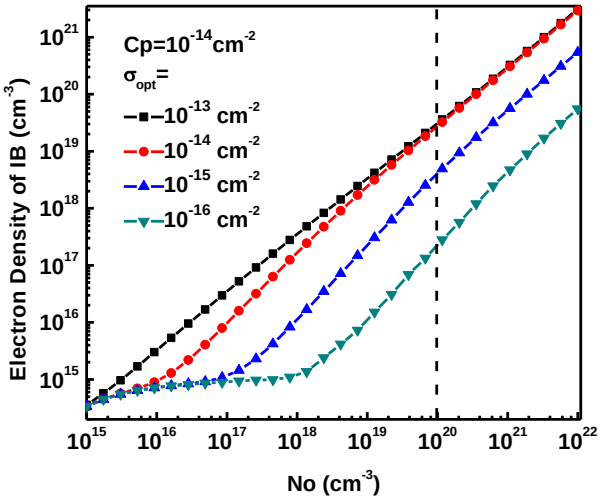

Figure 5.13 Electron occupation (Ni) vs IB density (No) in an n^+-p ZnTeO IBSC with the IB only in p region, $N_D=10^{19}cm^{-3}$, $N_A=10^{15}$ cm^{-3}, E_G=2.29eV, E_O=1.75eV, $\mu_n=\mu_p=100$ cm^2/Vs, underAM1.5.

However, detrimental effects, such as reduction of the depletion width only appears when N_A reaches the same level of electron densities of the IB (N_I) in the depletion region whose values depend on the optical cross-sections as marked in Figure 5.13. Then the optimal acceptor densities (N_A) are achieved.

5.2.4 Concentrated Sunlight (X)

The electron occupation of the IB either in the depletion region or in the diffusion region increases with sunlight intensity as shown in Figure 5.14 (a) and (b) respectively.

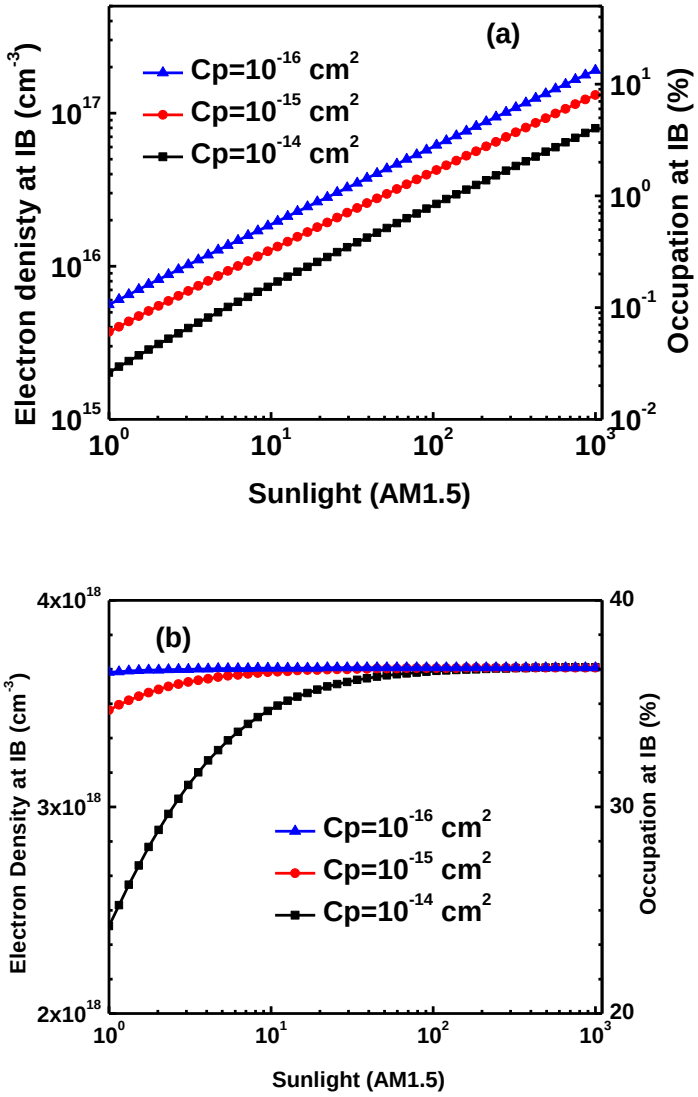

Figure 5.14 Electron occupation (Ni) vs sunlight intensity, in an n^+-p ZnTeO diode with $\sigma_{opt}=10^{-14}cm^2$, $No=10^{19}cm^{-3}$, $N_D=10^{19}cm^{-3}$, $N_A=10^{15}\,cm^{-3}$, $E_G=2.29eV$, $E_O=1.75eV$, $\mu_n=\mu_p=100\ cm^2/Vs$ in (a) the diffusion region (b) the depletion region.

The electron occupation of the IB in the diffusion region is less 0.1% under one sun and less 10% under 1000 suns regardless of the capture cross-sections as shown in the Figure 5.14(a). Therefore, the photo-carrier generation from the VB to the IB is always much stronger than that from the IB to the CB. In this case, increase of electron occupation in the IB will enhance the absorption coefficient from the IB to the CB (α_{IV}), the electron lifetime and the electron diffusion length, and consistently enhance the

photon-electron current in the diffusion region. On the other hand, the electron occupation in the IB is already more than 20% under one sun. The generation from the VB to the IB is nearly balanced to that from the IB to the CB. Increase of occupation may break the balance and does not necessarily lead to generate more photo carriers, but it certainly results in shrink of the depletion region and minuses the photon current generated in this region. An example of the conversion efficiency dependent on the sunlight intensity is given in Figure 5.15. For the low capture cross-section (10^{-16} cm^2), the occupation in the depletion region is nearly fixed as shown in Figure 5.14 (b) regardless of light intensity but the occupation in the diffusion region increase linearly with light intensity. Therefore, the conversion efficiency is consistently enhanced. But it is not the case for the high capture cross-section.

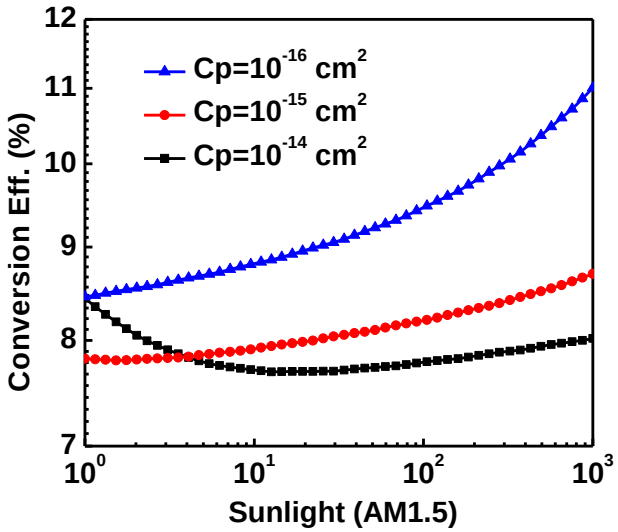

Figure 5.15 Conversion efficiency vs sunlight intensity in an n^+-p ZnTeO diode with $\sigma_{opt}=10^{-14}cm^2$, $No=10^{19}cm^{-3}$, $N_D=10^{19}cm^{-3}$, $N_A=10^{15}$ cm^{-3}, E_G=2.29eV, E_O=1.75eV, $\mu_n=\mu_p=100$ cm^2/Vs .

5.3 Parasitic Factors

The parasitic effects such as imperfect semi-metal contacts, semi-semi interfaces and so on are discussed in this section, which dramatically influence the performance of real solar cell devices.

5.3.1 Series Resistance (R_s) and Shunt Resistance (R_{sh})

Two parasitic parameters, series resistance (R_s) and shunt resistance (R_{sh}), are listed in the circuit model shown in the Figure 5.16 with the current-voltage (J-V) relationship described in equation (5.19).

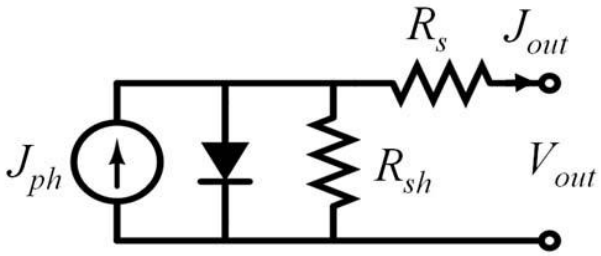

Figure 5.16 Circuits model of a solar cell including series resistance and shunt resistance.

$$J_{out} = J_o[\exp(\frac{q(V_{out} - J_{out}R_s)}{nkT}) - 1] + \frac{V_{out} - J_{out}R_s}{R_{sh}} - J_{ph} \qquad (5.19)$$

where J_{out} is the output current density, J_o is the saturation current density of the diode, J_{ph} is the photo current density, V_{out} is the output voltage, q is an electronic charge unit, k is the Boltzmann' constant, and T is absolute temperature, n is the ideal factor of the diode.

For an ideal diode, R_s is expected to be zero and R_{sh} is infinite. Quantitatively the effect of R_s and R_{sh} on J-V curves are revealed in Figure 5.17 (a) and (b) respectively. R_s mainly degrades the short circuit current (J_{sc}), and R_{sh} mainly degrades open circuits voltage (V_{oc}). Both of them can deteriorate the Fill Factor significantly. The figures also indicate the loss of conversion efficiency is negligible when R_s is less than $1\Omega.cm^2$ and R_{sh} is more than $1k\Omega.cm^2$.

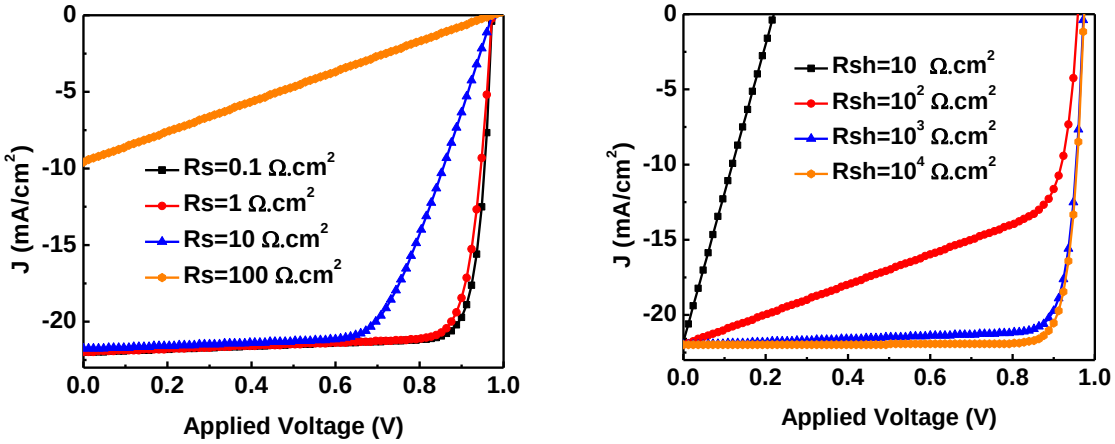

Figure 5.17 (a) J-V curves vs R_s with J_o=10^{-18}A/cm^2, J_{ph}=22mA/cm^2, R_{sh}= 1kΩ.cm^2, and ideality factor n=1. (b) J-V curves vs R_{sh} with J_o=10^{-18}A/cm^2, J_{ph}=22mA/cm^2, R_s= 1Ω.cm^2, and ideality factor n=1.

Three main sources for series resistance (R_s) are shown in Figure 5.18.

- Contact resistance ($R_{contact}$) between metal electrode and semiconductor. Good ohmic contact process is required to achieve a low contact resistance.
- Bulk resistance (R_{bulk}) from the inactive and active semiconductor region, such as cladding layers, absorption layers.
- Spread resistance (R_{spread}) from the current spreading based on electrode geometry.

The shunt resistance (R_{sh}) results from the leakage current through the device edge, the pin holes, and other defects inside devices.

All of these parameters are traded off with other factors in a solar cell device, and will be discussed in more detail in the Chapter 6 and 7

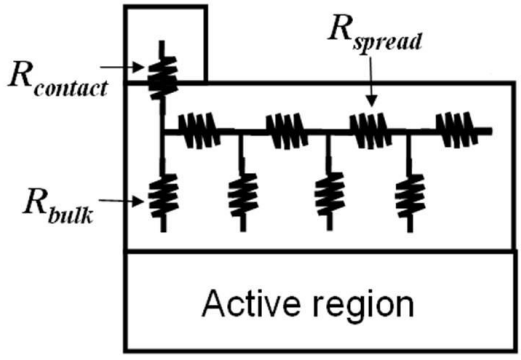

Figure 5.18 Composition of series resistance in a semiconductor diode.

5.3.2 Hetero-junction

ZnTe epi-layers usually show p type conductivity because of intrinsic defects. And it is very difficult to achieve n type conductivity as discussed in Chapter 2. The achievement of ZnTe homo-junction has scarcely succeeded[81]. Hetero-junction is an alternative solution to realize a ZnTe diode with a p-type layer of ZnTe but an n-type layer consists of other semiconductors, such as ZnO, ZnSe, and GaAs and so on. The additional structural defects are certainly introduced into hetero-junction because of lattice and crystal structure mismatch. Therefore, zinc blend ZnSe and zinc blend GaAs are better choices than wurtzite ZnO for low structural defects.

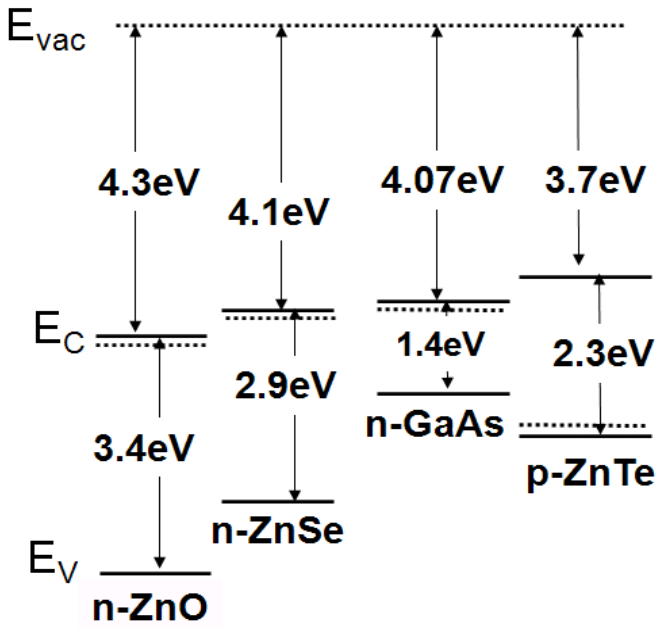

Figure 5.19 Band alignments for n-ZnO, n-ZnSe, n-GaAs and p-ZnTe.

On the other hand, band alignment as shown in Figure 5.19 is also a major factor to select the hetero-junction material. For example, band alignment of the VB between n-GaAs/p-ZnTe favors hole injection form ZnTe to GaAs under forward bias, resulting in small open circuit voltage. However, both electron injection from n side and hole injection from p side under forward bias are barred at either ZnO/ZnTe or ZnSe/ZTe interface. Overall, ZnSe may be the best choice among these three candidates for hetero-junction. And more detail also will be discussed in the following chapters.

5.3.3 Additional Absorption and Reflection

Absorption and reflection at the window layer should be as small as possible to maximize the incident photon intensity, which usually requires large band gap and low refractive index for the window layer. ZnO with the band gap of 3.4eV and refactive index of 1.9 may be a good choice.

5.4 Summary

The CRT model has given basic rules to guide the design of IBSC based on ZnTeO. This model is updated by including the band profile redistribution for electron occupation in the IB, and the dependence of minority carrier lifetime on the electron occupation of the intermediate band. The effect of material parameters, device structure and operation conditions on the overall conversion efficiency are reevaluated.

In n^+-p ZnTe junction with the IB in the p side, the IB is nearly half filled in the depletion region and almost empty in the diffusion region under steady state. Both the open circuit voltage and fill factor degrade but the short circuit current increases comparison to those in a ZnTe junction without an IB.

The overall efficiency improvement from the IB extremely depends on its optical cross-section. Once it is larger than $10^{-14}cm^2$, the conversion efficiency of ZnTeO based IBSC can be more than 20% with the optimal IB density in range of 10^{20}-10^{21} cm^{-3} regardless of capture cross section from 10^{-16}-10^{-13} cm^2. The efficiency of ZnTe IBSC is almost double than that of a ZnTe cell without an IB.

The optimal doping concentration is in the range 10^{18}-10^{19} cm^{-3} for the n side, and 10^{16}-10^{17} cm^{-3} for the p side, dependent on the optical cross-section.

Concentrated sunlight does increase the electron occupation of the IB both in the depletion region and the diffusion region. However, only increase of occupation in the diffusion region leads to enhance the conversion efficiency.

The circuit model indicates the series resistance should be less than $1\Omega.cm^2$ and shunt resistance larger than $1K\Omega.cm^2$ for a practical solar cell device. N-type ZnSe is believed to a best candidate to form a hetero-junction for a ZnTe based diode based on the crystal structure and band alignment. ZnO may be a good choice for the window layer.

Chapter 6

Demonstration of ZnTeO Based IBSC

Oxygen doping in ZnTe is applied to a junction diode in the aim of utilizing the associated electron states near 0.4-0.7eV below the conduction band edge as an intermediate band for photovoltaic solar cells. The ZnTeO diodes confirm extended spectral response below the band edge relative to undoped ZnTe diodes, and demonstrate a 100% increase in short circuit current, 15% decrease in open circuit voltage, and overall 50% increase in power conversion efficiency. Sub-band gap excitation at 650 nm and 1550 nm confirms response via a two-photon process and illustrates the proposed energy conversion mechanism for an intermediate band solar cell.

6.1 Device Structure

ZnTeO based intermediate band solar cells were initially realized by a p-GaAs/n-ZnTe heterojunction structure because 1) ZnTe epi-layers are achievable on GaAs substrates, 2) GaAs substrates can be degenerately doped as n type to form p-ZnTe/n-GaAs hetero-junction, which simplifies device fabrication.

6.1.1 Device Structure

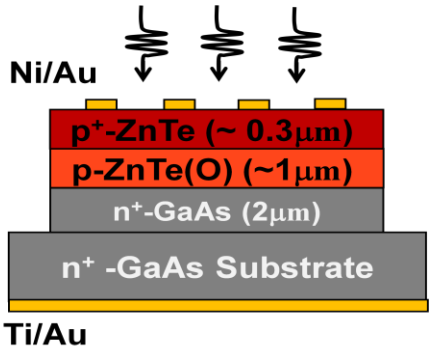

Figure 6.1 Device cross-section schematics of p-ZnTe/n-GaAs junction.

A typical device schematic is shown in Figure 6.1.The substrate is n type GaAs with the electron concentration about $2\times10^{18}cm^{-3}$, the mobility about 2000 cm^2/v.s, the thickness near 0.5mm. First, a lightly doped p-type ZnTe absorber layer was grown on the substrate with or without oxygen doping, followed by a highly doped p-type ZnTe contact layer. Metal contacts were formed on the top and bottom sides. The typical thicknesses are 1μm for the absorption layer, 0.3 μm for the ZnTe contact layer, and 100nm for both the top and the bottom metal contact layers. The electrical parameters used in calculation of energy band diagram are listed in Table 6-1. The calculated energy band diagram is illustrated in Figure 7.2.The discontinuities of the conduction band (ΔE_C) and the valence band (ΔE_V) are about 0.37eV and 0.5eV respectively, where ΔE_C is a barrier for electron injection from n-GaAs to p-ZnTe, while ΔE_V assists hole injection from p-ZnTe to n-GaAs.

Materials	Doping Con.	Electron Affinity	Band Gap	Effective Mass
p^+-ZnTe	$10^{19}\,cm^{-3}$	3.7eV	2.29eV	$m_h=0.2m_e$
p-ZnTe(ZnTeO)	$10^{15}\,cm^{-3}$	3.7eV	2.29eV	$m_h=0.2m_e$
n^+-GaAs	$2\times10^{18}\,cm^{-3}$	4.07eV	1.42eV	$m_e=0.067m_0$

Table 6-1 Electrical parameters for energy band diagram calculation.

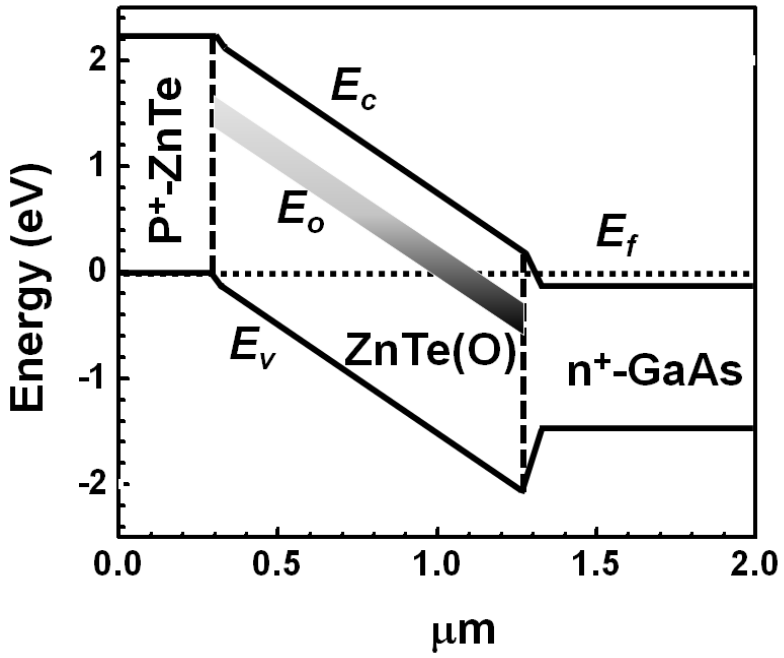

Figure 6.2 Calculated band diagram for p-ZnTe/n-GaAs junction.

6.1.2 Material Growth and Device Fabrication

The solar cells with n^+-GaAs/p-ZnTeO/p^+-ZnTe were grown by the following steps.

1. The epitaxy ready GaAs (100) substrates were cleaved into 1cm ×1cm and loaded in the growth chamber of the MBE system with base pressure $<10^{-8}$ Torr.
2. The GaAs substrates were heated up to 700 ^oC to remove surface oxides.
3. After surface cleaning, the substrates were heated to 250 ^oC. The Beam Equivalent Pressure (BEP) of the zinc cell was set to 5×10^{-7} Torr, and 1.2×10^{-6} Torr for the tellurium cell. Oxygen was introduced by an Oxford ECR cell with oxygen flow rate of 1sccm, resulting in the growth chamber pressure increase to 2×10^{-5} Torr. The growth rate is about 1.5μm/hr for ZnTeO growth under the above conditions.
4. The growth chamber was pumped down to $2\text{-}3\times10^{-8}$ Torr to pump residual oxygen. Nitrogen was then introduced by the ECR cell for p-type doping of ZnTe at a flow rate of 2sccm, resulting in approximately 10^{19} cm^{-3} hole concentration.

The solar cell with n-GaAs/p-ZnTe/p^+-ZnTe structure was grown as same steps as above except turning off oxygen flow. Then the solar cell devices were fabricated using the following procedure.

1. Top contacts consist of 30nm Ni as an adhesion layer and 70nm Au as a highly conducting layer, both of which were deposited by e-beam evaporation at room temperature, and then lifted off into the designed pattern. The pattern was generated by photolithography, as described in Appendix II.
2. Solar cells were isolated using photolithography and wet chemical etching. The mesa etching was executed by a solution consisting of deionized water, Hydrogen Peroxide (H_2O_2) solution, and Phosphoric acid (H_3PO_4) at a volume ratio of 2:1:1. Both GaAs and ZnTe can be etched by this solution. The etching rate of this mixture solution for ZnTe is about 1.5μm/min.
3. Bottom contacts at the backside of the GaAs substrate consist of 50nm Ti as an adhesion layer and 100nm Au as a contact layer, both of which were deposited by e-beam evaporation at room temperature.
4. The solar cell deviceswere annealed under nitrogen ambient at 200^oC for 10 minutes in order to reduce the metal/semiconductor contact resistance.

The fabricated solar cell devices are illustrated in Figure 6.3.

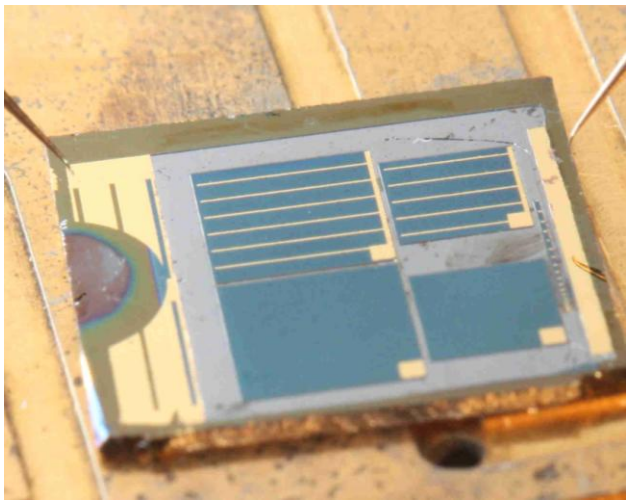

Figure 6.3 Top view of fabricated ZnTeO based solar cells on GaAs substrate.

6.2 Characterization and Analysis

Current-voltage and spectral response measurements were used to identify whether oxygen states in ZnTe are beneficial to solar energy conversion.

6.2.1 Current-Voltage Characteristics

Current-voltage characteristics were measured at room temperature using a Keithley 4200 semiconductor parametric test system. The current-voltage curves for ZnTe and ZnTeO cells measured in the dark are shown in Figure 6.4. Both cells rectify current strongly with on/off ratio of approximately 50 for the ZnTe cell and 200 for the ZnTeO cell. The ideality factor of the ZnTe cell is about 3.3, indicating high non-radiative recombination in the ZnTe region, likely due to the high lattice mismatch between the ZnTe epi-layer and the GaAs substrate. The forward current of the ZnTeO cell clearly demonstrates two distinct regions, likely due to additional high recombination centers induced by oxygen doping. The ideal factors are approximately 6.7 in the region from 0.1V to 0.5V forward bias, and 3.1 in the region from 0.5V to 1.0V.

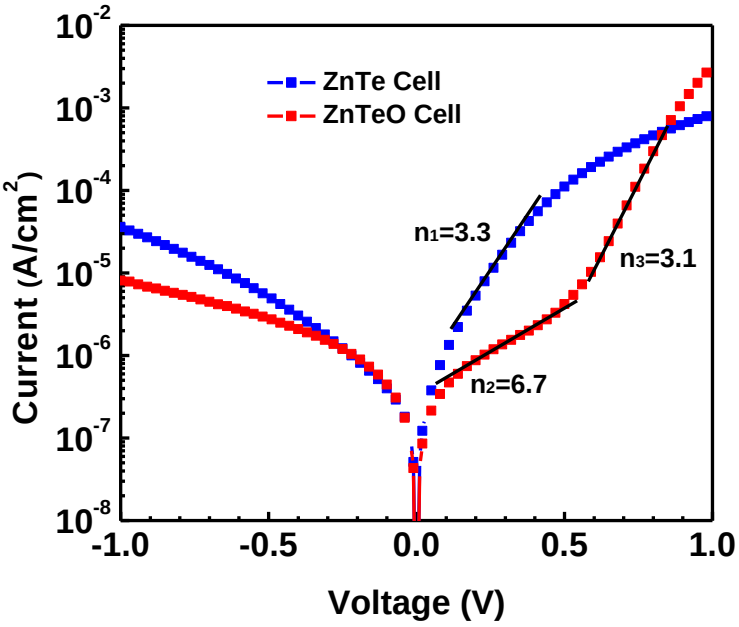

Figure 6.4 Current-Voltage curves of ZnTe and ZnTeO cells under dark.

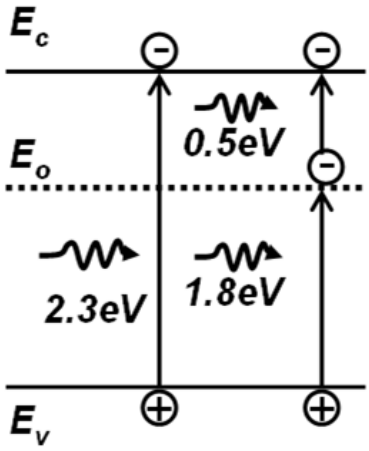

Figure 6.5 Schematics of optical transitions of ZnTeO under solar illumination.

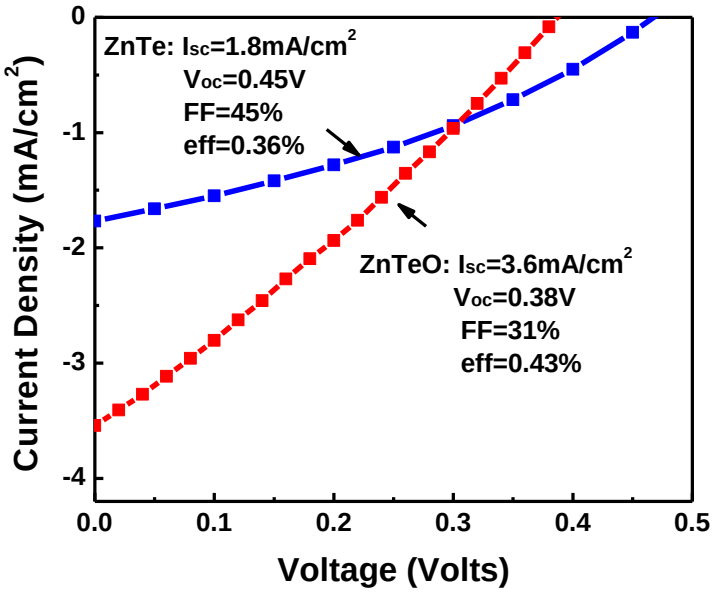

Figure 6.6 Solar cell current-voltage curves under AM1.5 conditions for ZnTe and ZnTeO diodes.

The possible optical transitions of ZnTeO under solar illumination are illustrated in Figure 6.5. The current-voltage characteristics for ZnTe and ZnTeO solar cells under AM 1.5 illumination are shown in Figure 6.6. A clear photovoltaic response is observed for both sets of devices, where an increased short circuit current density (J_{sc}) and reduced open circuit voltage (V_{oc}) are observed for the ZnTeO, with an overall improvement of 50% in the power conversion efficiency. The increase in J_{sc} is approximately double corresponding larger number of photo-generated carriers. The source for the approximate 15% reduction in V_{oc} may be due to a number of factors, including increased non-radiative recombination and carrier occupation in the IB lowering the Fermi level position. The overall conversion efficiency of both devices are both relatively low (<1%), where significant development of materials growth and device structures are required to improve efficiency. Factors degrading conversion efficiency include high series resistance, low shunt resistance of the junction, and small carrier lifetime associated with the junction technology and defects corresponding to the large lattice mismatch of the active region and GaAs substrate. Equivalent circuit modeling of the I-V characteristics provide values for the shunt resistance and series resistance of the devices, which were determined to be on the order of R_{shunt}=3000Ω-cm^2 and R_{series}=300Ω-cm^2. The value of

series resistance is clearly a major limitation, where reduction to a more typical $R_{series}=1\Omega\text{-cm}^2$ is estimated to provide a power conversion efficiency value of approximately 5% for the ZnTeO device in Figure 6.6. Further significant efficiency improvements are expected with the development of suitable buffer layers and ZnTe or II-VI based junction technologies to reduce defect density and associated non-radiative recombination.

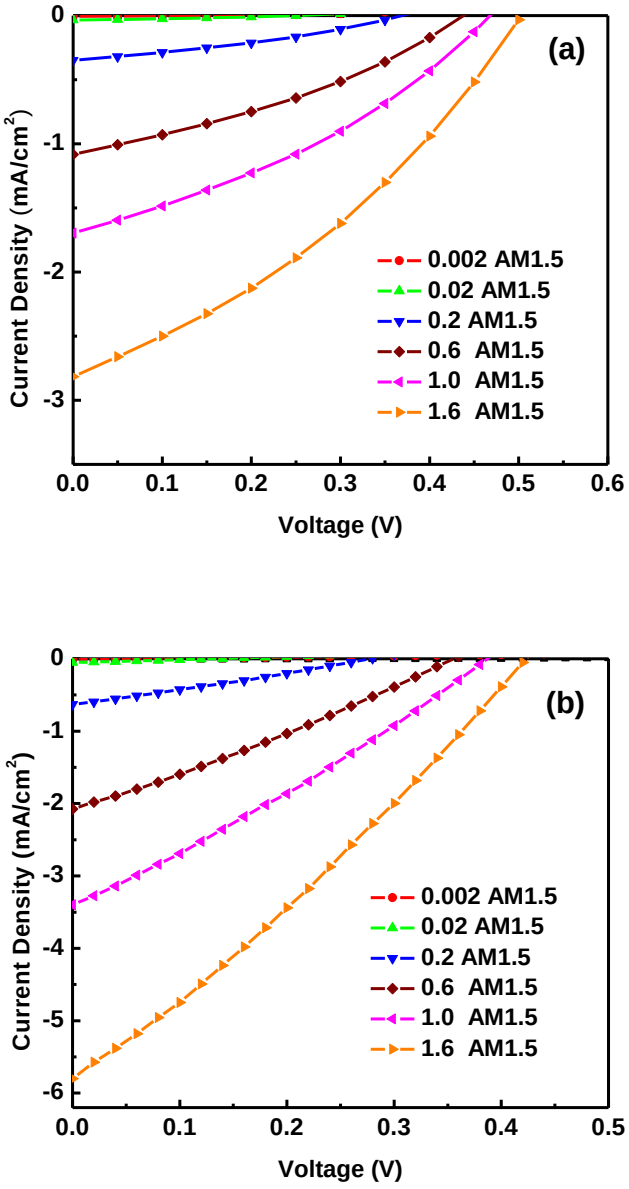

Figure 6.7 Current-Voltage curves under varying incident solar power for (a) ZnTe cell (b) ZnTeO cell.

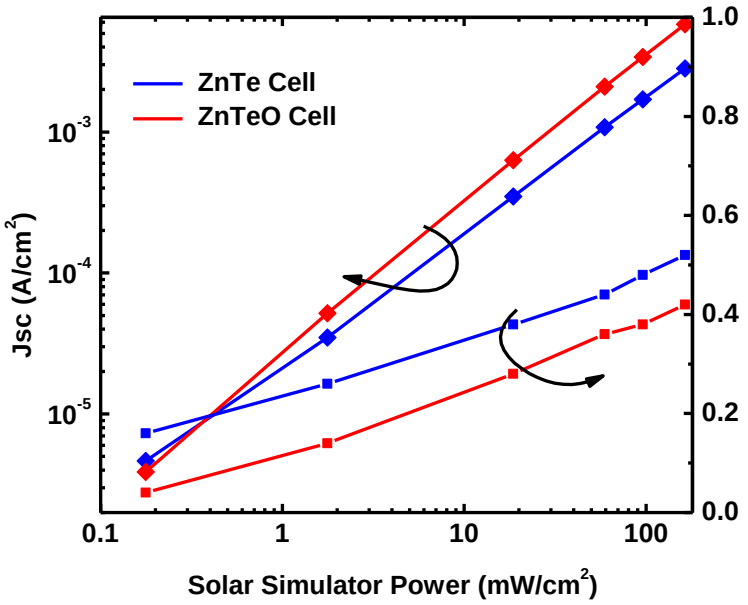

Figure 6.8 V_{oc} and J_{sc} vs incident solar power of ZnTe and ZnTeO cells.

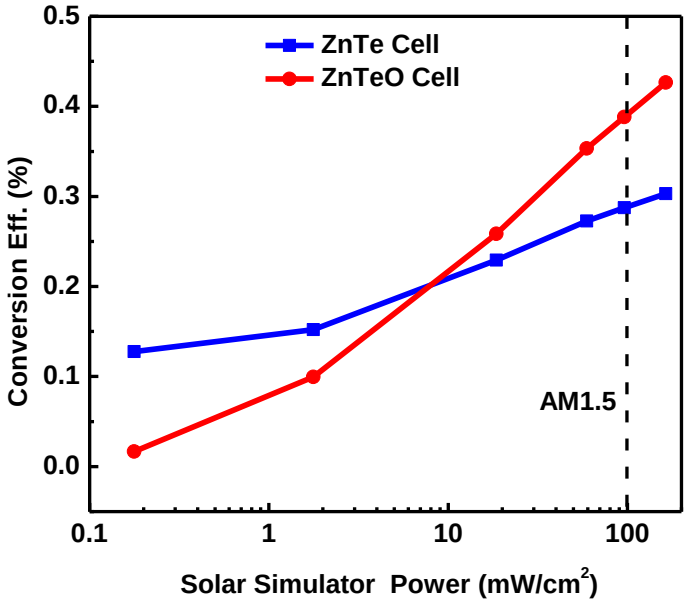

Figure 6.9 Conversion efficiency vs incident solar power of ZnTe and ZnTeO cells .

The current-voltage curves were measured under varying solar power intensity as shown in Figure 6.7. The V_{oc} increases logarithmically and the J_{sc} increases linearly with the incident solar power intensity as illustrated in Figure 6.8. Both V_{oc} and J_{sc} of the ZnTeO cell are less than those of the ZnTe cell under low illumination (around 0.5mW/cm^2), indicating oxygen states act as recombination centers rather than generation centers. However, J_{sc} of the ZnTeO increases more rapidly with power intensity than that of ZnTe, where the conversion efficiency of the ZnTeO cell surpasses the ZnTe efficiency when the incident power is about 10mW/cm^2, equal to one tenth AM1.5 intensity as shown in Figure 6.9.

6.2.2 Monochromatic Photon Response

Photoluminescence measurements were taken using excitation from a HeCd 325nm laser, a grating spectrometer, lock-in amplification, and a photodiode detector. Solar cell optical response measurements were taken using a grating spectrometer for spectral response. A room-temperature photoluminescence spectrum for ZnTeO grown on GaAs is shown in Figure 6.10, indicated both a bandedge response for ZnTe at 2.3 eV and a strong sub-bandgap response related to oxygen doping in the range of 1.6-2.0 eV. In a majority of the ZnTeO samples, the spectrum is dominated by defect emission, where the spectrum in Figure 6.10, was chosen in order to illustrate both defect and ZnTe bandedge emission. In comparison, the photoluminescence spectrum for an undoped ZnTe sample shows a sharper bandedge transition, and a much weaker defect emission. The presence of defect emission in the undoped ZnTe sample is believed to be due to residual oxygen present in the growth chamber. The strong radiative emission due to oxygen in ZnTe is consistent with previous detailed studies[82-84]. The strong emission for the oxygen defect in ZnTe denotes a highly radiative transition, and is therefore a highly desirable characteristic for the IB solar cell. Complementary optical absorption spectra inferred from transmission measurements have been reported in chapter 3 for samples deposited on sapphire under varying oxygen partial pressure[85]. A sharp bandedge response is observed for ZnTe without oxygen, while increasing sub-bandgap optical absorption is observed with increasing oxygen. Sub-bandgap response occurs when an electron is excited from the valance band to the oxygen states by absorbing one sub-bandgap photon,

and then from the oxygen states to the conduction band with the assistance of another sub-bandgap photon. The sub-bandgap optical absorption is consistent with the photoluminescence characteristics, and is similarly attributed to oxygen defects in ZnTe.

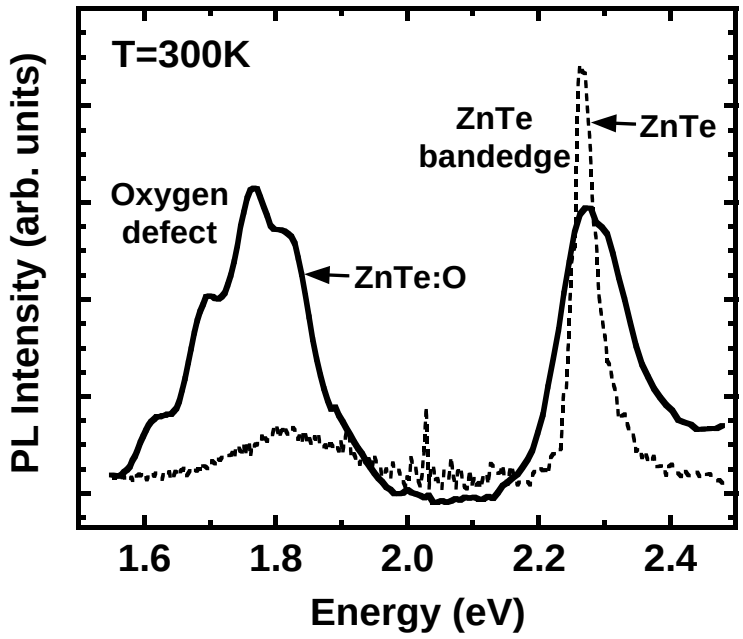

Figure 6.10 Room-temperature photoluminescence spectra of ZnTeO illustrating emission from both the ZnTe bandedge and oxygen related defect states.

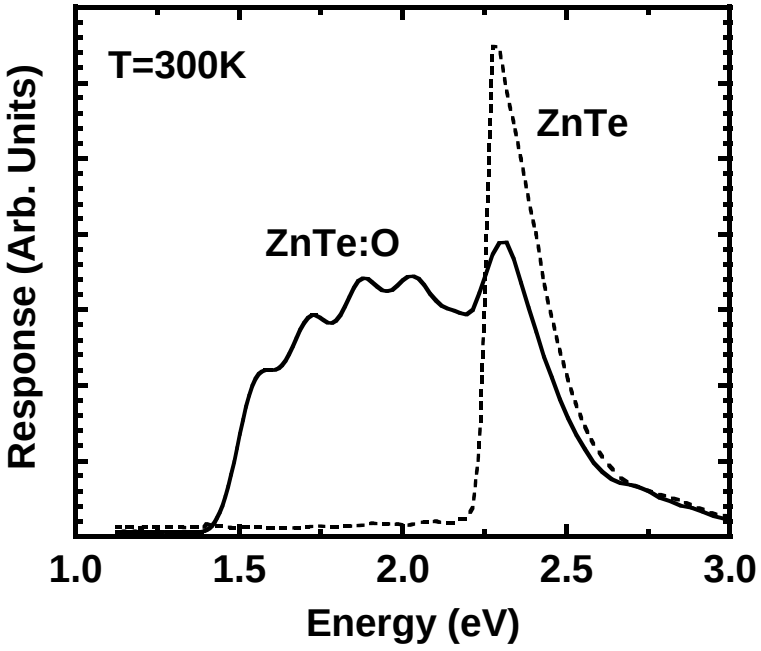

Figure 6.11 Solar cell spectral response for ZnTe and ZnTe:O diodes.

The spectral response for diodes fabricated with ZnTe and ZnTeO absorber layers is shown in Figure 6.11. For the case of the ZnTe diode, a sharp bandedge response is observed near 2.25 eV, with a gradual response decrease with increasing energy. The negligible response below the bandedge for the ZnTe diode indicates that the GaAs substrate does not contribute to the photocurrent, where the large band offsets block carrier transfer from n-GaAs to p-ZnTe. The response decrease at high energy is attributed to an increasing fraction of optical absorption in the heavily doped p type ZnTe cap layer, where carrier collection will be impeded due to short carrier diffusion lengths in this layer. The ZnTeO diode exhibits enhanced spectral response below the bandedge, where response is observed for energies down to 1.5 eV. It should be noted that the spectral response was obtained using monochromatic light, and does not necessarily represent the true spectral response of a solar cell where a full spectrum is incident on the device. The monochromatic incidence does not provide a means of "pumping" carriers from the valence band to intermediate band in order to enable absorption from the intermediate to the conduction band.

6.2.3 Two-Photon Absorption

The multi-photon process associated with intermediate-band transitions was further investigated using illumination by 650 nm (1.91 eV) and 1550 nm (0.8 eV) laser sources corresponding to energies below the ZnTe band edge as shown in Figure 6.12.

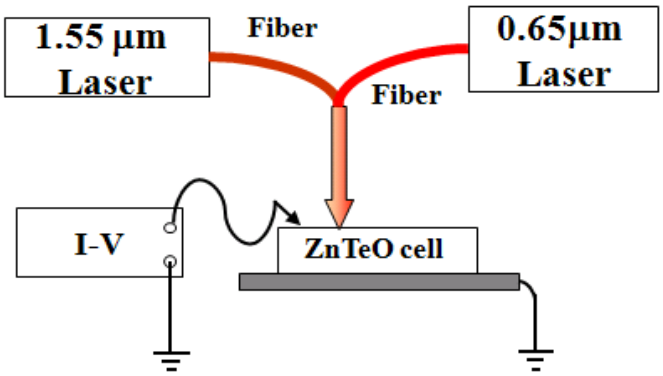

Figure 6.12 Experimental set-up for two-photon absorption measurement.

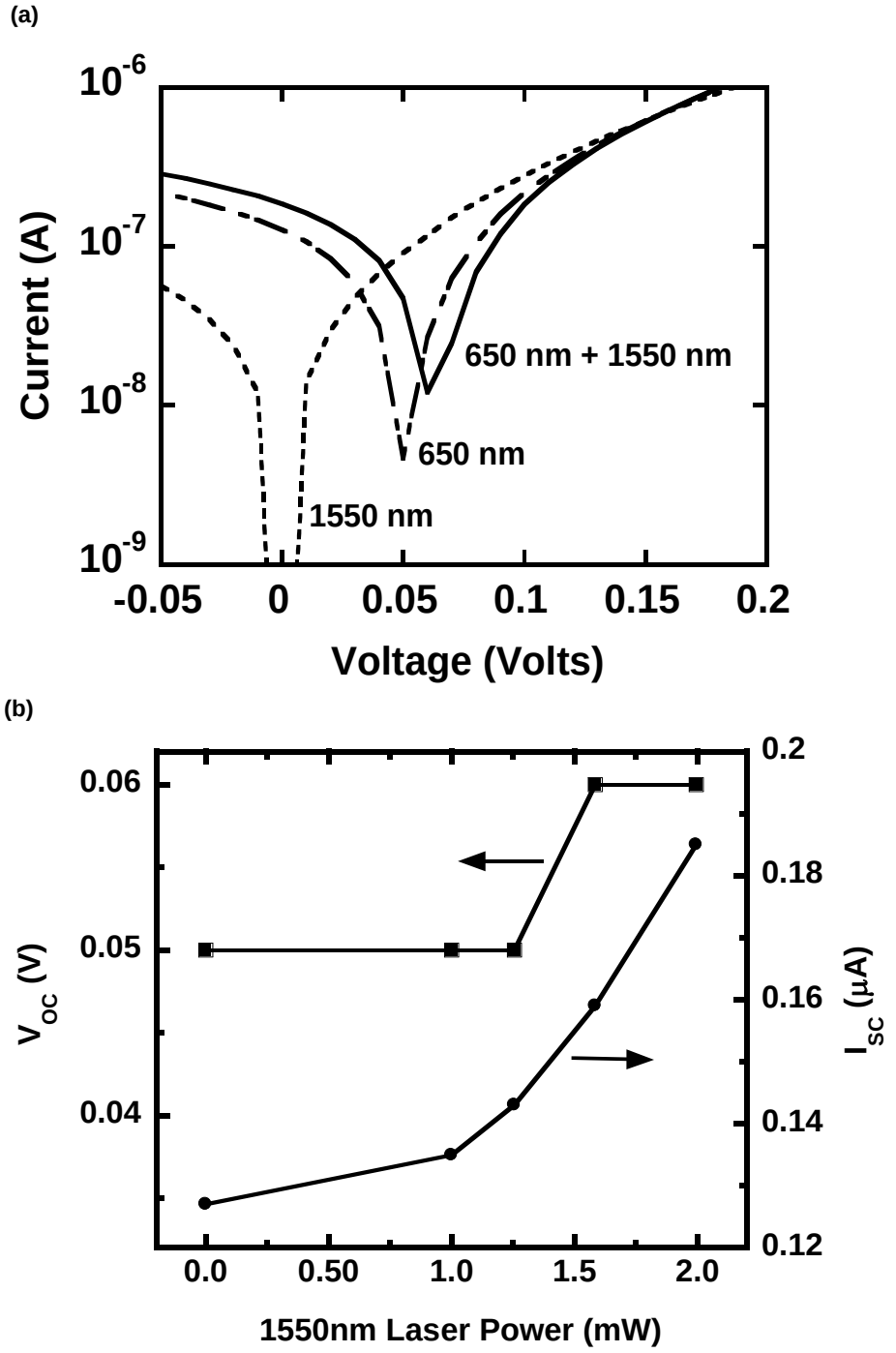

Figure 6.13 Sub-bandgap response of a ZnTe:O solar cell with 0.09 cm^2 device area shown by (a) current-voltage characteristics under 1550nm, 650nm, and 650nm + 1550nm excitation, and (b) I_{SC} and V_{OC} for variable 1550nm laser excitation and constant 650nm excitation.

The 650 nm laser provides energy necessary to excite an optical transition between the valence band and IB, while the 1550 nm laser provides the energy necessary to excite a transition from IB to conduction band. The ZnTe diodes did not exhibit any detectable response at these wavelengths. The ZnTeO diodes do not show any detectable response for sole illumination at 1550nm, but do demonstrate significant response for illumination at 650nm, consistent with the response observed at 1.91 eV in Figure 6.13(a). The observed response for monochromatic 650 nm illumination suggests that carriers are excited into the IB and are subsequently promoted to the conduction band by further 650 nm photons, thermionic emission, or tunneling. Alternatively, it would be possible to extract carriers directly from the IB for the case where transport via IB states is significant. However, IB transport is unlikely in these experiments due to the low density of oxygen states and corresponding large spacing between neighboring oxygen atoms. The addition of 1550 nm illumination to 650 nm illumination (simultaneous excitation) results in an increase in photocurrent and open circuit voltage. The photovoltaic response increases monotonically with increasing 1550nm power density Figure 6.13(b), providing supporting evidence that the intended two-photon process for IB solar cells may be occurring in the ZnTeO device. The non-linear increase in short circuit current with increasing 1550 nm illumination suggests that IB solar cell efficiency may be improved under higher excitation levels, indicating that these devices may further benefit from solar concentration.

The short circuit current has an approximate square root dependence on 1550nm laser intensity as shown in Figure 6.14. Based on the limited data set, the source of nonlinearity between J_{sc} and 1550 nm laser intensity is inconclusive. Possible explanations for this behavior are a two-photon absorption process, nonuniform absorption in the material, and overlap of absorption bands. Nonlinear behavior may also be related to material defects, where quantum efficiency is less than one and may have a dependence on incident laser intensity.

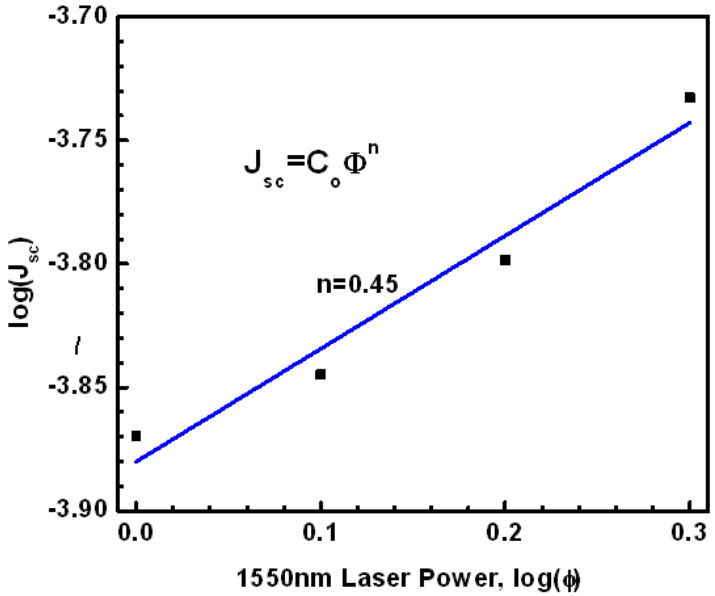

Figure 6.14 Correlation of Jsc with 1550nm laser power in log scale

6.3 Summary

In conclusion, ZnTeO has been applied to diode structures exhibiting enhanced response to the solar spectrum in comparison to ZnTe due to photo-excitation below the bandgap energy. The increase in response for the ZnTeO diodes translates to an approximate doubling of the short circuit current, while suffering an approximate 15% decrease in open circuit voltage. Sub-bandgap excitation experiments under 650nm and 1550nm excitation demonstrate the two-photon response characteristic desired for intermediate band solar cells and serve as a basis for further efforts to develop ZnTeO and other dilute alloys or impurity materials for enhanced solar cell conversion efficiency.

In this chapter, ZnTeO diodes were realized by p-ZnTe/n-GaAs hetero-structures in order to simply the device fabrication. However, the conversion efficiency is severely limited by 1) high dislocation density in the absorber layers and interface defects because of large lattice mismatch, 2) possible reverse doping either in the p-ZnTe layer by Ga diffusion or the n-GaAs substrate by Zn diffusion, 3) band alignment for amplifying hole injection from p-ZnTe to n-GaAs, 4) strong absorption in the p^+-ZnTe window layer. Further significant efficiency improvements are expected with the development of suitable buffer layers and ZnTe or II-VI based junction technologies to reduce defect density and associated non-radiative recombination.

Chapter 7

Solar Cell Device Structure Improvement Efforts

Initial efforts were conducted to improve ZnTe diode characteristics. The ZnO/ZnTe hetero-structure was studied in the goal of improving the ideality factor and to reduce series resistance. Furthermore, the effect of a ZnSe buffer between ZnO/ZnTe was investigated in order to reduce interface defects between ZnO/ZnTe and provide a more lightly doped n-type layer adjacent to the ZnTe-based absorber layers.

7.1 Device Structure

The low formation energy of n-type native defects including Zn interstitials, O vacancies, and unintentional donors such as hydrogen leads to high background n-type carrier concentrations in ZnO[86]. With doping of group III elements[87], such as Al, Ga, In, electron concentration can be over $10^{20}cm^{-3}$. Furthermore, wide bandgap (E_g=3.34eV at room temperature) and low refractive index (around 2.0 in the visible range) of ZnO make it attractive as a top layer with low absorption and reflection.

7.1.1 Device Structure

The schematic of a ZnO/ZnTe junction is shown in Figure 7.1. The device was fabricated on a p-type GaAs substrate with the hole concentration about 2×10^{18} cm^{-3}, the mobility around 200 $cm^2/V.s$. A heavily doped p-type ZnTe was used as a buffer layer, followed by a lightly doped p-type ZnTe layer and n-type ZnO. The electrical parameters to calculate the energy band diagram are listed in Table 7-1.

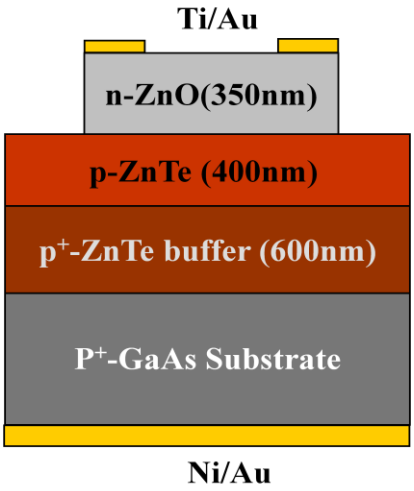

Figure 7.1 Schematics of n-ZnO/p-ZnTe heterojunction on a GaAs substrate.

Materials	Doping Con.	Electron Affinity	Band Gap	Effective Mass
n-ZnO	10^{18} cm^{-3}	4.3eV	3.34eV	$m_h=0.24m_0$
p-ZnTe	10^{15} cm^{-3}	3.7eV	2.29eV	$m_h=0.2m_0$
p^+-ZnTe	10^{19} cm^{-3}	3.7eV	2.29eV	$m_h=0.2m_0$
p^+-GaAs	2×10^{18} cm^{-3}	4.07eV	1.42eV	$m_h=0.5m_0$

Table 7-1 Electrical parameters for energy band diagram calculation

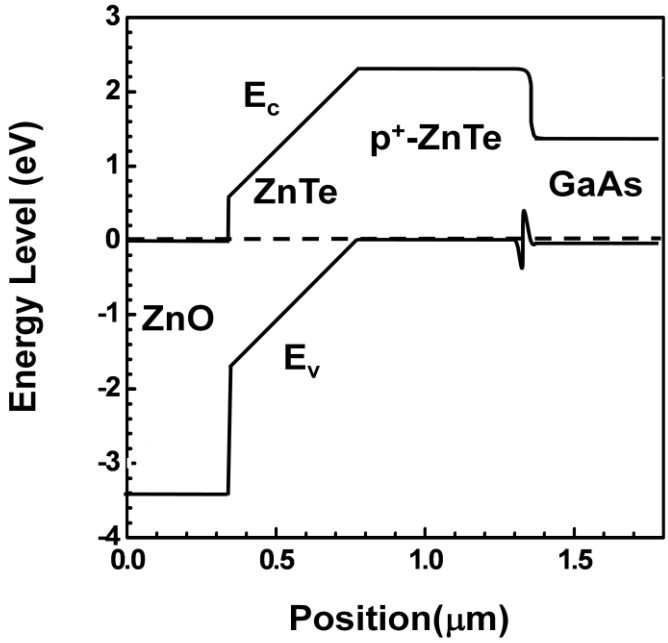

Figure 7.2 Calculated energy band diagram at thermal equilibrium.

The calculated energy band diagram is illustrated in Figure 7.2. The band alignment between ZnO and ZnTe is type II, whose discontinuities at the conduction band and the valence band are 0.6eV and 1.64eV respectively. These discontinuities block majority carrier injection from both n-type ZnO to p-type ZnTe and p-type ZnTe to n-type ZnO, potentially reducing the diode saturation current.

7.1.2 Device Growth and Fabrication

The ZnO/ZnTe hetero-junction with the structure in Figure 7.1 was grown and fabricated as the following steps.

1. A nitrogen doped ZnTe layer as a buffer layer were grown by molecular beam epitaxy (MBE) on conducting p-type GaAs (001) substrates at a substrate temperature of 250^{o}C, with thickness of 0.6μm and approximate hole concentration of 1×10^{19}cm^{-3}.
2. A 0.4 μm thick layer of ZnTe was grown without intentional doping. Independent calibration runs of ZnTe on insulating substrates resulted in background carrier concentrations of less than 10^{15} cm^{-3}.
3. A subsequent layer of ZnO was grown by pulsed laser deposition (PLD) in a separate chamber, with a thickness of 350nm. The substrate temperature for ZnO deposition was kept intentionally low at 200 ^{o}C to avoid possible degradation of the ZnTe material. The electron concentration of ZnO grown under these conditions has been determined to be approximately 2×10^{18} cm^{-3}.
4. Ti/Au 30nm/70nm for contacts to n-type ZnO deposited by e-beam evaporation at the room temperature was patterned by the lithography and the lift-off processes.
5. Mesa etching was executed by the mixture solution consist of deionized water and hydrofluoric acid with volume ratio of 9:1. The etching rate for ZnO film is about 0.2μm/min.
6. Ni/Au 50nm/100nm for bottom contacts to p-type GaAs were also deposited by e-beam evaporation at the room temperature.
7. The devices usually were annealed under nitrogen ambient at 150^{o}C for 10 minutes in order to reduce the metal/semiconductor contact resistance.

   The fabricated device is illustrated in Figure 7.3.

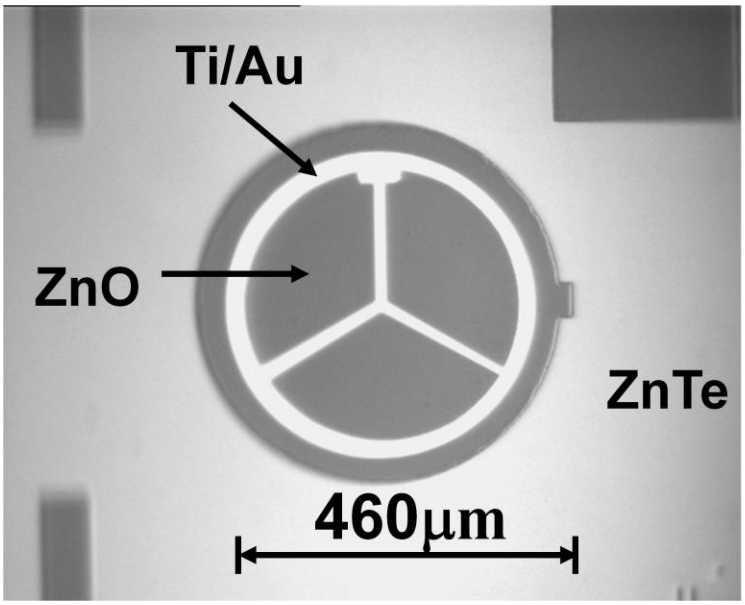

Figure 7.3 Top view of ZnO/ZnTe hetero-junction on GaAs substrate.

7.2 Characterization and Analysis

The ZnO/ZnTe diode properties were explored by electrical, optical and structural measurements.

7.2.1 Structural Mismatch

X ray diffraction (XRD) with ω-2θ wide angle scanning, shown in Figure 7.4, was used to exam the crystalline structure of the ZnO/ZnTe hetero-junction. The ZnTe (002) and (004) reflections clearly indicate the predicted zinc blend ZnTe (001) orientation on the GaAs (001) substrate. A strong ZnO (0002) reflection is observed, indicating the wurtzite c-plane ZnO (0001) orientation. Despite the apparent epitaxial relationship between ZnO, ZnTe, and GaAs, a significant defect density is likely in these hetero-junctions due to the differing symmetry of the hexagonal ZnO crystal structure in comparison to zinc-blend ZnTe. Furthermore, a large defect density is also predicted for the large lattice mismatch in this orientation, where the crystalline relation (0001) ZnO//(001) ZnTe and $\left[10\bar{1}0\right]$ZnO//[110]ZnTe results in a lattice mismatch of 25%.

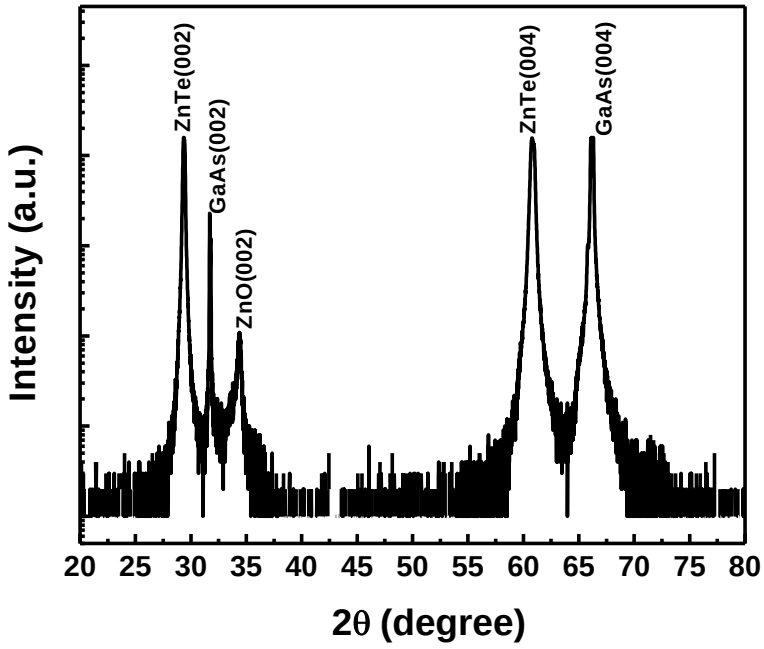

Figure 7.4 X-ray diffraction θ-2θ scan of the ZnO/ZnTe hetero-junction on GaAs.

7.2.2 Current-Voltage Characteristics

Room temperature Current-Voltage (J-V) characteristics of the n-ZnO/p-ZnTe hetero-junction are presented in Figure 7.5 on both a logarithmic and linear scale. The leakage current for the diodes is less than 0.1mA/cm^2 at reverse bias of 1 volt, with a breakdown voltage of approximately 10 volts. In forward bias, the turn-on voltage is approximately 1 volt, resulting in a current on/off ratio of J_{on}/J_{off} of approximately 1×10^5. The J-V characteristics in forward bias fit closely to the diode equation, $J=J_s\ exp(qV-qJR_s/nkT)$, where J_s is saturation current density, q is the charge of an electron, kT is the thermal energy, and n is the ideality factor, R_s is series resistance . The ideality factor of the diode is determined to be 1.3 for the voltage range from 0 to 0.5 volt, indicating primarily diffusion current rather than generation-recombination current in the depletion region. Series resistance was determined to be R_s=0.063Ω.cm^2. The low series resistance in n^+-ZnO/ZnTe/p^+-ZnTe comparing to p^+-ZnTe/ZnTe/n^+-GaAs may be contributed low dislocation density in ZnTe region because of a thick p^+-ZnTe buffer.

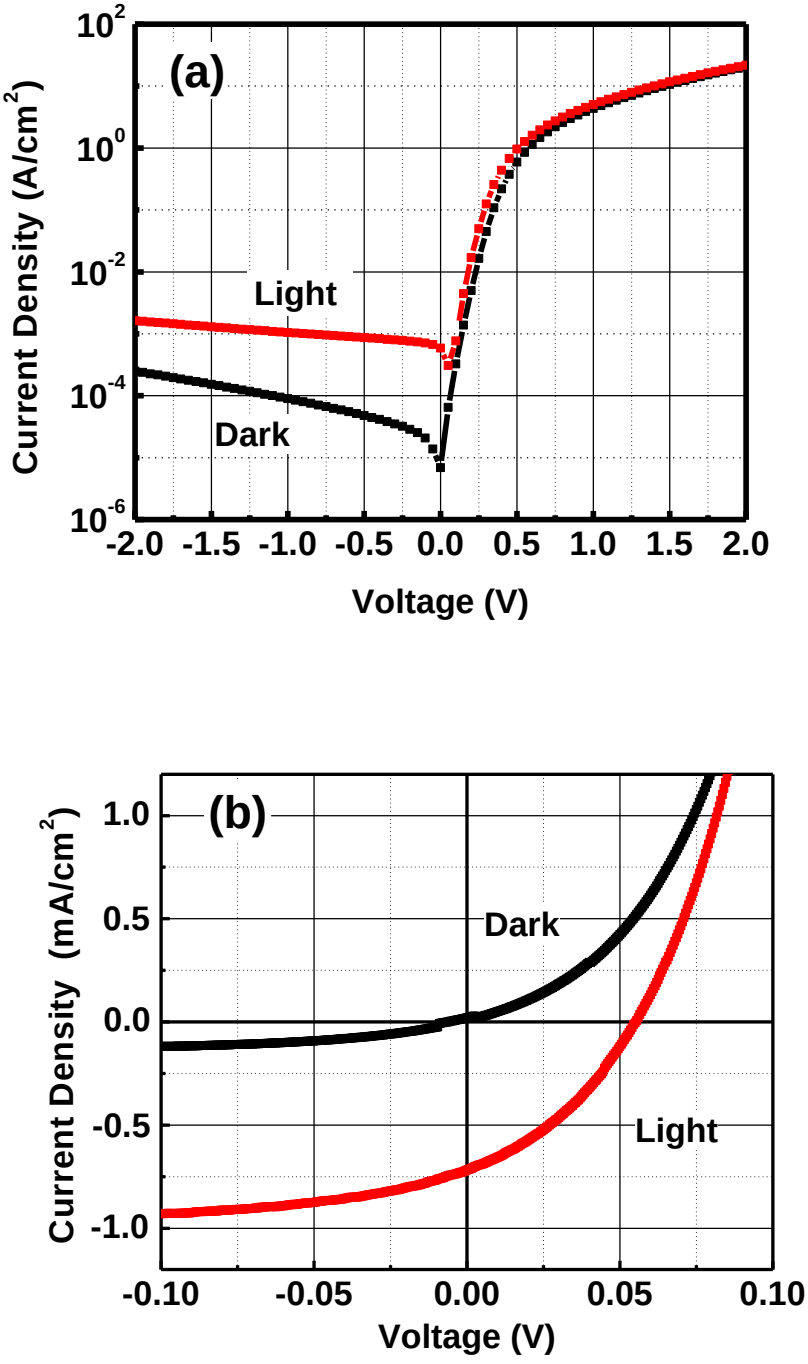

Figure 7.5 Current-voltage characteristics for the ZnO/ZnTe heterojunction diode with and without illumination shown on (a) logarithmic (b) linear scale.

A strong photo-response is observed under illumination through a tungsten lamp with estimated power density about 70mW.cm^{-2} through a microscope objective, as

shown in Figure 7.5 (b). A photovoltaic effect is observed under zero and forward bias, where a short circuit current of J_{sc}~0.8mA/cm^2 and open circuit voltage of V_{oc}~60mV are observed. According to the relation $V_{oc}=nkTln(J_{sc}/J_s)/q$[88], the small V_{oc} is related to a large reverse saturation current density. The reverse saturation current in these diodes may be related to defects arising from the mismatch between the ZnO and ZnTe crystalline structures or defects in the ZnO related to the low temperature deposition process. We have also evaluated ZnO/ZnTe diodes with a similar structure, but without the heavily doped ZnTe buffer layer. The absence of the ZnTe buffer layer would be expected to result in a high density of dislocations within or near the diode depletion region, corresponding to the mismatched ZnTe/GaAs interface. These devices exhibited an increased ideality factor of n=1.9 and lack of photovoltaic effect, consistent with these expectations. Several differing approaches may be used to reduce the reverse saturation current and increase the photovoltaic response. To improve the ZnTe/ZnO match, the (111) ZnTe orientation may be used for an improved match to the hexagonal symmetry of ZnO. Higher quality ZnO material may be utilized by inverting the device structure, i.e. by growing ZnTe (requiring low temperature growth) on high quality ZnO, where (111) ZnTe growth would be expected.

7.2.3 Photo-Response

The spectral response of the diodes is shown in Figure 7.6, where response between 2.3eV and 3.6eV is observed. There is clearly no significant response for energies below 2.3eV, corresponding to the ZnTe bandgap energy. This observation indicates that the GaAs substrate does not play a role in determining the observed diode behavior. For incident photons with energy between the ZnTe and ZnO bandgap energy, absorption and carrier generation occurs primarily in the unintentionally doped ZnTe layer. This ZnTe layer will lie in the depletion region of the diode where photogenerated electron-hole pairs will be separated and collected across the junction by the built-in electric field. The spectral response cutoff at short wavelength (~3.6eV) roughly corresponds to the ZnO bandgap energy, and is discussed in the following. When the energy of incident photons exceeds the bandedge of ZnO (3.37eV), there will be strong optical absorption in the ZnO layer. Shorter wavelengths will lead to increased absorption near the ZnO surface due to

the increasing optical absorption coefficient at higher energies. In order for these photogenerated carriers to contribute to detector photocurrent, the minority carrier holes in the ZnO must diffuse to the junction in order to be swept to the p-side of the junction. However, the diffusion length of holes in ZnO is predicted to be only ~50nm due to the short minority carrier (hole) lifetime in n-ZnO, ~1ns[89], and low minority carrier mobility, ~1cm^2/v.s[90]. This hole diffusion length is significantly smaller than the thickness of the ZnO layer (350nm) in the device structure. The short wavelength cutoff of the detector response just above the ZnO band edge may be attributed to the long diode structure relative to the hole diffusion length.

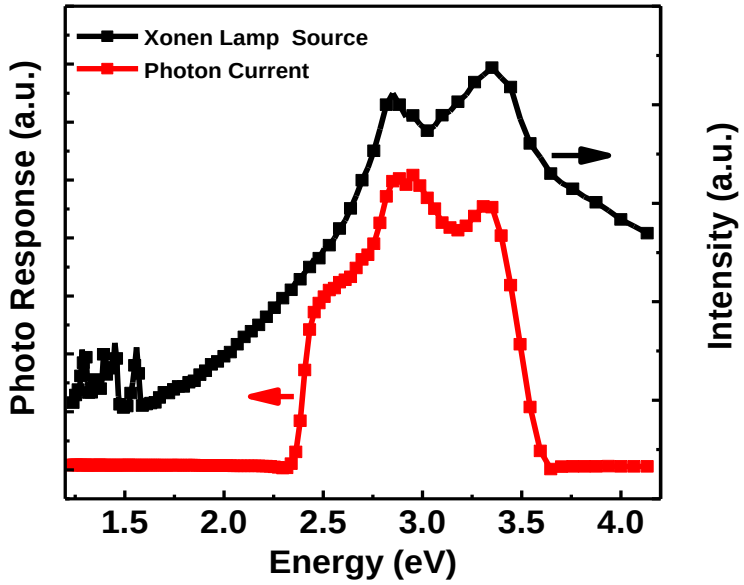

Figure 7.6 Spectral response of the ZnO/ZnTe heterojunction diode and incident xenon lamp.

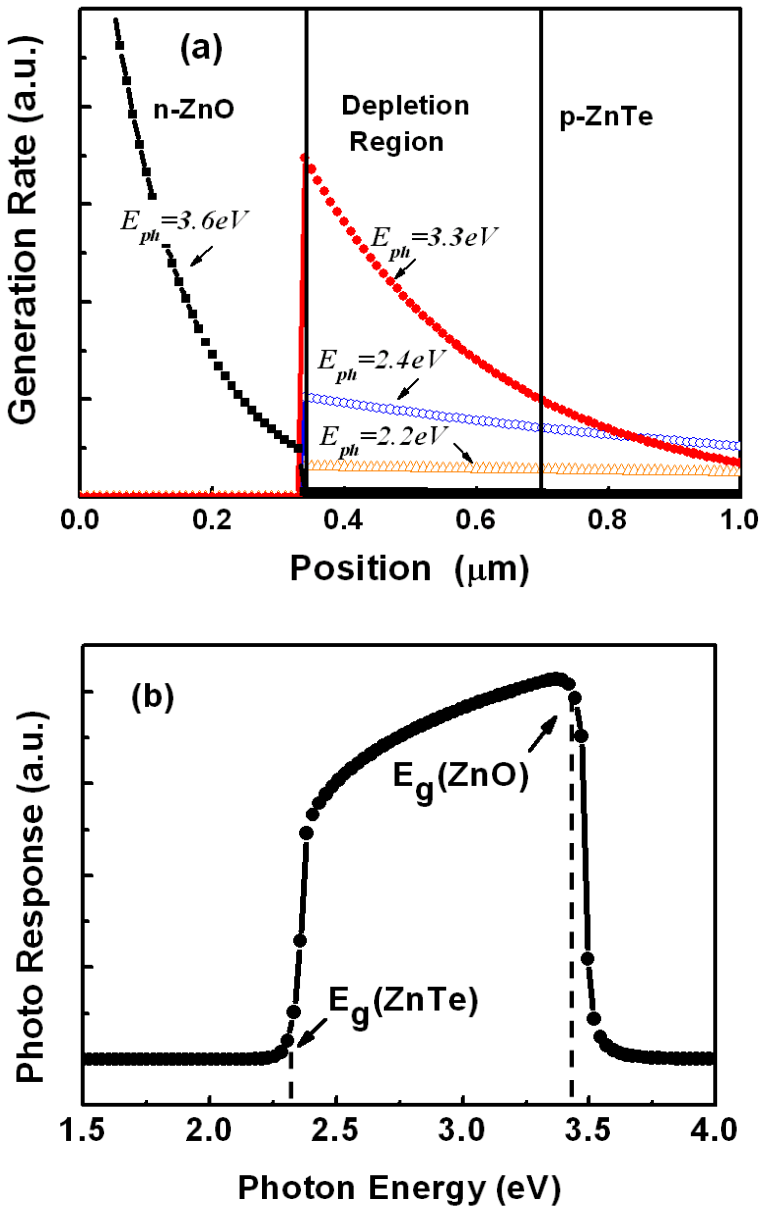

Figure 7.7 Simulation results for the ZnTe/ZnO heterojunction diode showing (a) position dependent carrier generation rate at varying incident photon energy and (b) spectral response.

A device model used to validate our explanation for the photo response behavior. The photon generation rate as a function of position is calculated by $G(x)= \Phi_{opt}\, \alpha\, exp(-\alpha x)$,where x is the position departing from surface, Φ_{opt} is incident photon flux, α is absorption coefficient. The absorption coefficient is given by the following expressions near band edge[91], where E_g is the band gap of semiconductor, E_{ph} is the incident photon

energy, and α_0 and α_1 are fitting parameters for the optical absorption coefficient. The values for these fitting parameters are assumed to be $\alpha_0 \sim 5\times10^4\ \mathrm{cm}^{-1}$, $\alpha_1 \sim 1\times10^4\ \mathrm{cm}^{-1}$, for ZnO[92], and $\alpha_0 \sim 5000\ \mathrm{cm}^{-1}$, $\alpha_1 \sim 1000\ \mathrm{cm}^{-1}$ for ZnTe[93].

$$\alpha = \alpha_0 \exp\left(\frac{E_{ph} - E_g}{kT}\right), \text{ for } E_{ph} < E_g \tag{7.1}$$

$$\alpha = \alpha_0 + \alpha_1 \sqrt{\frac{E_{ph} - E_g}{kT}}, \text{ for } E_{ph} \geq E_g \tag{7.2}$$

The carrier generations at four energies in the range of 2.2eV to 3.6eV is presented in Figure 7.7(a). From this plot, a strong transition from photo-generation in the ZnTe to predominant photo-generation near the incident ZnO surface is observed with increasing photon energy. The photon current density is mainly proportional to the integral of *G(x)* in hole diffusion length in n region, depletion region, and electron diffusion length in p region. The resulting current density for the diode is then calculated according to drift-diffusion equations described in the reference[94]. The calculated spectral response due to the white light illumination with uniform intensity is then shown in Figure 7.7 (b). The simulated spectral response is qualitatively in good agreement with the measured spectral response shown in Figure 7.6. Deviations between calculated and measured spectral response may be primarily attributed to the nonuniform spectral response of the xenon lamp and optical interference effects not accounted for in the simulation.

7.3 ZnSe Buffer

Low series resistances and small ideal factors have been achieved in n-ZnO/p-ZnTe hetero-structure. However, the high saturation current may limit its performance as a solar diode, which results from the high defect density at the ZnO/ZnTe interface because of crystal structure and lattice constant mismatches and atmosphere exposure between ZnTe and ZnO growth. Nevertheless, ZnSe probably is a good candidate to mitigate the interface defects due to the follow reasons.

1) ZnSe is a zinc-blend crystal similar to ZnTe. Its lattice constant is 0.567nm with 6.7% mistmatch with ZnTe, much less than the mismatch between ZnO(111) and ZnTe(100).

2) ZnSe also shows intrinsic n–type behavior andcan be heavily n-type doped with group VII elements[95], such as Cl, Br and I, or group III elements[96], such as Al.

3) Solar absorption in the ZnSe buffer layer is negligible for thin layers (~50nm) and and the wide bandgap (2.70eV at room temperature) measured from the optical reflection as shown in Figure 7.8 .

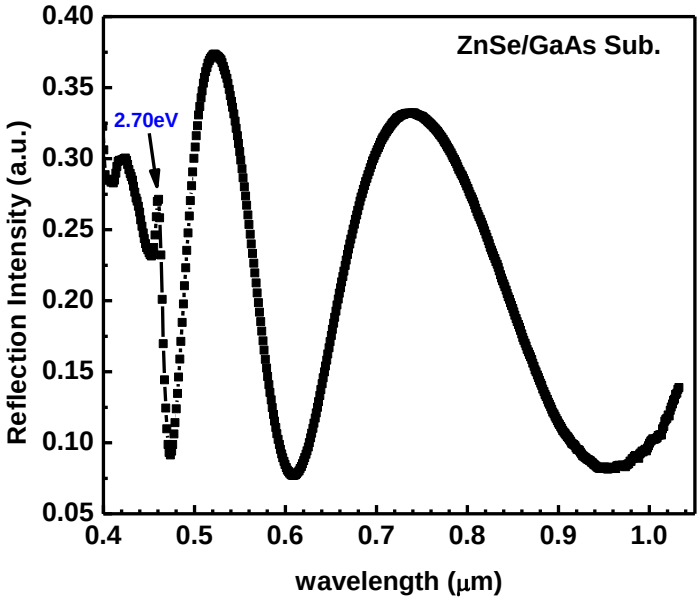

Figure 7.8 The optical reflection of ZnSe thin film GaAs substrate grown by MBE

7.3.1 Device Structure and Fabrication

The schematic diagram of the ZnO/ZnTe junction with a ZnSe buffer structure is shown in Figure 7.10. The growth and fabrication processes are the same as those without a ZnSe buffer layer except for the deposition of ZnSe and ZnO. The ZnSe layers in these devices are deposited either by room temperature e-beam evaporation (SJ26) or by molecular beam epitaxy after ZnTe growth at 250^{o}C. The single crystal ZnTe epitaxy film grown by MBE is indicated by Figure 7.9 in contrast to amorphous ZnSe films deposited by room temperature evaporation. The difference of these two deposition methods will be addressed in the follow section.

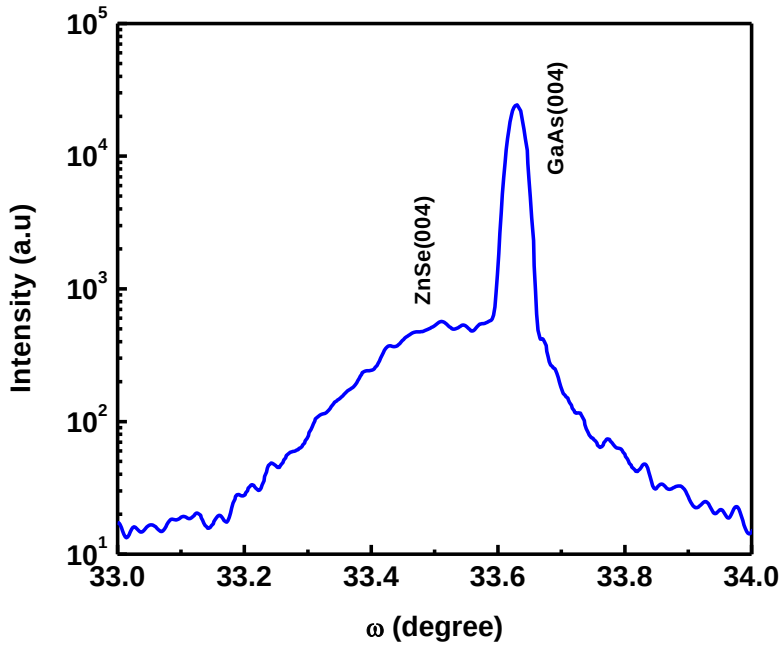

Figure 7.9 X-ray diffraction (ω rocking curve) of ZnSe epitaxy on GaAs (100) substrate.

A 200nm thick ZnO layer with the electron concentration of $5\times10^{18}cm^{-3}$, mobility of $3cm^2/V.s$ was grown by Atomic-Layer-Deposition (ALD) with thickness of 200nm at 150^oC growth temperature. The low mobility of the ZnO film results from the amorphous type crystal obtained at low growth temperature.

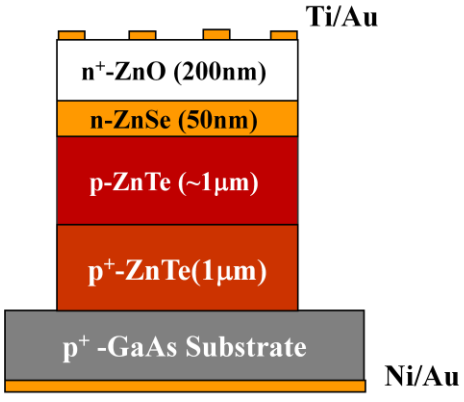

Figure 7.10 Device schematics of n-ZnO/p-ZnTe with a thin ZnSe buffer layer.

Materials	Doping Con.	Electron Affinity	Band Gap	Effective Mass
n-ZnSe	10^{16} cm^{-3}	4.1eV	2.76eV	$m_e=0.21m_0$

Table 7-2 Electrical parameters for band diagram calculation.

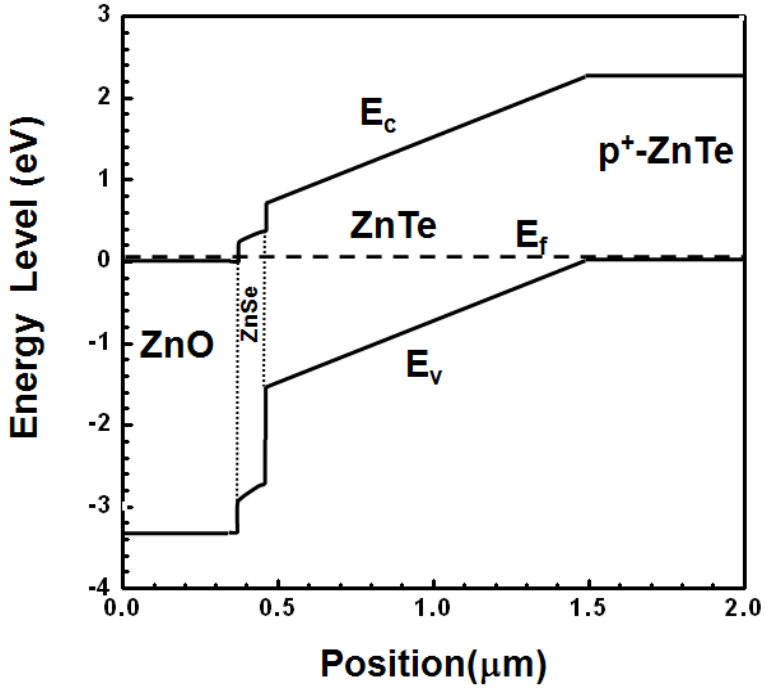

Figure 7.11 Calculated band diagram for n-ZnO/p-ZnTewith a ZnSe buffer layer.

The electrical parameters of ZnTe and ZnO for band diagram calculation are listed in Table 7-1, while the parameters of ZnSe are listed in Table 7-2. The electron concentration in undoped ZnSe grown by MBE is sensitive to growth conditions, and is below10^{16} cm^{-3} in most cases[97]. The calculated band diagram is illustrated in Figure 7.11, where the band alignment between ZnSe and ZnTe is still type II with band barriers for both major carrier injections.

7.3.2 Effect of ZnSe Buffer

Dark I-V curves of ZnO/ZnTe junctions with and without ZnSe buffer are shown in Figure 7.12 on a logarithmic scale. The series resistance for the junction with ZnSe is 241Ω.cm^2 and ideality factor of 3.5. The junction without ZnSe results in a series resistance of 0.46 Ω.cm^2, and an ideality factor of 3.9, both of which are higher than those in previous ZnO/ZnTe diodes with the ZnO films deposited by PLD. The poor diode characteristics may result from the amorphous crystal of ZnO in ALD deposition.

The reverse saturationcurrent in the junction with ZnSe is 10^4 times smaller than that in the junction without ZnSe, and may be due to reduced interface defects in the junction. The forward current is also10^4 time smaller in the junction with ZnSe, probably due to the high resistivity of the ZnSe layer. Therefore, a highly conductive n-type ZnSe with single or poly crystalline structure is preferred to improve the diode characteristics.

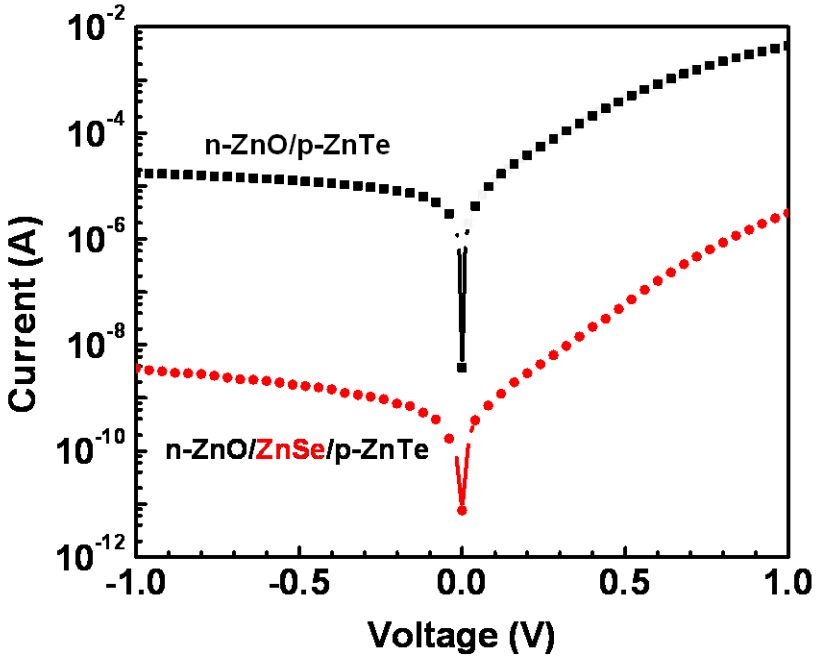

Figure 7.12 Dark I-V curves of n-ZnO/p-ZnTe with and without a ZnSe buffer

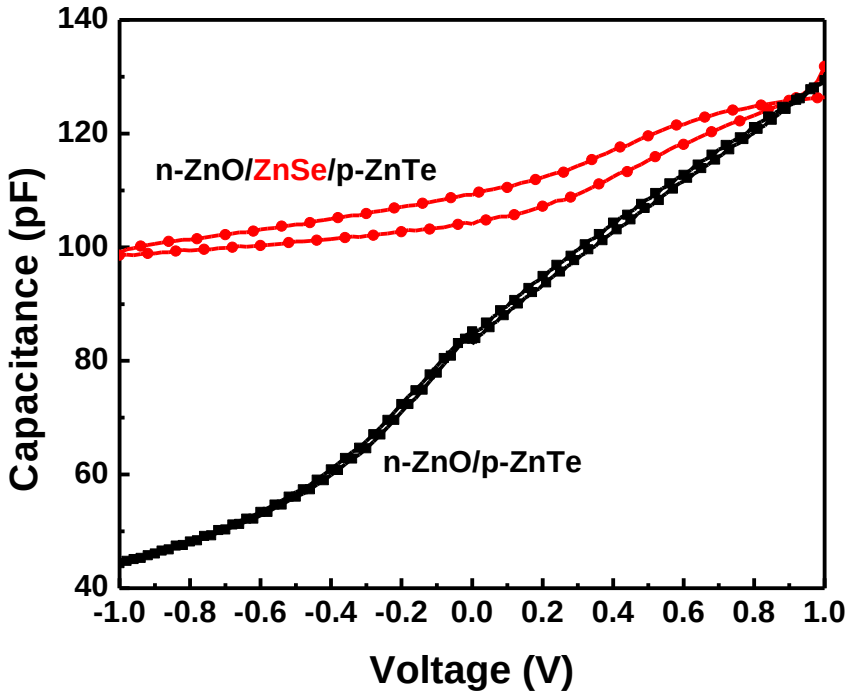

Figure 7.13 C-V curves of n-ZnO/p-ZnTe with and without thin a ZnSe buffer

Significant hysteresis is observed in the capacitance-voltage characteristics of the junction with ZnSe, indicating that there is a high density of charged defects, which are not observed without ZnSe. This difference suggests that amorphous ZnSe is the major cause for high density mobility charges, which are estimated to be on the order of 10^{11} cm^{-2}.

Furthermore, a ZnSe buffer layer prepared by room temperature evaporation provides weaker photovoltaic effect than that without a ZnSe buffer as shown in Figure 7.13. On the contrary, a ZnSe buffer grown by molecular beam epitaxy dramatically improves the diode's photovoltaic effect with V_{oc}=0.7V and J_{sc}=34μA/cm^2, confirming that the crystal quality of ZnSe is critical to achieve the benefit of a ZnSe buffer. The poor fill factor indicates that the high series resistance caused by the ZnSe buffer again becomes the major issue, which may be resolved by intentionally adding a highly conductive n-type ZnSe layer.

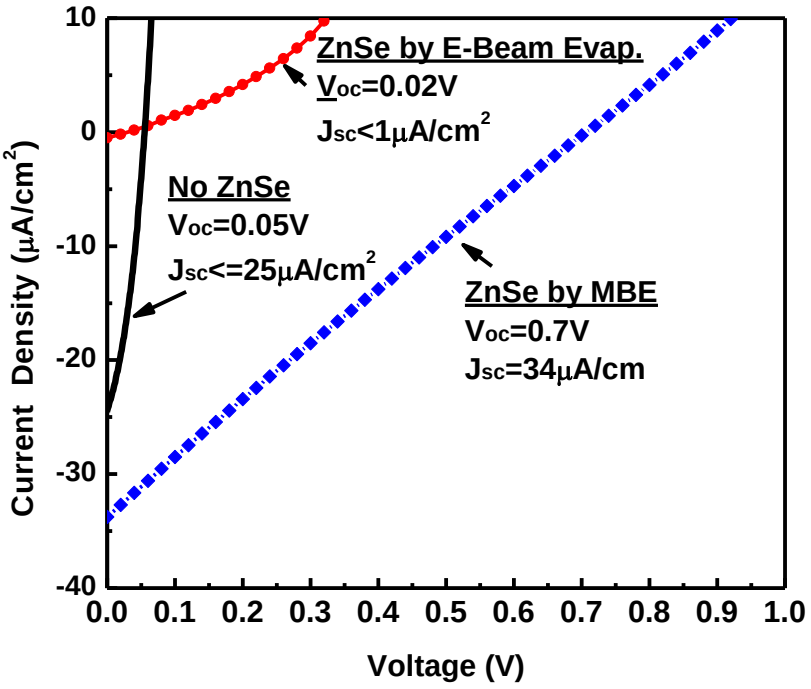

Figure 7.14 I-V curves of ZnO/ZnTe diodes with and without a ZnSe buffer layer under illumination of a microscope tungsten lamp.

7.4 Summary

In conclusion, strong rectifying diode behavior is achieved for n-ZnO/p-ZnTe heterojunction diodes with I_{on}/I_{off} ~ 1×10^5, ideality factor n=1.3, and series resistance Rs=0.063Ω.cm^2. Strong photoresponse is observed in the range of 2.3eV to 3.6eV, where cutoff energies are determined by the absorption edge for ZnTe and minority hole collection in ZnO, respectively. The diode behavior and photovoltaic response indicates that these structures are promising for future electronic and optoelectronic devices based on ZnTe heterojunctions, despite the mismatch between ZnTe and ZnO. A ZnSe buffer grown by molecular beam epitaxy with poly or single crystal structure between the ZnO/ZnTe interface demonstrated a significant improvement of photovoltaic effect probably resulting from interface defects constrain by the ZnSe buffer. However, a highly conductive ZnSe layer with good crystalline quality may be required to reduce the series resistance and saturation current density, and improve a diode ideality so that these n-ZnO/p-ZnTe diodes can become excellent structures for realizing ZnTeO based intermediate band solar cells with high conversion efficiency.

Chapter 8

Conclusions and Future Works

8.1 Summary of Thesis Work

This thesis has investigated the operation of an intermediate band solar cell based on the ZnTeO material system both experimentally and theoretically including material synthesis and characterization; analysis of photo-carrier generation, recombination and transport; and device simulation, fabrication and optimization.

First, ZnTeO material synthesis and characterization of structural, chemical and electrical properties of were presented. These studies conclude that high oxygen concentration in ZnTe results in complex tellurium oxide (TeO_x), and low oxygen concentration (below 10^{20} cm^{-3}) are preferred to generate substitutional oxygen impurities in ZnTe.

Optical properties of ZnTeO were explored in detail by transmission, reflection, and photoluminescence measurement in order to reveal the carrier generation and recombination processes via the oxygen states. The absorption coefficient of oxygen related states about 0.4-0.7eV below the conduction band demonstrated values as high as $10^4 cm^{-1}$ with proper oxygen doping conditions. Oxygen states and associated complexes also demonstrate highly radiative emission ranging from 1.6 eV to 1.9eV, whose radiative recombination coefficient is estimated to be 1.2×10^{-10} cm^3 sec^{-1}, where electron lifetime is more than 1μs confirmed from time resolved photoluminescence. However, the electron lifetime at the conduction band is extremely short (<100ps) due to fast relaxation to oxygen states.

Rate equation analysis suggests that the electron lifetime at the conduction band possibly can be extended to over 1ns when injection carrier density is on the order of the oxygen state density. Rate equation analysis also suggests that the electron lifetime of oxygen states can be extended to as long as the thermal emission time (1millisecond level) by applying a modest electric field.

After understanding the basic properties of the oxygen related intermediate band or states in ZnTe, the theoretical works based on semiconductor device physics was presented in the 5^{th} chapter in order to guide the design of a solar cell device. In n^+-p ZnTe junction with the oxygen states in the p side, the oxygen states are nearly half filled in the depletion region and almost empty in the diffusion region under steady state. Both the open circuit voltage and fill factor degrade but the short circuit current increases comparison to those in a ZnTe junction without oxygen states. The overall efficiency improvement from the oxygen states depend on the value of the optical cross-section. For cross sections larger than $10^{-14}cm^2$, the conversion efficiency of ZnTeO based IBSC can be more than 20% with the optimal oxygen states density in range of 10^{20}-10^{21} cm^{-3} regardless of capture cross section in the range of 10^{-16}-10^{-13} cm^2. The efficiency of a ZnTeO cell is almost double than that of a ZnTe cell.

Experimentally, ZnTeO cells have been applied to p-ZnTe/n-GaAs diode structures exhibiting enhanced response to the solar spectrum in comparison to ZnTe due to photo-excitation below the bandgap energy. The increase in response for the ZnTeO diodes translates to an approximate doubling of the short circuit current, while suffering an approximate 15% decrease in open circuit voltage. Sub-bandgap excitation experiments under 650nm and 1550 nm excitation demonstrate the two-photon response characteristic desired for intermediate band solar cells and serve as a basis for further efforts to develop ZnTeO and other dilute alloys or impurity materials for enhanced solar cell conversion efficiency.

The diode structure was further optimized by n-ZnO/p-ZnTe heterojunction with achievement of current on/off ratio ~ 1×10^5, ideality factor n=1.3, series resistance $Rs=0.063\Omega.cm^2$, and absorption up-edge at 3.6eV. A ZnSe buffer grown by molecule beam epitaxy with poly or single crystal structure between the ZnO/ZnTe interface demonstrated a significant improvement of photovoltaic effect but an increased series

resistance, which probably will be solved by introducing a highly conductive n-type doping for the ZnSe buffer.

8.2 Suggestions on Future Work

The technology of intermediate band solar cell based on ZnTeO is very promising but still in the early research stage. The following topics are extremely important to make it competitive with other mature solar cell technologies.

8.2.1 In-Situ Junction Growth

In this thesis, the solar cell performance is mainly limited by a poor diode characteristic, such as a high saturation current, high series resistance, and poor ideality factor. The growth of a n^+-ZnO/n^+-ZnSe/ZnTeO/p^+-ZnTe structure in one chamber without exposing the device into the atmosphere between thedeposition of various layers is highly recommended.

8.2.2 Role of Oxygen Doping

Oxygen atoms introduced by the plasma cell can incorporate either as substitutional impurities such as O_{Te} O_{Zn} substitutes, or interstitial states. Only O_{Te} states have been confirmed to provide a radiative recombination center. The roles of other states are unclear. Raman spectrum and infrared spectrum may provide the methods to identify O_{Te} states from others. In-situ or ex-situ annealing processes may need to be developed to maximize the formation of O_{Te} States.

8.2.3 Optical Cross-section

The value of optical cross-section for O_{Te} states is still ambiguous, but is the most important parameter for designing device structure, which may be determined from optical deep level transient spectrum.

8.2.4 Flight Mobility

The electron flight mobility in p-type ZnTeO is assumed to same as electron mobility in p-ZnTe. However, more scatter mechanisms may be introduced in ZnTe by doping with oxygen. The relationship of electron mobility and oxygen doping level needs to be identified in order to optimize the device performance.

8.2.5 Optimization of Bandgap

The band gap of ZnTe and energy level of oxygen states are different from the energy levels for the maximum absorption of solar spectrum by an intermediate band structure. It is possible to tune the band gap of ZnTe and oxygen states to the optimized levels by adding some percentage of cadmium.

Appendix I: Growth Process for Oxygen Doping in ZnTe

1. After thermal clean of GaAs substrate, the ratio of Te flux (Beam Equivalent Pressure) to Zn flux is set to 1.5. The typically Zn flux and Te flux for growth is 5.0×10^{-7}Torr. and 7.5×10^{-7}Torr respectively
2. Te is first exposed on GaAs substrates
3. A thin ZnTe nucleation layer (~30nm) is grow by open both Zn and Te flux.
4. Stop growth by shift the main shutter in the growth chamber
5. The oxygen flow rate is set to be 0.1-1.0 sccm by a mass flow controller
6. Completely open the leakage valve to flow oxygen in the growth chamber for 3-5 minutes
7. Increasing the power of the plasma controller unit slowly until the plasma is turned on
8. Wait a minute for stabilizing the oxygen plasma
9. The oxygen partial pressure in the growth chamber is set to a desired valued by closing the leakage valve

Appendix II: Lithography Recipes

1. Clean samples by acetone at room temperature for 2 minutes, and dry the samples by a nitrogen gun
2. Clean the samples by Isopropyl Alcohol at room temperature for 2 minutes, and dry the samples by a nitrogen gun
3. Bake the samples at 130 ^{0}C for 2 minutes
4. Spin Hexamethyldisilazane (HMDS), a photoresist adhesion, with a speed of 4000 cycle/min for 30sec.
5. Spin a positive photoresist, PRS220, with a speed of 4000 cycle/min for 30sec
6. Bake the samples at 105 ^{0}C for 60sec
7. Expose the samples under UV light with power density 20mW/cm2 for 4.5sec
8. Bake the samples at 115 ^{0}C for 60sec
9. Develop the samples in the base solution, MF-319 for 60sec.
10. Deposit metal for lift-off process, or etch the films depending on the processes requirement
11. Remove the photoresist from the samples by acetone solution
12. Clean the samples by Isopropyl Alcohol

REFERENCES

[1] Energy Information Administration, Official Energy Statistics from the U.S. Government (http://www.eia.doe.gov/fuelrenewable.html)

[2] http://en.wikipedia.org/wiki/World_energy_resources_and_consumption

[3] W.Shockley, and H.J.Queisser, J. Appl. Phys. 32, 510 (1961)

[4] http://rredc.nrel.gov/solar/spectra/ (Nov. 2009)

[5] D. M. Chapin, C. S. Fuller, and G. L. Pearson.. J. Appl. Phys. 25, 676 (1954)

[6] L.L. Kzamerski, J. Electron Spectro. Phenom. 150, 105 (2006)

[7] M.A. Green, K. Emery, Y. Hishikawa and W. Warta, Prog. Photovolt: Res. Appl. 17, 320 (2009)

[8] M.A.Green Prog. Photovolt: Res. Appl. 9, 123 (2001)

[9] M.A. Contreras, B. Egaas, K. Ramanatham, J. Hiltner, A. Swartzlander, F. Hasoon, R. Noufi. Prog. Photovolt: Res. Appl. 7, 311 (1999)

[10] X. Wu, J.C. Keane, R.G. Dhere, C. Dehart, A. Duda, T.A. Gessert, S. Asher, P. Sheldon, Conf. Proc., 17th European Photovlot. Solar Energy Conf, Munich, 22-26, 995, (Oct, 2001)

[11] J. Meier. J. Sitznagel, U. Kroll, C. Bucher, S. Fay, T. Moriarty, and A. Shah. Thin Sold Films 451, 518 (2004)

[12] A.S. Brown, M.A. Green, Prog. Photovolt: Res. Appl. 10, 299 (2002)

[13] R.R. King, D.C. Law, K. M. Edmondson, C. M. Fetzer, G. S. Kinsey, H. Yoon. R. A. Sherif and N. H. Karam, Appl. Phys. Lett. 90, 183516 (2007)

[14] A.J. Nozik, Physica E 14, 115 (2002)

[15] G. J. Conibeer, C.-W. Jiang, D. Konig, S. Shrestha, T. Walsh. and M.A. Green, Thin Solid Film, 516, 6968 (2008)

[16] M. Wolf, Proc. IRE, 48, 1246 (1960)

[17] G. Guttler, H. Queisser, Energy Convers. 10, 51 (1970)

[18] P. Wurfel, Sol. Energy Mater. Sol. Cells , 29, 403 (1993)

[19] M.M. Keevers, and M. A. Green, J. Appl. Phys. 75, 4022 (1994)

[20] H.Kasai, T. Sato, and H. Mastsumura, 26th IEEE Photovoltaic Specialists Conferences, Anaheim, CA, Sept. 29- Oct. 3, 215 (1997)

[21] M. J. Keevers, and M. A. Green, Sol. Energy. Mater. Sol. Cell. 41, 195 (1996)

[22] A. S. Brown, M. A. Green, J. Appl. Phys. 92, 1329 (2002)

[23] A. Luque, A. Marti, Phys. Rev. Lett. 78, 5014 (1997)

[24] A. Marti, L. Cuadra, and A. Luque, IEEE Trans. Electron Devices 48, 2394 (2001)

[25] V. Popescu, G. Bester, M. C. Hanna, A. G. Norman, and A. Zunger, Phys. Rev. B 78, 205321 (2008)

[26] A. M. Kechiantz, L. M. Kocharyan, and H. M. Kechiyants, Nanotechnology, 18, 40, 405401,(2007)

[27] A. Luque, A. Marti, C. Stanley, N. Lopez, L. Cuadra, D. Zhou. And A. Mckee, J. App. Phys. 96, 903 (2004)

[28] A. Franceschetti, S. Lany, and G. Bester, Phys. E, 41, 15 (2008)

[29] R. Oshima, A. Takata, and Y. Okada, Appl. Phys. Lett. 93, 08311 (2008)

[30] K. Barnham, B. Braun, J.Nelson, M. Paxman, C. Button and J. S. Roberts and C. T. Foxon, Appl. Phys. Lett. 59, 135 (1991)

[31] K. M. Yu, W. Walukiewicz, J. W. Ager, D. Bour, R. Farshchi, O. D. Dubon, S. X. Li, I. D. Sharp, and E. E. Haller, Appl. Phys. Lett. 88, 92110 (2006)

[32] E. Canovas, A. Marti, A. Luque, and W. Walukiewicz, Appl. Phys. Lett. 93, 174109 (2008)

[33] G. Becaucarne, A.S. Brown, M. J. Keevers, R. Corkish, and M.A.Green, Prog. Photovolt: Res. Appl. 10, 345 (2002)

[34] T.Tibbits, I,Ballard, K. Barnham, D. Johnson, M. Mazzer, J. Roberts, R. Airey, N. Foan, Conference Record of the 2006 IEEE 4th World Conference on Photovoltaic Energy Conversion p4 (2006)

[35] A. Luque, A. Marti, N. Lopez, E. Antolin, E. Canovas, C. Stanley, C. Parmer, and P.diaz, J. Appl. Phys. 99, 094503 (2006)

[36] P. Olsson, J. -F. Guillemoles, and C. Domain, J. Phys. Conden. Matter, 20, 064226 (2008)

[37] J. Wu, W. Shan, and W. Walukiewicz, Semicond. Sci. Technol. 17, 860 (2002)

[38] K. M. Yu, W.Walukiewicz, J.Wu, W. Shan, J.W. Beeman, M. A. Scarpulla, O. D. Dubon, and P. Becla , Phys. Rev. Lett. 91,246403(2003)

[39] S. O. Ferreira, H. Sitter, W. Faschinger and G. Brunthaler, , J. Cryst. Growth 140, 282 (1994).

[40] C. M. Rouleau, D. H. Lowndes, J. W. McCamy, J. D. Budai, D. B. Poker, D. B. Geohegan, A. A. Puretzky and S. Zhu, , Appl. Phys. Lett. 67, 2545 (1995).

[41] J. Han, T. S. Stavrinides, M. Kobayashi, R. L. Gunshor, M. M. Hagerott and A. V. Nurmikko, Appl. Phys. Lett. 62, 840 (1993).

[42] I. W. Tao, M. Jurkovic and W. I. Wang, Appl. Phys. Lett. 64, 1848 (1994).

[43] R.F Brebrick, Phys. Chem. Solids 4, 190 (1958)

[44] G. Mandel, Phys. Rev. 134, A1073 (1964)

[45] J. D. Dow, R.-D. Hong, S. Klemm, S. Y. Ren, M.-H. Tsai, O. F. Sankey and R. V. Kasowski, Phys. Rev. B (Condensed Matter) 43, 5396 (1991)

[46] K. Akimoto, H.Okuyam, M. Ikeda and Y. Mori, J. Cryst. Growth, 117, 420-423 (1992)

[47] J.J.Hopfield, D.G. Thomas and R.T.Lynch, Phsy, Rev. Lett. 17, 312(1966)

[48] R. E. Deitz, D.G. Thomas, and J. J. Hopfield. Phys. Rev. lett. 8, 391 (1962)

[49] J.D. Cuthbert, J.J. Hopfield, and D.G. Thomas, USA Patent 3413506 (1966)

[50] Z. T. Kang, H. Menkara, B. K. Wagner, C. J. Summers, R. Durst, Y. Diawara, G. Mednikova and T. Thorson, J. of Electron. Mater. 35, 1262 (2006).

[51] K. M. Yu, W. Walukiewicz, J. Wu, W. Shan, J. W. Beeman, M. A. Scarpulla, O. D. Dubon and P. Becla, Phys. Rev. Lett. 91, 246403 (2003)

[52] S. Merita, T. Kramer, B. Mogwitz, B. Franz, A. Polity and B. K. Meyer, Phys. Status Solidi C 4 960 (2006).

[53] Y. Nabetani, T. Okuno, K. Aoki, T. Kato, T. Matsumoto and T. Hirai, Phys. Status Solidi A 203, 2653 (2006).

[54] J. H. Chang, T. Takai, B. H. Koo, J. S. Song, T. Handa, and T. Yao, Appl. Phys. Lett. 79, 785 (2001)

[55] D. T. F. Marple, J. Appl. Phys. 35, 539 (1964)

[56] K. Moazzami , Ph.D. dissertation, 'Characterization of Optoelectronic Properties of HgCdTe & ZnO II-VI Semiconductors for Infrared & Ultroviolet Detector Application', p 33, (2006)

[57] J. L. Merz, J. Appl. Phys. 42,2463 (1971)

[58] J. L. Merz, Phys. Rev. 176, 960 (1968)

[59] M. Felici, A. Polimeni, M. Capizzi, Y. Nabetani, T. Okuno, K.Aoki, T.Kato, T.Matsumoto, and T.Hirai, Appl, Phys. Lett., 88, 101910 (2006)

[60] M. J. Seong, I. Miotkowski and A. K. Ramdas, Phys. Rev. B (Condensed Matter) 58, 7734 (1998)

[61] H. L. Porter, C. Jin, J. Narayan, A. L. Cai, J.F.Muth, O. W.Holland, Mat. Res. Soc. Sypm. Proc. 744, M5.5.1 (2003)

[62] S. Iida, J. Phys.Soc. Jpn. 32, 142 (1972)

[63] M. Schneider, H. Tews, and R. Legros, J. Cryst. Growth, 59, 293 (982)

[64] A. Testa, W. Czaja, A. Quattropani, and P. Schwendimann, J. Phys. C: Solid State Phys. 1253 (1987)

[65] Y. Burki, W. Czaja, V. Cappozzi, and Schewndimann, J. Phys. : Condens. Matter 5 9235 (1993)

[66] R.Pasler, Phys. Rev. B. 36, 1168 (1987)

[67] G. Bacher, et al, Rhys. Rev. B. 47, 9545 (1993)

[68] A. S. Brown and M. A. Green, J. Appl. Phys. 94, 6150 (2003).

[69] L. Cuadra, A. Marti and A. Luque, Thin Solid Films 451-452, 593 (2004).

[70] R.S.Titile, G. Mandel, and F. F. Morehead, Phys. Rev. 136, 300 (1964)

[71] J. L. Merz, J. Appl. Phys. 42,2463 (1971)

[72] Y. Nabetani, T. Okuno, K. Aoki, T.Kato, T. Matsumoto, and T. Hirari, Phys. Stat. Sol. (a), 11, 2653 (2006)

[73] D. Z. Garbuzov, J. Luminescence 27, 109 (1982)

[74] U. Strauss and W.W. Ruhle, Appl. Phys. Lett. 62, 55 (1993)

[75] A. F. Tasch, Jr. and C.T. Sah, Phys. Rev. B1, 800 (1970)

[76] D. Z. Garbuzov, J. Luminescence 27, 109 (1982)

[77] W.Wang, A. Lin, J.D. Phillips, J. Electrical Mater, 37, 1044 (2008)

[78] A. Luque, A. Marti, Phys. Rev. Lett. 78, 5014 (1997)

[79] A. Lin, W. Wang, J. Phillips, J. Appl. Phys. 105, 064512 (2009)

[80] A. Luque, A. Marti, N. Lopez, E. Antolin, and E. Canovas, C. Stanley, C.Farmer, and P.Diaz, J. Appl. Phys. 99, 094503 (2006)

[81] J. H. Chang, T. Takai, B. H. Koo, J. S. Song, T. Handa and T. Yao: Appl. Phys. Lett. 79 785 (2001)

[82] J. J. Hopfield, D.G. Thomas and R. T. Lynch, Phys, Rev. Lett. 17, 312(1966)

[83] R. E. Deitz, D.G. Thomas, and J. J. Hopfield. Phys. Rev. lett. 8, 391 (1962)

[84] J. D. Cuthbert, J. J. Hopfield, and D. G. Thomas, USA Patent 3413506 (1966)

[85] W. Wang, W. Bowen, S. Spanninga, S. Lin and J. Phillips, J. Electrical Mater. 38, 119 (2009)

[86] D. C. Look, Mater. Sci. Eng., B 80, 383 (2001).

[87] B. M. Ataev, A. M. Bagamadova, A. M. Djabrailov, V. V. Mamedov and R. A. Rabadanov Thin Solid Film,260, 19 (1995)

[88] P. Bhattacharya, Semiconductor Optoelectronic Devices, New Jersey, Prentice hall, 417 (1994).

[89] K Moazzami, T E Murphy, J D Phillips, M C-K Cheung and A N Cartwright, Semicond. Sci. Technol. 21, 6, 717 (2006)

[90] D. C. Look, and B. Claflin, Phys. Stat. Sol. (b) 241, 3, 624 (2004)

[91] C.A.Hougen, J.Appl. Phys., 66, 8, 3763 (1989)

[92] V. Srikant and D. R. Clarke, J. Appl. Phys. 81, 9, 6357 (1997)

[93]A. Erlacher, M. Ambrico, G. Perna, L. Schiavulli, T. Ligonzo, H. Jaeger and B. Ullrich, Appl, Surf. Sci 248, 402 (2005)

[94] H.J.Hovel, Semiconductors and Semimetals, Academic Press, vol,11, Solar cells, 17 (1975)

[95] Z.Zhu, H.Mori, and T. Yao, Appl. Phys. Lett. 61, 2811(1992)

[96] T. Takai, J.H. Chang, K.Godo, T. Handa, T.Yao, Phys. Status. Solidi B229, 381(2002)

[97] T. Yao, M. Ogura, S. Matsuoka, and T. Morishita, J. J. App. Phys. 22, 144 (1983)